INFRARED-BRIGHT GALAXIES IN THE MILLENNIUM SIMULATION AND SUNYAEV ZELDOVICH EFFECT CONTAMINATION

Daniel Christopher Opolot

A thesis submitted in partial fulfilment of the requirements
for the degree of Master of Science in the Department of Physics,
University of the Western Cape

Prof. Catherine Cress

March 9, 2010

Keywords

Cosmic microwave background, Sunyaev Zel'dovich effect (SZE), Galaxy clusters, Dark energy, Structure evolution, Millennium N-body simulation, Star formation, Infrared galaxies, Cluster galaxy number density, SZE contamination.

Abstract

Infrared-bright galaxies in the millennium simulation and Sunyaev Zeldovich effect contamination.

O D C Opolot.

MSc Thesis, Department of Physics, University of the Western Cape.

8.10.2009

Measuring the evolution of the abundance of galaxy clusters puts constraints on cosmological parameters like the cosmological density parameter Ω_m, σ_8 and the dark energy equation of state parameter, w. Current observations that promise to give large cluster counts and their properties are those that rely on the Sunyaev-Zeldovich effect (SZE) from clusters. We study the contamination of the SZ signals from galaxy clusters by cluster infrared (IR) galaxies and particularly faint IR galaxies. We use the Millennium simulation database to extract galaxy clusters and deduce contaminant IR fluxes using the star formation rate - IR luminosity relations. We use the IR spectral energy distribution (SED) to obtain the monochromatic fluxes at 145 GHz, 217 GHz and 265 GHz, which are the observation frequencies of the Atacama Cosmology Telescope (ACT). Taking ACT as a case study, we selected all clusters with $M_{vir} \geq 2 \times 10^{14}$ $M_\odot$, and consider all galaxies in a cluster with star formation rate $sfr \geq 0.2$ $M_\odot yr^{-1}$ as IR galaxies. From the fluxes of these selected sources, we compute their contribution to the SZE temperature fluctuations.

We find that the galaxies in clusters have a non-neglible contribution to the SZ signals. In massive and rich clusters the contribution can be as high as 100 μK at $z = 0.36$, which is substantial when compared to the thermal SZE of $\gtrsim 270\mu$K for such clusters. This effect can be reduced significantly if proper modelling of IR sources is done to pick out the point sources within clusters. We also find that irrespective of the mass range, the average contaminant temperature fluctuation ΔT can be modelled as a power-law: $\Delta T = Cz^m$, where z is the redshift, $m = 1.8 \pm 0.07$ and C takes on a range of values (0.008 to 0.9) depending on the cluster mass and the observation frequency respectively. We also study some properties of simulated galaxy clusters like substructures in clusters, 2D projected distributions and number density profiles, which are all discussed in the results.

UNIVERSITY of the
WESTERN CAPE

Declaration

I declare that *Infrared-bright Galaxies in the Millennium Simulation and Sunyaev-Zeldovich Effect Contamination* is my work, that it has not been submitted for any degree or examination in any other university, and that all the sources I have used or quoted have been indicated and acknowledged by complete references.

Full name..... Date.....

Signed.....

Acknowledgement

I would like to extend my sincere gratitude to my Supervisor Dr. Catherine Cress for her guidance and support during the entire course of the project both academically and motivationally. To the University of the Western Cape Physics department for hosting me during the study and for the facilities as well as the logistics provided. Many thanks to the Square Kilometer Array (SKA-South Africa) program at large for the financial support and the recreational activities; Kim de Boer for all the responses. Not forgetting my research group, Claudio Moises Paulo, Ando Ratsimbazafy, Sean Passmoor, Fidy Ramamonjisoa, and Daniel Cunnama for all the ideas and contributions during the discussion groups. The masters coursework classmates, Anne Marie, Sean February, Jean Kubwimana.
Lastly to my family for all the support, Victoria Namutebi for your wise words of encouragement.

Contents

1 Introduction **2**

1.1 Objectives 4

2 Theoretical background **5**

2.1 Introduction 5

2.2 The cosmic microwave background (CMB) 5

2.3 Sunyaev-Zel'dovich effect 7

2.3.1 Inverse Compton scattering (IC) 7

2.3.2 Sunyaev-Zel'dovich Effect in galaxy clusters 9

2.3.3 Kinetic SZE 14

2.3.4 The relation between observed SZE fluxes and the temperature fluctuations 16

2.4 The standard cosmological model 18

2.5 Galaxy clusters 19

2.6 Structure evolution in the Universe and the initial conditions 22

2.7 The millennium simulation 28

2.7.1 Dark matter simulation 28

2.7.2 Semi-Analytic models (SAM) 33

3 Methodology **42**

3.1 Introduction 42

3.2 Data 42

3.3 Fluxes 43

3.4 Temperature fluctuations 47

4 Results and Discussion **48**

4.1 Overview 48

4.2 Simulation output versus observations 48

4.3 The distribution of simulated star forming galaxies in clusters 52

4.3.1 2D projections 52

4.3.2 The radial distribution of galaxies in clusters and substructure . . . 56

4.3.3 The fraction of star forming galaxies in clusters as a function of cluster size and redshift 61

4.4 Implied temperature fluctuations from infrared-bright galaxies in clusters . 65

4.4.1 Magnitude of point-source contributions compared to SZ signatures 75

4.4.2 Removing bright point sources and residual temperature fluctuations 76

5 Conclusion **78**

6 Appendix **81**

6.1 Radiation energy density in Compton scattering 81

6.2 Derivation of thermal SZE for relativistic limit 83

6.3 The kinetic SZE 85

List of Figures

2.1 [Adopted from [6]] Geometrical illustration of inverse Compton scattering in the rest frame of electron before the interaction. The photon is incident at an angle θ relative to the x axis (direction of motion of the electron). It is deflected by angle ϕ_{12} , and emerges after the scattering at angle θ'. In the observers frame, where the electron is moving with velocity βc along the x axis, the photon changes energy by an amount depending on $\beta = v/c$ and the angles θ and θ'. 7

2.2 The background photons are scattered by the intracluster hot electrons causing a shift in energies of photons, which is observed as a collective effect 10

2.3 §[8] Distortion of the Cosmic Microwave Background spectrum by inverse Compton scattering. The dashed line is the spectrum before scattering and the solid line is after distortion. What is shown is exaggerated for illustrative effects (its for a fictional cluster 1000 times more massive than a typical massive galaxy cluster). The intensity decreases in the Rayleigh-Jeans region of the spectrum and increases in the Wien region 12

2.4 § [49] The spectral distribution of ΔI_ν for $y = 0.0005$ for five different conditions, the Kompaneets limit with kT/mc^2 close to zero, and four curves with kT of 5.1, 15.3, 25.5, and 125 Kev, showing the difference in amplitudes for relativistic and nonrelativistic distributions 13

2.5 § [8] The spectral distortion of the CMB spectrum by SZEs. The cluster properties used to calculate the spectra are an electron temperature of 10 keV, a Compton y parameter of 10^{-4} , and a peculiar velocity of 500 km s^{-1}. The dotted line is a 2.7 K thermal spectrum for the CMB intensity scaled by 0.0005. The kSZE, the dashed line is much smaller than the tSZE, the solid line. 15

2.6 Adopted from Bahcall et al (1997). Shows the evolution of abundance of massive coma-like clusters with redshift. Line represent predictions from different models obtained from large-scale cosmological N-body simulations ($400h^1$Mpc box size) for different cosmologies: Standard Cold Dark Matter (SCDM,$\Omega_m = 1$, COBE normalised: §17, $\sigma_8 = 1.05$), SCDM with $\sigma_8 = 0.53$ (normalised to the present-day cluster abundance; Mixed Dark Matter (MDM: hot + cold), Open CDM (OCDM,$\Omega_m = 0.35$, $\sigma_8 = 0.8$), and Lambda CDM (LCDM, $\Omega_m = 0.4$, $\Lambda = 0.6$, $\sigma_8 = 0.8$. The data points are from Canadian Network for Observational Cosmology (CNOC) survey, which was originally designed to differentiate between the Ω=1 and $\Omega \simeq 0.2$ cosmologies.) 21

2.7 § [15] Number density of haloes with $M \geq 10^{14} M_{\odot}$ plotted as a function of redshift z for various Q models (with different equation of state parameters, $w_x(z)$). The other cosmology used is $\Omega_m = 0.3$, $\Omega_\lambda = 0.7$, $H_0 = h\ 100\ kms^{-1}Mpc^{-1}$ with $h = 0.7$, and the rms matter density fluctuation within a sphere of radius 8 h^1 Mpc linearly extrapolated to today, $\sigma_8 = 0.8$. 22

2.8 § [4] The WMAP angular power spectrum: the vertical axis can be taken as the amplitude of temperature fluctuation as observed in the sky and the horizontal axis (multipole moment) is the angular scale on the sky ($\simeq 180/l$ degrees). The acoustic peaks can be clearly seen, the first one at about 1^o . 24

2.9 § [21] [53] The large-scale redshift-space correlation function of the SDSS LRG sample (k is an equivalent of inverse of spatial scale factor or wavelength) for different models of $\Omega_m h^2 = 0.12$ (top, green), 0.13 (red), and 0.14 (bottom with peak, blue). The bump exists at about $100h^{-1}$ Mpc as predicted by the physics before recombination. In Fourier space, this can be seen as wiggles with wavelength scale determined by the sound Horizon. 25

2.10 adopted from Meiksen & White (1997). The matter power spectrum at various redshifts in Fourier space. The power is divided by a real-space zero-baryon power spectrum (matter power spectrum without wiggles). The oscillations are the *Baryon Acoustic Oscillations*. The effect of nonlinear gravitational collapse is demonstrated. It is a function of both redshift and scale factor or wavelength. Taking spherical shells in the sky, at lower redshifts, nonlinearity exists up to larger scales compared to higher redshifts. e.g at $z = 1$, the linear regime exists up to $k < 0.2hMpc^{-1}$ corresponding to 2-3 oscillations and at $z = 3$, its up to $k < 0.5hMpc^{-1}$, about 4 oscillations 26

2.11 § [56] Schematic organisation of the merger tree in the Millennium Run. At each output time, FOF groups are identified which contain one or several (sub)halos. The merger tree connects these halos. The FOF groups play no direct role, except that the largest halo in a given FOF group is the one which may develop a cooling flow according to the physical model for galaxy formation implemented for the trees. To facilitate the latter, a number of pointers for each halo are defined. Each halo knows its descendant, and its most massive progenitor. Possible further progenitors can be retrieved by following the chain of next progenitors. In a similar fashion, all halos in a given FOF group are linked together. 30

2.12 § [56] The dark matter density field on various scales. Each individual image shows the projected dark matter density field in a slab of thickness $15h^1$ Mpc (sliced from the periodic simulation volume at an angle chosen to avoid replicating structures in the lower two images), colour-coded by density and local dark matter velocity dispersion. The zoom sequence displays consecutive enlargements by factors of four, centred on one of the many galaxy cluster halos present in the simulation. 31

2.13 § [56] Differential halo number density as a function of mass and epoch. The function $n(M, z)$ gives the comoving number density of halos less massive than M. It is plotted as the halo multiplicity function $M^2\rho^{-1}dn/dM$, where ρ is the mean density of the universe. The fraction of mass bound to halos of more than 20 particles (vertical dotted line) grows from 6.42×10^4 at $z = 10.07$ to 0.496 at $z = 0$. Solid lines are predictions from an analytic fitting function proposed by Jenkins (2001), while the dashed lines give the Press-Schechter model [48] at $z = 10.07$ and $z = 0$. 32

2.14 §[3] A schematic of the cooling model used in semi-analytical models represents a stage in the cooling process. In the first step (t_1), baryons fall into the gravitational potential well of the dark matter halo. This gas is assumed to be heated by shocks as it falls into the potential well, attaining the virial temperature associated with the halo (t_2). In the third step (t_3), the inner parts of the hot gas halo cool, forming a rotationally supported disc. At a later stage (t_4), the radius within which gas has had time to cool advances outwards towards the virial radius of the halo and the cold gas disc grows in size 35

2.15 § [11]The black hole accretion rate density, $\dot{m}_{BH}$, as a function of redshift for both the 'quasar' and the 'radio' modes discussed above. This figure shows that the growth of black holes is dominated by the 'quasar mode' at high redshift and falls off sharply at $z \lesssim 2$. In contrast, the 'radio mode' becomes important at low redshifts where it suppresses cooling flows, but is not a significant contributor to the overall black hole mass budget 38

3.1 § [9] The asterisks show data from IRAS, ISOCAM and SCUBA surveys. The lines are the best fit of a first order polynomial. The red triangles are the corresponding values from template spectral energy distributions of Chary & Elbaz [9]. 44

3.2 § [50] The spectral energy distribution of infrared bright galaxy. It includes a grey-body (dotted line), a warm power-law (short-dash), PAH emission (long-dash), and unextincted stellar emission (dot-dash) with $e^{-\tau\nu}$ extinction applied. The thick solid line is the total 46

4.1 IR luminosity function (LF) observations adapted from [29], in which crosses mark the local LF from Sanders et al. (2003) and the corresponding solid line is the double power law fit to the local data. The symbols mark the LF calculated in their work at redshift 0.3 (upside down triangles), 0.5 (squares), 0.8 (circles) and 1.0 (triangles). The lines are the local LF evolved to the corresponding redshift with the best fit pure evolution parameters. The arrows indicate bins which are incomplete because of the survey sensitivity. The horizontal error bars indicate the binsize 49

4.2 The IR luminosity function, obtained using our model in the millennium simulation at different redshifts. The three lines (dash, dotted, and dash-dotted) are corresponding fits for the redshifts $z = 0$, 0.28 and 0.76. The break points indicate a seperation between the two classes of infrared galaxies, the Luminous InfraRed Galaxies (LIRGs) and the Ultra-Luminous InfraRed Galaxies (ULIRGs). The low density of ULIRGs can thus be effectively seen as a sharp slope in the luminosity function. What is also recognisable is the difference in the evolution rate of the number density of the two classes, it is relativey high for ULIRGs, an indication of their abundance at higher redshifts. It is also vital to note that this is a log - log plot 50

4.3 Examples of the distribution of galaxies in clusters at redshift, $z = 0.36$. The grey points are galaxies with star formation rate, sfr< 0.2 in $M_{\odot}yr^{-1}$ and the green circles are galaxies with $0.2 <$sfr< 1, and so on as indicated on the figure. The grey points are scaled smaller than the others for visual clarity. The three figures are for a less massive cluster ($2.2 \times 10^{14} M_{\odot}$), an intermediate mass cluster ($7.5 \times 10^{14} M_{\odot}$) and the most massive $2.21 \times 10^{15} M_{\odot}$ cluster projected on the x-y axes. 54

4.4 The upper row is two clusters at intermediate redshift, $z = 0.69$, a $2.2 \times 10^{14} M_{\odot}$ cluster (left) and a $1.16 \times 10^{15} M_{\odot}$ (right). The bottom row is two clusters at $z = 1.08$, a $2.1 \times 10^{14} M_{\odot}$ cluster (left) and $7.1 \times 10^{14} M_{\odot}$ (right). The projected distribution doesn't seem to vary with redshift significantly, but what is obvious is that the number of star forming galaxies tends to increase with redshift, depending on the richness of the cluster. 55

4.5 The radial distribution of starforming galaxies. Number density in 2D annuli (Mpc^{-2}) are compared with 3D shells (Mpc^{-3}) for galaxies with $sfr > 0.2 M_{\odot} yr^{-1}$. The three rows are clusters with mass $2.045 \times 10^{14} M_{\odot}$ ($R_{vir} = 52.65\ Mpc$) and $5.7 \times 10^{14} M_{\odot}$ ($R_{vir} = 147.63\ Mpc$) at $z = 0.36$, and $1.16 \times 10^{15} M_{\odot}$ ($R_{vir} = 300.44\ Mpc$) at $z = 0.69$. In the last row, we show an example of a cluster that has a significant number of starforming galaxies at its centre. 59

4.6 Number density of galaxies in 2D (Mpc^{-2}) as a function of radius: comparison of all galaxies in the cluster with those that have $sfr > 0.2 \mathrm{M}_{\odot} yr^{-1}$. The three rows are clusters $2.045 \times 10^{14} M_{\odot}$ and $5.7 \times 10^{14} M_{\odot}$ at $z = 0.36$, and $1.16 \times 10^{15} M_{\odot}$ at $z = 0.69$. In the first cluster, a higher fraction of star forming galaxies can be seen in an infalling halo at the outskirts of cluster 60

4.7 The left column is the two dimensional radial distribution and the right column is the three dimensional radial distribution of galaxies with sfr$> 0.2 M_{\odot} yr^{-1}$. The units of n_{rel} in 2D are Mpc^{-2} and in 3D are Mpc^{-3}. In each panel, the average distributions for galaxies with different virial radii, R_{vir} are plotted. The three rows are for redshifts $z = 0.38, 0.69, 1.08$ respectively. Note that n_{rel} decreases with increasing R_{vir} 63

4.8 Two dimensional radial distribution of galaxies with sfr$> 0.2 M_{\odot} yr^{-1}$. Different plots are for clusters scaled to virial radii of $R_{vir} = 1.8, 2.0, 2.2, 2.4, 2.6, 2.8 Mpc$, from the top left (left to right) to the bottom right respectively. On the vertical axes is the galaxy number count per square Mpc, n_{rel}, normalized to the total number of galaxies in the cluster. This is plotted for three redshifts $z = 0.36, 0.69, 1.08$. Clearly from the figures, n_{rel} scales with z. . 64

4.9 Variation of the temperature fluctuation with redshift. The right column is the log-log plot of the first column. The rows are plots for 265 GHz, 217 GHz and 145 GHz respectively. This is plotted for three mass bins, $2.0\times10^{14} \leqq M < 2.4\times10^{14}$, $2.4\times10^{14} \leqq M < 3.5\times10^{14}$, and $M \geqq 3.5\times10^{14}$. These mass bins were chosen this way to account for the fact that cluster mass function drops off with redshift. On the vertical axis is the average temperature fluctuation for each of the mass bins, and the errorbars are deviations from the average value (average deviation; a reason why the error bars are so small at high z; few cluster), which for a normal distribution includes 58% of the sample. There is a drop in magnitude of the fluctuations with z, and an increase of the magnitude with cluster mass. The lines are first order polynomial fits 74

6.1 Two low energy photons in a parallel beam stricking the moving electron at an angle θ from the x axis, as seen in the lab frame. 81

6.2 § [6] Geometry of the kSZE as seen in the frame of an observer at rest in the Hubble flow 86

List of Tables

4.1 Fluxes (in mJy) and temperature fluctuations (in K) at z = 0.36 shown for frequencies 145 GHz, 217 GHz and 265 GHz (continues to table 4.3). Cluster mass is in $10^{14} M_{\odot}$. Some rows (chosen randomly) have been omitted since the table contained about 400 rows (too long to be wholly displayed) 67

4.2 Fluxes (in mJy) and temperature fluctuations (in K) at z = 0.36 shown for frequencies 145 GHz, 217 GHz and 265 GHz. Cluster mass is in $10^{14} M_{\odot}$. . 68

4.3 Fluxes (in mJy) and temperature fluctuations (in K) at z = 0.51 shown for frequencies 145 GHz, 217 GHz and 265 GHz. Cluster mass is in $10^{14} M_{\odot}$. It continues to table 4.5 69

4.4 Fluxes (in mJy) and temperature fluctuations (in K) at z = 0.51 shown for frequencies 145 GHz, 217 GHz and 265 GHz. Cluster mass is in $10^{14} M_{\odot}$. . 70

4.5 Fluxes (in mJy) and temperature fluctuations (in K) at z = 0.83 shown for frequencies 145 GHz, 217 GHz and 265 GHz. Cluster mass is in $10^{14} M_{\odot}$. . 71

4.6 Fluxes (in mJy) and temperature fluctuations (in K) at z = 1.08 shown for frequencies 145 GHz, 217 GHz and 265 GHz. Cluster mass is in $10^{14} M_{\odot}$. . 72

4.7 Fluxes (in mJy) and temperature fluctuations (in K) at z = 1.39 shown for frequencies 145 GHz, 217 GHz and 265 GHz. Cluster mass is in $10^{14} M_{\odot}$. . 73

4.8 Typical values of m and C 73

4.9 flux limits 77

4.10 magnitude of ΔT 77

Chapter 1

Introduction

Cosmic microwave background (CMB) radiation was emitted soon after the Big Bang and has been travelling toward us for over 10 billion years. Observing the CMB can therefore give insight into the nature of the universe at very early times and provides a probe of structures between us and the surface of last scattering (the epoch at which the universe cooled enough for photons to decouple from baryons).

Observations of the CMB have been carried out since its discovery by radio astronomers Arno Penzias and Robert Wilson in 1964. The NASA Cosmic Background Explorer (COBE) operated from 1989 to 1996 and detected and quantified the large scale anisotropies of the CMB. More ground and balloon based experiments followed, helping to quantify CMB anisotropies on smaller angular scales than done by COBE. In 2003 the first results from the *Wilkinson Microwave Anisotropy Probe* (WMAP) were released, providing measurements of anisotropies over the entire sky. The best angular resolution achieved by these experiments was that of the BOOMERanG experiment, which was about 10 arcminutes. The current CMB experiments include the Planck Surveyor, launched in May, 2009, and the ground-based experiments: the South Pole Telescope in Antarctica, and the Atacama Cosmology Telescope (ACT).

In this project we considered ACT as our case study. ACT will map about 800 square degrees of the microwave sky at three frequency bands (145 GHz, 217 GHz, 265 GHz)

with angular resolution of about one arcminute. The cosmological signals to be detected are: primary CMB fluctuations, gravitational lensing, and thermal and kinetic Sunyaev Zeldovich Effects (SZE). The survey is expected to map thousands of clusters via the SZE, carrying out blind pointing in the sky and relying on the science of interaction between the CMB photons and high energy hot electrons in the intra-cluster medium to detect the clusters. The photons are inverse Compton scattered causing a shift in the CMB power spectrum. The CMB experiments at such small angular scales suffer from contamination from point sources like infrared galaxies and AGN, as well as from dust in the galactic centre. All these contaminants have to be corrected for to achieve sensible results from CMB surveys. At the observation frequencies of ACT, the main contaminants are the submillimeter point sources (i.e infrared galaxies and quasars).

The aim of the project is to study the space density of infrared-bright galaxies in clusters to account for their contribution to the observed CMB-SZ signals. Infrared-bright galaxies are dusty galaxies with relatively high star formation rates; the UV and optical light from the young stars is absorbed by the dust and then reradiated at infrared wavelengths. The emission components of these galaxies include: stellar emission that comes from mostly the old population stars of at least 10 Gyrs old; the polycyclic aromatic hydrocarbon (PAH) that dominates the mid infrared wavelength; and continuum dust emission that is divided into emission from warm, small dust grains, and the thermal grey-body emission from cold dust.

Surveys such as Spitzer and submillimeter common-user bolometer array (SCUBA; in the James Clerk Maxwell telescope (JCMT)), have greatly improved our knowledge of the distribution of far infrared and sub-mm sources though not enough to be able to model their contamination of the CMB at all redshifts. In this project we access catalogues of galaxies from the millennium simulation database and model the infrared emission from the galaxies using properties given in the simulation. We test our model by comparing the space density of infrared galaxies in the simulation with what is observed. We then study the properties of the modelled infrared galaxies in clusters as well as some galaxy cluster properties, and model the contamination of the SZ signal from clusters by the submillimeter galaxies within clusters.

IR-point source contamination in CMB experiments has been considered by other authors in most of their semi-analytical modeling such as in [16], [11], but until very recently, the IR-bright galaxies have been randomly distributed in simulated maps of the CMB and not correctly positioned in clusters and the large-scale structure, where they are likely to cause more contamination. [52] attempt to cluster the IR-bright galaxies correctly, using a halo model where galaxies are positioned randomly within clusters. This will get the positions roughly correct but in high-resolution CMB experiments a more accurate method may be appropriate. We use complete semi-analytical modelling of the sources which allows us to explore the spatial distribution of the IR-contributions within and near clusters.

1.1 Objectives

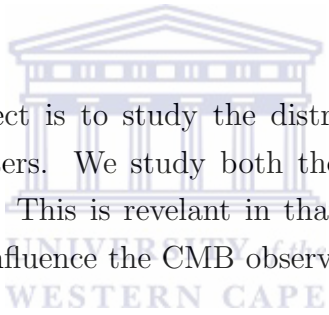

The first objective of the project is to study the distribution of galaxies, particularly infrared-bright galaxies in clusters. We study both the 2 dimensional (2D) and the 3 dimensional (3D) distributions. This is revelant in that we are able to understand the galaxy cluster properties that influence the CMB observations.

The second objective is to compute the flux contribution from the infrared galaxies within clusters using the the observed relation between star formation rate and infrared luminosity. We then compute the magnitudes of temperature fluctuations that result from these fluxes.

Finally, we determine the submillimeter contributions from IR-bright sources as a function of redshift and at different observation frequencies of ACT. We compare these with expected signals from the thermal and kinetic SZ effect. We also consider the residual fluctuations which would remain if the brightest IR-bright sources could be removed from maps using observations at other wavelengths or higher resolution observations.

Chapter 2

Theoretical background

2.1 Introduction

In this chapter we give a theoretical background on the cosmic microwave background radiation and on Compton and inverse Compton scattering, linking it to the Sunyaev Zel'dovich effect in clusters. This is followed by a brief theory of large-scale structure and the initial conditions of N-body simulations. We then give an overview of the millennium N-body dark matter (DM) simulation as well as the semi-analytic modeling that is superposed on the DM simulation to account for the baryonic processes involved in galaxy and large-scale structure formation. Detailed derivations of some sections of this chapter can be found in the Appendix.

2.2 The cosmic microwave background (CMB)

Current observational data strongly supports the Big Bang theory as the best model that explains the way the observable universe started. The most recent evidence comes from the WMAP data that gives the cosmological parameter values close to the predictions from the Big Bang model. This model states that the universe expanded from a primordial hot and dense initial condition at some finite time. At about 10^{-37} seconds the embryonic

universe underwent a stage of cosmic inflation, an exponential growth that smoothed out almost all the inhomogeneities originally created during the big bang. Symmetry breaking is believed to lead to the creation of the elementary particles and setting up of fundamental forces as observed in the present universe. Approximately 10^{-6} seconds after the big bang, the universe was made up of a plasma of photons (thermal radiation), electrons and baryons. The radiation was tightly coupled to "a hot soup" of electrons and baryons through Thomson scattering making the universe opaque to radiation. As the universe continued expanding and cooling, after about 379,000 years (redshift of about 1100) the temperature of the plasma dropped to about 3000 K. At this temperature the electrons and baryons could combine forming stable atoms. The photons decoupled from baryons due to the decrease in free electron density. This phase was thus marked by decoupling followed by recombination, between electrons and baryons and it is generally called *The time of last scattering*. Since the time of last scattering (when the CMB was emitted) the CMB photons travel freely to us, giving us a snapshot of the fluid at that fixed instant in time. As the universe expands, the CMB photons are redshifted, such that the current temperature of the radiation would be about 2.7 K (∼3000K/1100) as supported by observations.

The discovery of the CMB dates back to 1948 when it was predicted by George Gamow, Ralph Alpher and Robert Herman; Alpher and Herman estimated its temperature to be 5 K and after two years they re-estimated it to be 28 K. In 1953 George Gamow estimated 7K and in 1956 revised this to 6K [38]. Other predictions included that by Robert Dicke who called it "radiation from cosmic matter" predicting its temperature to be <20K, but he did not refer to it as "background radiation". In 1960 D. Robert refered to it as "microwave background radiation" and re-estimated its temperature to 40 K [38]. In 1964 A. G. Doroshkevich and Igor Novikov, Soviet astrophysicists, published a brief paper, where they named the CMB radiation phenomenon as detectable. Still in 1964, David Todd Wilkinson and Peter Roll, from Princeton University, began constructing a Dicke radiometer to measure the CMB [13]. In 1965, Arno Penzias and Robert Woodrow Wilson at the Crawford Hill location of Bell Telephone Laboratories in New Jersey found an excess of 3.5 K antenna temperature in their Dicke radiometer, which they had built for radio astronomy and satellite communication experiments. They could not account for the excess temperature, but together with the Princeton group, they confirmed that the temperature excess was due to the microwave background. This discovery won Penzias and Wilson a Nobel Prize in Physics in 1978.

The CMB measurements by the Differential Microwave Radiometer (DMR) instrument on COBE shows it to be isotropic in the sky to roughly one part in 10^5. Its spectrum fits that of a thermal black body radiation. Its specific intensity can therefore be expressed as

$$I_\nu = \frac{2h\nu^3}{c^2}\left(e^{\frac{h\nu}{k_B T_{rad}}} - 1\right)^{-1} \tag{2.1}$$

2.3 Sunyaev-Zel'dovich effect

2.3.1 Inverse Compton scattering (IC)

Inverse Compton scattering occurs when an electron having sufficient kinetic energy compared to a photon interacts with the photon leading to transfer of energy from an energetic electron to a low energy photon. After the interaction, the energy and direction of motion of the photon and electron are usually altered.

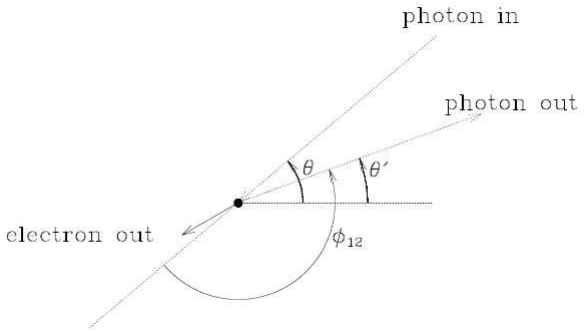

Figure 2.1: [Adopted from [6]] Geometrical illustration of inverse Compton scattering in the rest frame of electron before the interaction. The photon is incident at an angle θ relative to the x axis (direction of motion of the electron). It is deflected by angle ϕ_{12} , and emerges after the scattering at angle θ'. In the observers frame, where the electron is moving with velocity βc along the x axis, the photon changes energy by an amount depending on $\beta = v/c$ and the angles θ and θ'.

Let P be the lab frame in which a photon is incident at an angle θ and P' the rest frame of electron. In the relativistic limit, $\gamma\hbar\omega \ll m_e c^2$. Where $\hbar\omega$ is the energy of the photon

in the rest P frame and m_e is electron mass. According to the Doppler shift formula, the energy of the photon in P' frame will be

$$\varepsilon' = (\hbar\omega)' = \gamma\hbar\omega\,[1 + \beta cos\theta] \tag{2.2}$$

The energy loss rate of the electron in P' is the rate at which energy is radiated by electron and is given by

$$-\left(\frac{dE}{dt}\right)' = \sigma_T c U'_{rad} \tag{2.3}$$

where σ_T is Thomson cross section, c is speed of light and U'_{rad} the energy density of radiation in the rest frame of electron. $\frac{dE}{dt}$ is invariant, thus $\left(\frac{dE}{dt}\right)' \equiv \left(\frac{dE}{dt}\right)$ where $\frac{dE}{dt}$ is in the lab frame, P. We need to derive a transformation of U' to U. The derivation is shown in the appendix 6.1 with the result that

$$U'_{rad} = \frac{4}{3}U_{rad}(\gamma^2 - \frac{1}{4}) \tag{2.4}$$

which gives energy radiation rate of,

$$\left(\frac{dE}{dt}\right) = \frac{4}{3}\sigma_T c U_{rad}(\gamma^2 - \frac{1}{4}) \tag{2.5}$$

as the total energy in the radiation field after inverse-Compton upscattering of low-energy photons. The initial energy of the photons before the upscatter is $\sigma_T c U_{rad}$, so the net energy added to the radiation field is

$$\left(\frac{dE}{dt}\right) = \frac{4}{3}\sigma_T c U_{rad}(\gamma^2 - \frac{1}{4}) - \sigma_T c U_{rad} \tag{2.6}$$

$$= \frac{4}{3}\sigma_T c U_{rad}(\gamma^2 - 1) \tag{2.7}$$

Using the identity $(\gamma^2 - 1) = \gamma^2\beta^2$

$$\left(\frac{dE}{dt}\right) = \frac{4}{3}\sigma_T c U_{rad}\beta^2\gamma^2 \tag{2.8}$$

which for low energy limits reduces to

$$\left(\frac{dE}{dt}\right) = \frac{4}{3}\sigma_T c U_{rad}\beta^2 \tag{2.9}$$

Defining the number of photons scattered per second in the upscatter process as the number of photons encountered per second by the electron, that is $\sigma_T N_{phot} c = \sigma_T U_{rad} c/\hbar\omega_0$ [43], the average energy gained by the photons per Compton collision will be

$$\left\langle \frac{d\epsilon}{\epsilon} \right\rangle = \frac{4}{3}\beta^2 \tag{2.10}$$

and for electrons with a thermal distribution of velocities at temperature T_e

$$\left\langle \frac{d\epsilon}{\epsilon} \right\rangle = \frac{4k_B T_e}{m_e c^2} \tag{2.11}$$

The average fractional change of energy of photons due to Compton scattering (scattering of electrons by high energy photons leading to transfer of energy from high-energy photons to low-energy electrons) is given as in [43]

$$\left\langle \frac{d\epsilon}{\epsilon} \right\rangle = \frac{\hbar\omega}{m_e c^2} \tag{2.12}$$

In normal plasma environments we expect these two scattering processes (Compton and inverse-Compton) to establish an equilibrium distribution if enough time is available for it to do so. At equilibrium, $4k_B T_e = \hbar\omega$, and one process dominates the other depending on whether the electrons are hotter than the photons or vice versa.

2.3.2 Sunyaev-Zel'dovich Effect in galaxy clusters

The typical astrophysical environments in which these Compton and more specifically inverse Compton processes occur are in clusters of galaxies. With a content of hot intracluster gas (high electron temperatures), the background CMB photons undergo scattering within the cluster in a random walk process before finally escaping to the observers line of sight.

This process as already noted before, increases the energy of the CMB photons causing a mis-match between CMB photons and their number density. If this process is given

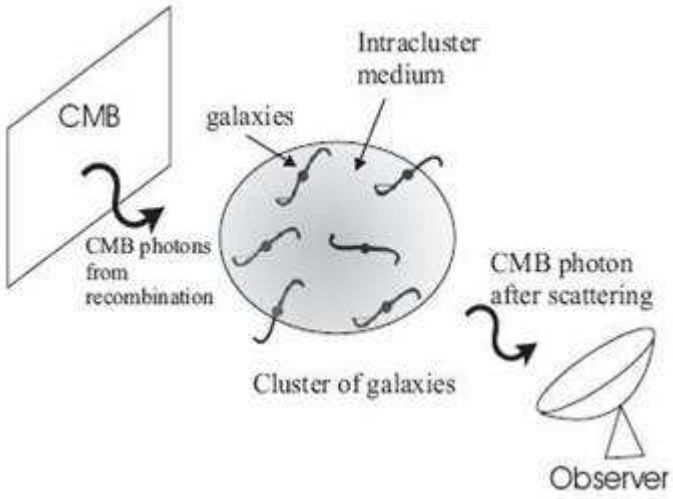

Figure 2.2: The background photons are scattered by the intracluster hot electrons causing a shift in energies of photons, which is observed as a collective effect

enough time and enough scattering (like in the early universe before the epoch of recombination), then we would expect an equilibrium distribution to be set up. In scattering by clusters, there is not enough time for equilibrium distribution to be attained. We therefore need to establish an equation that characterises the photon evolution towards equilibrium distributions. In the non-relativistic limit as that described above, this equation is known as the *Kompaneets equation* after the Soviet scientist who first derived it in 1949.

The Kompaneets equation describes the change in the occupation number, n(ν) by a diffusion process in a non-relativistic limit. Since the equation describes the evolution of the distributions of photons in phase space, n(ν) can therefore be considered as number of photons per state.
The equation is written as

$$\frac{\partial n}{\partial y} = \frac{1}{x^2}\frac{\partial}{\partial x}\left[x^4\left(n + n^2 + \frac{\partial n}{\partial x}\right)\right] \tag{2.13}$$

where $y = \int \left(\frac{kT_e}{m_e c^2}\right)\sigma_T N_e dl$ and $x = \frac{h\nu}{kT_e}$.
The other terms have the following meanings; $\frac{\partial n}{\partial x}$ represents the diffusion of photons along the frequency axis in both directions with respect to their initial energies, n represents the cooling of the photons by recoil effect and n^2 represents the effects of induced Compton scattering which also contributes to the cooling of the photons in cases where the

occupation number is large.

The above equation can be used in various astrophysical applications such as self comptonization in X-ray sources, in which photons are created by bremsstrahlung and in turn strongly comptonized. We also use it in describing distortions of the CMBR background photons after being scattered by intracluster hot gas (electrons). When considering intracluster environments, it is correct to assume that $T_e \gg T_{rad}$, where T_{rad} is the radiation temperature. Since $x \propto T_e^{-1}$, we can ignore the cooling terms (n and n^2). The resulting CMBR photon spectrum after Compton scattering in the non-relativistic limit can thus be computed by solving a simplified Kompaneets equation below.

$$\frac{\partial n}{\partial y} = \frac{1}{x^2}\frac{\partial}{\partial x}\left[x^4\left(\frac{\partial n}{\partial x}\right)\right] \tag{2.14}$$

For a weakly interacting incident CMB radiation, we can substitute $\frac{\partial n}{\partial x}$ and in turn $\frac{\partial}{\partial x}$ for occupation number of a purely Planckian radiation field, that is $n(x) = \frac{1}{e^x - 1}$.
Integrating along the path length through the cluster gives the change of spectral intensity along the line of sight:

$$\frac{\Delta I_\nu}{I_\nu} = \frac{\Delta n}{n} = y\frac{xe^x}{(e^x - 1)}\left(x\frac{e^x + 1}{e^x - 1} - 4\right) \tag{2.15}$$

where $I_\nu = \frac{2h\nu^3}{c^2}\left(e^{\frac{h\nu}{k_B T_{rad}}} - 1\right)^{-1}$ and $T_{CMB} = 2.726$ is the CMB radiation temperature.
The result of the above equation is a shift in the CMB spectrum leading to a decrease in intensity in the Rayleigh-Jeans region of the spectrum (less than about 218 GHz in this case) and an increase in the Wien region as can be seen in figure 2.3

As noted above, the Kompaneets equation is only applicable to non-relativistic limits. The cluster intergalactic medium (of massive/hottest clusters) can be heated to very high temperatures such that the scattering electrons need to be treated relativistically. A detailed derivation of relativistic case is shown by Birkinshaw [6], a brief derivation is shown in the appendix 6.2.
The intensity (radiation spectrum) change at frequency ν for a single photon scatter is

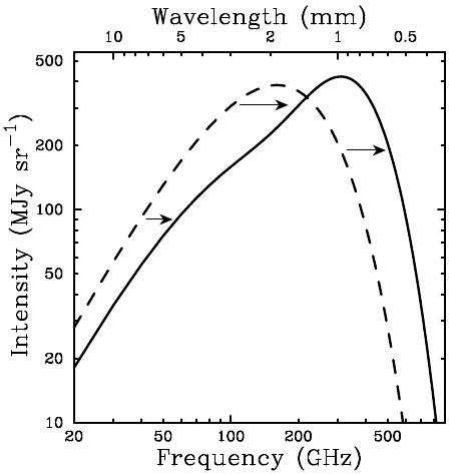

Figure 2.3: §[8] Distortion of the Cosmic Microwave Background spectrum by inverse Compton scattering. The dashed line is the spectrum before scattering and the solid line is after distortion. What is shown is exaggerated for illustrative effects (its for a fictional cluster 1000 times more massive than a typical massive galaxy cluster). The intensity decreases in the Rayleigh-Jeans region of the spectrum and increases in the Wien region

given by (details in the appendix 6.2)

$$\Delta I(\nu) = I(\nu) - I_0(\nu) = \frac{2h}{c^2}\int_{-\infty}^{\infty} P_1(s)ds\left(\frac{\nu_0^3}{e^{\frac{h\nu_0}{k_B T_{rad}}}-1} - \frac{\nu^3}{e^{\frac{h\nu}{k_B T_{rad}}}-1}\right) \tag{2.16}$$

and for multiple scatter (where photons are scattered 0, 2, or more times)

$$\Delta I(\nu) = I(\nu) - I_0(\nu) = \frac{2h}{c^2}\tau_e\int_{-\infty}^{\infty} P_1(s)ds\left(\frac{\nu_0^3}{e^{\frac{h\nu_0}{k_B T_{rad}}}-1} - \frac{\nu^3}{e^{\frac{h\nu}{k_B T_{rad}}}-1}\right) \tag{2.17}$$

The difference between equations 2.16 and 2.17 is that in the multiple scatter case, the resulting intensity change is as that of a single photon scatter but has an amplitude reduced by a factor τ_e, such that the resulting intensity change is reduced by a factor τ_e from that of a single photon scatter. Equations 2.15 and 2.17 (derived in the appendix) give the same intensity change profiles but with differences in amplitudes as seen in figure 2.4

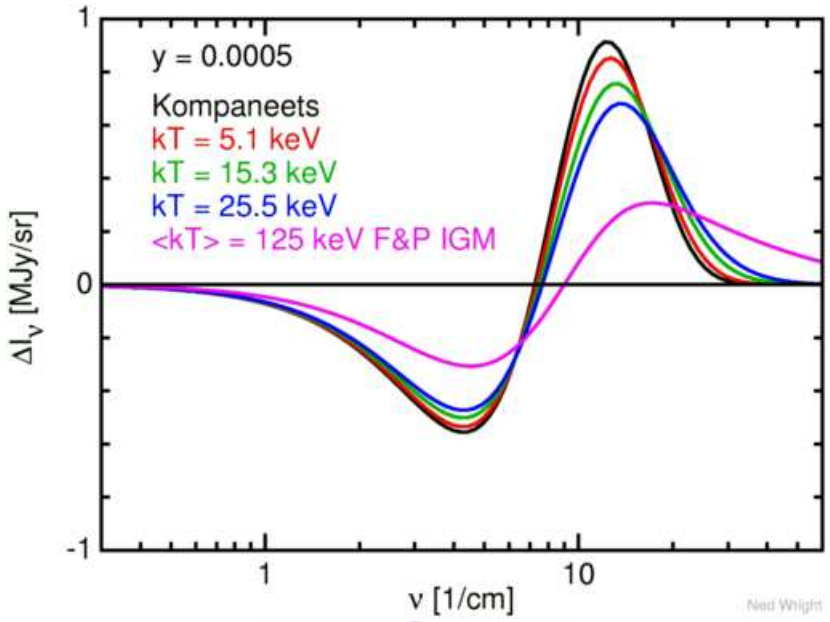

Figure 2.4: § [49] The spectral distribution of ΔI_ν for $y = 0.0005$ for five different conditions, the Kompaneets limit with kT/mc^2 close to zero, and four curves with kT of 5.1, 15.3, 25.5, and 125 Kev, showing the difference in amplitudes for relativistic and nonrelativistic distributions

Equations 2.15 and 6.20 can be rewritten as,

$$\triangle I(x) = I_o y g(x) \tag{2.18}$$

where

$$I_o = \frac{2h}{c^2}\left(\frac{k_B T_{rad}}{h}\right)^3$$

$$y = \int n_e \sigma_T dl \frac{k_B T_e}{m_e c^2}$$

and $g(x)$ is the profile of the spectrum,

$$g(x) = \frac{x^4 e^x}{(e^x - 1)^2}\left(x\frac{e^x + 1}{e^x - 1} - 4\right) \tag{2.19}$$

The corresponding change in radiation temperature due to the scatter is

$$\Delta T_{th} = T_0 y \left(\frac{x(e^x + 1)}{e^x - 1} - 4\right) \tag{2.20}$$

which for the Rayleigh-Jeans part of the spectrum ($x \ll 1$) approximates to

$$\frac{\Delta T_{th}}{T_0} \simeq \frac{\Delta I_\nu}{I_0} \simeq -2y\left(\frac{x}{2}+1\right) \tag{2.21}$$

2.3.3 Kinetic SZE

The Sunyaev-Zel'dovich effect explained above is purely from exchange of thermal energy between hot galaxy cluster electrons ($T_e \sim 10^8 K \sim 5keV$) and cold CMB ($T_{CMB} \sim 3K \sim 200\mu eV$) causing a non-thermal change in the CMB spectrum (distribution becomes 'colder' at lower frequencies and 'hotter' at higher frequencies). This effect is thus known as the *thermal Sunyaev-Zel'dovich Effect (tSZE)*. As seen in the above explanation, $tSZE$ is proportional to the intra-cluster medium (ICM) pressure, $n_e T_e$ and it dependends on the angular diameter distance $d_A(z)$, which is nearly constant at high z (making it nearly independent of z) hence a robust indicator of gas properties.

The other SZE results from the bulk motion of a cloud of electrons in a cluster with respect to the CMB rest frame. The cluster bulk velocity causes a new (on top of the tSZ) distortion (Doppler effect) on the CMB spectrum. This effect is called the *kinetic Sunyaev-Zel'dovich effect* (kSZE). If v_{pec} is the cluster velocity along the line of sight to the cluster, in the non-relativistic limit, this will lead to a thermal (due to thermal systematic motion of the electrons) distortion of magnitude $\tau_e\left(\frac{v_{pec}}{c}\right)$ [57]. For the relativistic limit, the kSZE results from the Lorentz boost to the electrons provided by the bulk velocity [51]. Sazonov & Sunyaev derived explicitly an expression for the relativistic limit showing that the leading term is of order $(K_B T_e/m_e c^2)\,(v_{pec}/c)$, which for a 10keV cluster with a peculiar velocity of 1000 km/s, has an effect of about 8% correction to the non-relativistic term [51]. The other higher oder terms are $(K_B T_e/m_e c^2)^2\,(v_{pec}/c)$ which is only about 1% of the non-relativistic kSZE and $(v_{pec}/c)^2$ which is only about 0.2% [8] [6].
We need to derive an equation for the change in specific intensity caused by the kSZE. The full derivation of the intensity change is in appendix 6.3
From the appendix 6.3, the fractional intensity change due to kSZE is given by,

$$\frac{\Delta I_\nu}{I_\nu} = \tau_e \int_{-1}^{+1} d\mu_1 \frac{3}{8}(1+\mu_1^2)\left(\frac{e^x-1}{e^{x_2}-1}-1\right) \tag{2.22}$$

where $x_2 = x\gamma_z^2(1+\beta_z)(1-\beta_z\mu_1)$ and $x = \frac{h\nu}{k_B T_{rad}}$, and $\beta_z = v_{pec}/c$ in z direction.

For small β_z, by expanding the integral in powers of β_z, and neglecting odd terms of the integrand, we end up with

$$\frac{\Delta I_\nu}{I_\nu} = -\tau_e \beta_z \frac{x e^x}{e^x - 1} \tag{2.23}$$

and the corresponding changes in specific intensity and brightness temperature become

$$\Delta I_\nu = -\beta \tau_e I_0 \frac{x^4 e^x}{(e^x - 1)^2} \tag{2.24}$$

$$\Delta T_{RJ} = -\beta \tau_e T_{rad} \frac{x^2 e^x}{(e^x - 1)^2} \tag{2.25}$$

The negative sign implies that there will be a decrease in radiation temperature and in the specific intensity of the CMBR. kSZE is an additional and smaller effect compared to the tSZE as illustrated by the spectral profile in the figure 2.5.

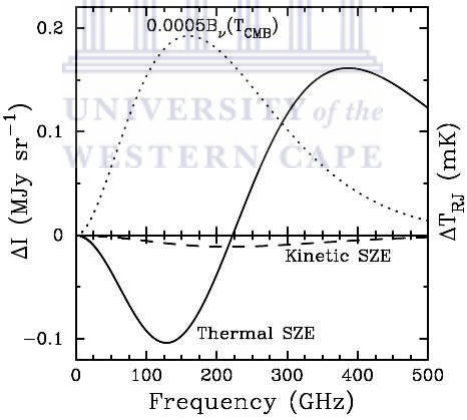

Figure 2.5: § [8] The spectral distortion of the CMB spectrum by SZEs. The cluster properties used to calculate the spectra are an electron temperature of 10 keV, a Compton y parameter of 10^{-4} , and a peculiar velocity of 500 km s^{-1}. The dotted line is a 2.7 K thermal spectrum for the CMB intensity scaled by 0.0005. The kSZE, the dashed line is much smaller than the tSZE, the solid line.

2.3.4 The relation between observed SZE fluxes and the temperature fluctuations

The SZE is a very powerful tool for probing galaxy cluster cosmology because it is easier to detect clusters beyond $z \sim 1$ using the SZE than it is using X-ray or optical surveys. This can be illustrated clearly by considering the following two reasons: the first comes from the fact that the X-ray cluster emissivity drops quite rapidly from the cluster centre to its peripheries, it is proportional to n_e^2 where n_e is the electron density. This means at relatively higher redshifts, even rich clusters with denser cores will still have a small apparent angular size. In contrast, the SZE flux scales as n_e, making it less dependent on the cluster electron density profile for isothermal clusters. The second reason can be explained by comparing the fluxes.

The total SZE flux can be computed by integrating the change in specific intensity induced by the SZE over the solid angle, $d\Omega$ subtended by the cluster

$$S_T(\nu) = \int_{cluster} \Delta I(\nu, \vec{\theta}) d\Omega \tag{2.26}$$

where $\Delta I(\nu, \vec{\theta}) = I_0 g(x) y$, I_0, $g(x)$ and y follow their usual definitions. If the cluster is assumed to be isothermal, then $S_T \propto \int d\Omega \int n_e(\vec{\theta}) dl$ where dl is the path-length through the cluster. By assuming that the gas is composed of only ionised hydrogen, this can then be transformed to angular diameter distance as,

$$D_a^{-2}(z) \int dV n_e(\vec{\theta}) = D_a^{-2}(z) \frac{M_{gas}}{m_p} = D_a^{-2}(z) \frac{f_b}{m_p} M$$

where M is total cluster mass, f_a is the baryon fraction and m_p is the proton mass. The SZE flux thus becomes

$$S_{SZE} = \frac{3.78 g(x) f_b T M_{15}}{D_a^2(z)} \tag{2.27}$$

T is in Kelvin, M_{15} in $10^{15} M_\odot$, $D_a(z)$ in Mpc, and the flux in mJy ($1mJy = 10^{-26} ergs^{-1} Hz^{-1} cm^{-2}$). From equation 2.27 we find out that the SZE flux is proportional to $D_a^{-2} = \left(\frac{D_m}{1+z}\right)^{-2}$ (D_m is the comoving distance). The X-ray flux on the other hand is proportional to $D_L^{-2} = (D_m(1+z))^{-2}$ (D_L being the luminosity distance). The ratio $D_a^2(z)/D_L^2(z)$ goes like $(1+z)^{-4}$, meaning that the SZE flux drops a factor $(1+z)^{-4}$ slower than the X-ray

flux, giving SZE surveys an advantage over X-ray surveys.

The kinetic SZE as noted earlier, for the non-relativistic limit, is a pure thermal distortion of magnitude

$$\frac{\Delta T_{SZE}}{T_{rad}} = -\tau_e \frac{v_{pec}}{c} \tag{2.28}$$

where $T_{rad} = 2.73K$ is CMBR temperature and v_{pec} is the peculiar velocity along the line of sight. We can therefore relate the change in specific intensity due to kSZE, $\Delta I(\nu, \vec{\theta})$ with temperature fluctuation as

$$\Delta I(\nu) = I_0 h(x) \left(\frac{\Delta T}{T_{rad}}\right) \tag{2.29}$$

$$I_0 = \frac{(k_B T_{rad})^3}{(hc)^2} = 2.7 \times 10^{11} \frac{mJy}{str}$$

and the spectral dependence $h(x)$ is

$$h(x) = \frac{x^4 e^x}{(e^x - 1)^2} \tag{2.30}$$

where x has the usual definition of the dimensionless frequency $x = h\nu/(k_B Trad) \approx \nu(GHz)/56.8$

If θ is the resolution per pixel in arcminutes, then the solid angle, $d\Omega = 8.4616 \times 10^{-8}(\theta)^2 str$. The SZE flux per pixel thus becomes

$$S_{SZE}(\nu) = 2.7 \times 10^{11} \frac{\Delta T}{T_{rad}} h(x) d\Omega \frac{mJy}{str} \tag{2.31}$$

$$= 8.369 \times 10^{-3} h(x) \frac{\Delta T}{\mu K} \left(\frac{\theta}{1'}\right)^2 mJy \tag{2.32}$$

or in terms of the temperature fluctuation,

$$\Delta T = 1.2 \times 10^2 \left(h(x) \left(\frac{\theta}{1'}\right)^2\right)^{-1} \left(\frac{S_{SZE}(\nu)}{mJy}\right) \mu K \tag{2.33}$$

The typical temperature fluctuation that results from the kinetic SZE is of order of tens of microkelvin.

We can use equations 2.31 and 2.33 to estimate the minimum flux and ΔT limits expected

to be achieved by any SZ survey (e.g ACT).

2.4 The standard cosmological model

In the standard cosmological model, the universe is isotropic and homogenous on large scales and is described by a Friedman-Robertson-Walker metric. Since the big bang, the space has been expanding in a way that is determined by the nature of its contents. Recent studies of cosmology clearly show that the expansion of the universe is accelerating, with the first evidence coming from Type Ia supernova redshift measurements (where the the observed supernova generally appear redder than they should actually be - indicating accelerated recession) and further evidence from the cosmic microwave background (CMB) power spectrum and from large scale structure studies [32]. From the CMB it can be shown that the universe is near to spatially flat and that matter makes up about a quarter ($\Omega_m \approx 0.27$) of the density. These observations lead to a conclusion that the dominant contribution to the energy density of the universe appears to exist in an unclustered form now generally termed as "dark energy". The nature of this energy has a wide range of implications, from cosmology to particle physics and fundamental physics. The main two models that have been adopted to explain this kind of energy are: the 'lambda cosmological constant', which was introduced by Einstein, such that it contributes a present-day fraction of energy density $\Omega_\Lambda = 0.73 \pm 0.04$. In this model, Λ acts as a 'repulsive gravity' that is driving cosmic expansion to phase of acceleration. The second model is that of 'quintessence (Q model), in which dark energy is considered to be a dynamic scalar field. In the quintessence model, the predictions are usually characterised in terms of the dark energy equation of state $w(z) = \frac{P}{\rho}$, where for the cosmological constant model, $w(z) = 1$ at all epochs. The equation of state can be parameterized as $w_x(z) = w_0 + w_1 z$.

2.5 Galaxy clusters

Clusters of galaxies have high concentrations of galaxies making them a suitable environment for galaxy-galaxy, galaxy-intergalactic medium interactions. The kind of interactive processes observed in galaxy clusters include: galaxy mergers and galaxy harassment, where two or more galaxies moving with relatively high orbiting speed (typically of 500 km/s) encounter each other on flybys. Harassment leaves morphologies of the galaxies involved disturbed, if not entirely changed. It also induces new bursts of star formation. Asymmetrical galaxies, disturbed galaxies, warps, bars and tidal tails can all be produced through galaxy harassment. The other form of interaction is between galaxies and the cluster environment, which include ram pressure stripping (gas of a galaxy moving within its cluster may be removed through interaction with the intra-cluster medium), and a process known as strangulation (gas of a galaxy falling into the cluster for the first time escapes to the inter-galactic medium due to tidal effects). Due to the interactive environments that galaxy clusters present, we expect to observe some regions with starbursts (due to interactions), hence brighter in FIR/sub-mm wavelengths. Giard, Montier, Pointecouteau and Simmat (2008) carried out a study of the infrared luminosity of galaxy clusters, to find out the main contributors to the infrared luminosity, either the intracluster dust or the galaxy components. They quantified infrared emission from galaxy clusters in two processes with different physical origins and consequences: if emission is from galaxies, it will be correlated with total star formation rate, which provides a net energy contribution to the immediate environment. Emission from intracluster dust is a cooling agent that can accelerate the condensation of diffuse baryons into stars and galaxies [25]. In their study, they deduced a dust-to-gas mass abundance in intracluster gas (from infrared luminosity and by assuming that all the infrared luminosity is from intracluster dust emission) of $Z_d \simeq 5 \times 10^{-4}$. Other constraints on the abundance of intracluster dust gives $Z_d \simeq 10^{-5}$, hence ruling out the idea that infrared emission is from intracluster dust. On the other hand, they found out that infrared luminosity mimics the evolution of the star formation rate with redshift, leading to a conclusion that the main contribution to infrared luminosity is from the ongoing star formation in the member galaxies. We therefore aim at quantifying the contribution from these (mainly faint) star forming (infrared) galaxies and determine their contamination of the SZE signal.

There is a great deal of literature on the galaxy populations in clusters which we do not attempt to summarize here as it is beyond the scope of a NASSP MSc project. We do however provide examples of the cosmological constraints that can be obtained from clusters of galaxies. The observed abundance of rich clusters of galaxies strongly constrains the matter density (Ω_m) and σ_8, which is the *rms* mass fluctuations on 8 h^{-1} Mpc scale (or the normalisation of the matter power spectrum on scales of 8 h^{-1} Mpc). The observed present-day abundance gives $\sigma_8\Omega^{0.5} \simeq 0.5 \pm 0.05$ [1]. The constraint is degenerate in Ω and σ_8, allowing a model with $\Omega = 1$, $\sigma_8 \simeq 0.5$ and one with $\Omega \simeq 0.25$, $\sigma_8 \simeq 1$. By measuring the mass of a cluster and normalizing by its luminosity, we obtain the mass-to-light ratio, M/L_B (L_B being the total blue luminosity of the cluster), which after integrating over the luminosity density of the universe, gives a dynamical mass density, Ω_{dyn}. Observations give $M/L_B \simeq 300 \pm 100h$ and the corresponding $\Omega_{dyn} \simeq 0.2$ on scales of about 1.5 h^{-1} Mpc. This value assumes that all galaxies have the same M/L_B ratio [2]. This means that if mass follows light on large scales (mass distribution is not biased), then a universal value of $\Omega_m \simeq 0.2$ is valid. If the universe has a critical density (that is $\Omega_m = 1$)as required by theory, then most mass must be unassociated with galaxies or light but exists in voids where there is no light. In other words $\Omega_m = 1$ implies a bias in distribution of mass, and light [2]. By correctly determining the cluster mass function (the number density of clusters above a threshold mass M), $n(> M)$, and its *evolution* with redshift (the rate of evolution), one can constrain the cosmological parameters (Ω_m and σ_8) and distinguish between models (that is between low-density, $\Omega_m < 1$ and standard $\Omega = 1$ models). Bahcall and Cen found that the standard $\Omega = 1$ cold dark matter models cannot reproduce well the observed cluster mass function [1]. Figure 2.6 (adopted from Bahcall et al 1997) shows the evolution of the abundance of massive clusters with mass $M(\leq R = 1.5h^{-1}Mpc) \geq 6.3 \times 10^{14}h^{-1}M_{\odot}$. From the figure we can straight forwardly deduce that, the observational data supports the low-density universe, and more specifically the Lambda Cold Dark Matter (LCDM) cosmology. From the figure, we can also see that the evolution of the abundance of high-mass clusters breaks the degeneracy between Ω_m and σ_8 that exists at $z \simeq 0$ [2], and quantifies the two parameters. This is because the abundance at a given redshift gives Ω_m and the rate of evolution gives σ_8.

In summary, SZE surveys will provide huge catalogues of galaxy clusters because of the redshift independence of the effect. Secondly, it will provide relatively accurate measures of galaxy cluster properties necessary to distinguish between cosmologies and quantify

cosmological parameters. It is therefore important to carry out studies that can help refine the accuracies of such surveys, like studying the possible systematic errors which will be involved. Above the $tSZE$ null, the signal from the faint sub-mm galaxies within clusters acts to boost the SZE signal making cluster masses deduced from the SZE distortion larger than the actual cluster mass (the reverse is true for observation frequencies below the $tSZE$ null). This effect in turn boosts clusters from low-mass bins into high-mass bins, and increases the total number of clusters in the sample above a certain mass limit [44]. That is, if M_{real} is the real mass of the cluster, the measured mass, M would then be

$$M = M_{real}(1 + s) \tag{2.34}$$

Where $s \geq 0$ is due to the systematic error and can be a constant in this case. The signal from the faint sub-mm galaxies can therefore be treated as a systematic error in the SZE surveys.

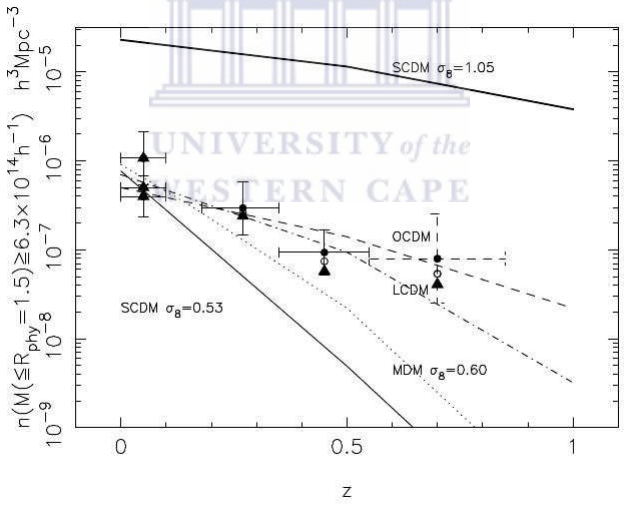

Figure 2.6: Adopted from Bahcall et al (1997). Shows the evolution of abundance of massive coma-like clusters with redshift. Line represent predictions from different models obtained from large-scale cosmological N-body simulations ($400h^1$Mpc box size) for different cosmologies: Standard Cold Dark Matter (SCDM,$\Omega_m = 1$, COBE normalised: §17, $\sigma_8 = 1.05$), SCDM with $\sigma_8 = 0.53$ (normalised to the present-day cluster abundance; Mixed Dark Matter (MDM: hot + cold), Open CDM (OCDM,$\Omega_m = 0.35$, $\sigma_8 = 0.8$), and Lambda CDM (LCDM, $\Omega_m = 0.4$, $\Lambda = 0.6$, $\sigma_8 = 0.8$. The data points are from Canadian Network for Observational Cosmology (CNOC) survey, which was originally designed to differentiate between the Ω=1 and $\Omega \simeq 0.2$ cosmologies.)

The other constraint expected from the abundance and redshift distribution (dN/dz) of galaxy clusters in future SZE cluster surveys (combined with the spatial power spectrum ($P_c(k)$)of the same clusters), is on the evolution of the dark energy equation of state, $w(z)$. Cluster surveys can also constrain the nature of dark energy. Figure 2.7 shows the dependence of evolution of cluster abundance on w_x where $w_x(z) = w_0 + w_1 z$.

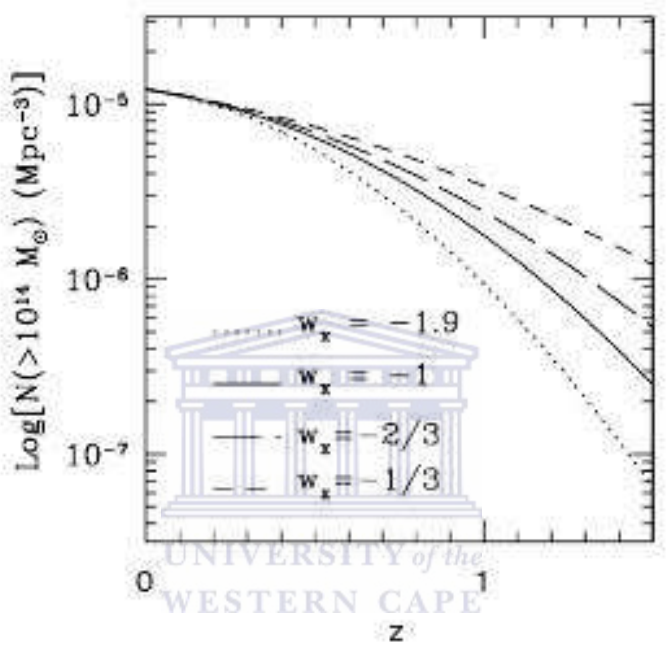

Figure 2.7: § [15] Number density of haloes with $M \geq 10^{14} M_{\odot}$ plotted as a function of redshift z for various Q models (with different equation of state parameters, $w_x(z)$). The other cosmology used is $\Omega_m = 0.3$, $\Omega_\lambda = 0.7$, $H_0 = h\ 100\ kms^{-1}Mpc^{-1}$ with $h = 0.7$, and the rms matter density fluctuation within a sphere of radius 8 h^1 Mpc linearly extrapolated to today, $\sigma_8 = 0.8$.

2.6 Structure evolution in the Universe and the initial conditions

The millennium simulation is an N-body simulation intended to mimic different epochs of the universe as it evolved from its very early stages, from the time the cosmic microwave

background radiation (CMBR) was just emitted, that is about 379,000 years after the big bang. It was created and run for the first time in 2005 by the *Virgo Consortium*, a collaboration of astrophysicists from Germany, the United Kingdom, Canada, Japan and the United States [56]. N-body simulations simulate massive particles, tracking their interaction under the influence of physical forces, the major one being the mutual gravitational forces. In this kind of simulation, the forces are integrated numerically rather than making approximations as is always done in analytical calculations. N-body simulations are very useful in studying the non-linear processes in the formation and growth of structure in the universe.

Before reviewing the the millennium simulation in detail, a brief review of the initial conditions and the science of structure evolution is necessary.
First we note that the relevant components of the universe include dark matter, the gas (nuclei and electrons), the cosmic microwave background photons, and the cosmic background neutrinos. These components played a role in the early stages of the universe, before recombination. Initially, before recombination, the Universe was ionized (gas plasma and photons), photons provided enormous pressure and restoring force causing the perturbations to oscillate as acoustic waves. At recombination, the universe cooled and protons recombined with electrons allowing the photons to decouple from the baryons, such that after recombination, the universe is neutral. The phase of oscillation at t_{rec} affects the late-time clustering amplitude [20].

Considering each initial overdensity (of dark matter, gas, neutrinos and photons) as an excess in pressure that launches a spherical sound wave which expands in spherical shells, then at recombination, the universe is a superposition of these shells. Since dark matter is denser than any other component, the resulting shells will have an overdensity at the centre purely due to dark matter and at the edge due to both gas and dark matter, but mainly gas. Theoretical models of the processes expected to have occurred then predict the radius of these spherical shells to be about 150 Mpc. After recombination, when the sound wave stalls, the overdensity in the shell (gas) and in the original centre (dark matter) both seed the formation of galaxies. The effect of this physics is today observed as a bump in the correlation function plot of the galaxy distribution in redshift space. In Fourier space, the bump can be seen as wiggles whose wavelength scale is determined by

the sound Horizon (the distance travelled by the sound wave from the time of Big Bang to recombination). This phase of the universe also left imprints on the CMBR, giving rise to prodigious structure in the CMBR anisotropies now observed as the Acoustic peaks in the CMBR power spectrum.

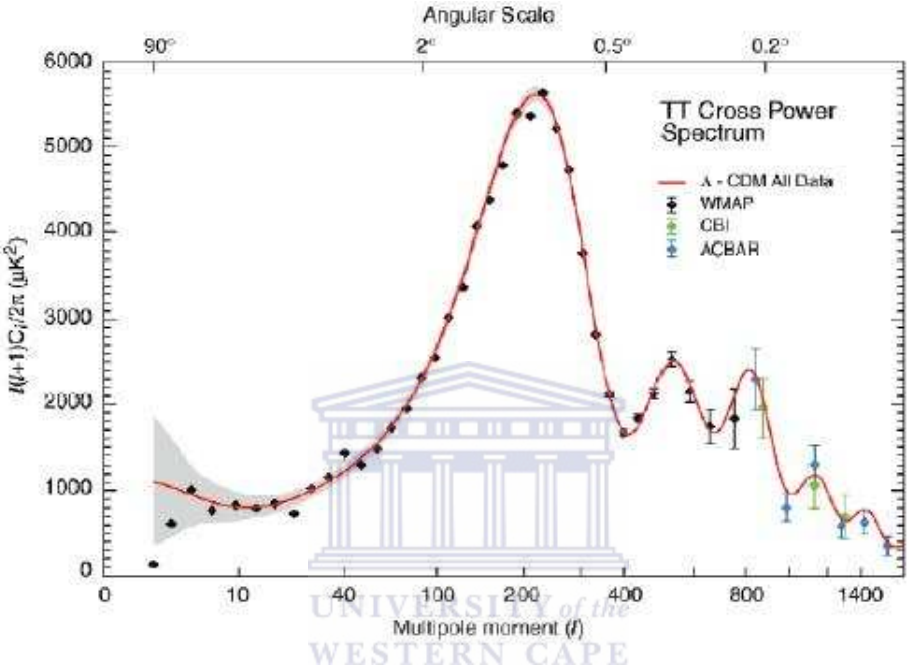

Figure 2.8: § [4] The WMAP angular power spectrum: the vertical axis can be taken as the amplitude of temperature fluctuation as observed in the sky and the horizontal axis (multipole moment) is the angular scale on the sky ($\simeq 180/l$ degrees). The acoustic peaks can be clearly seen, the first one at about 1^o

The galaxies, and the entire large scale structure are therefore believed to have formed by gravitational amplification of small primordial perturbations/fluctuation plus other physical processes such as radiative cooling, photoionization, recombination, radiative transfer and generally adiabatic gas dynamics [47] [46]. Using perturbation theory and approximation schemes, the evolution of perturbations in the high redshift universe can be studied analytically. At lower redshifts, the processes become more complex and non-linear. The nonlinearity of scales is defined by the density contrast of matter in the universe given by, $\delta = \rho/\tilde{\rho} - 1$, where $\tilde{\rho}$ is the average density of the universe. If this value for a given scale is very close to and/or greater than unity, then all physical processes operating at that scale are treated as nonlinear. For example, on galaxy scales now, the matter density ρ is thousands of times larger than $\tilde{\rho}$, but at the time of decoupling of matter and radiation,

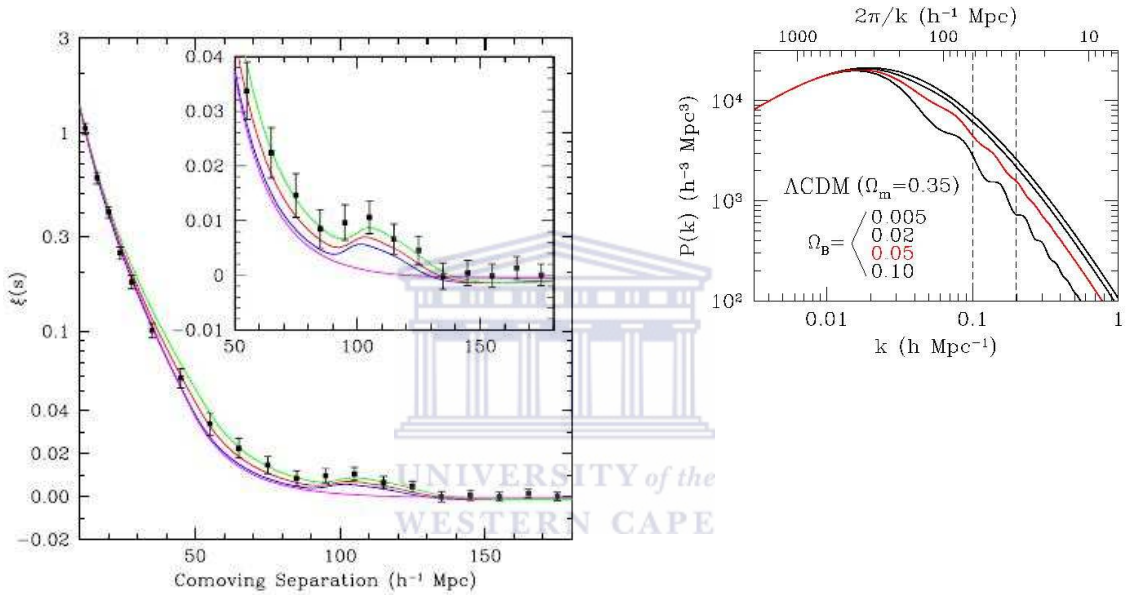

Figure 2.9: § [21] [53] The large-scale redshift-space correlation function of the SDSS LRG sample (k is an equivalent of inverse of spatial scale factor or wavelength) for different models of $\Omega_m h^2 = 0.12$ (top, green), 0.13 (red), and 0.14 (bottom with peak, blue). The bump exists at about $100h^{-1}$ Mpc as predicted by the physics before recombination. In Fourier space, this can be seen as wiggles with wavelength scale determined by the sound Horizon.

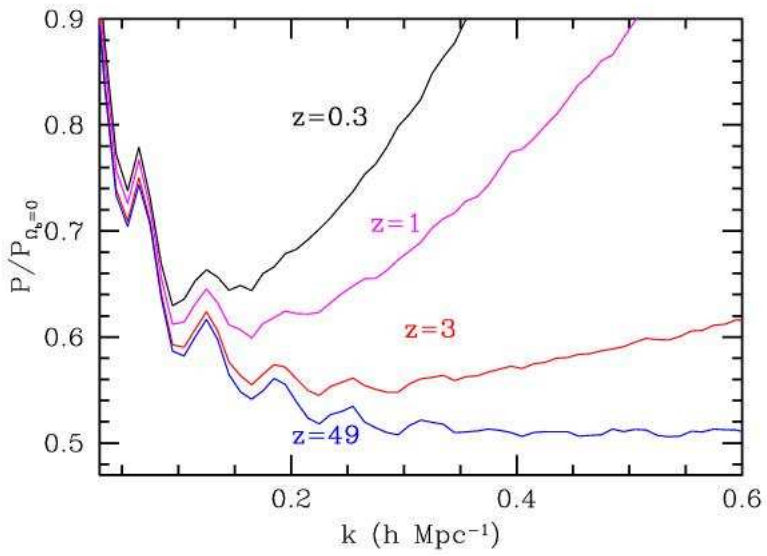

Figure 2.10: adopted from Meiksen & White (1997). The matter power spectrum at various redshifts in Fourier space. The power is divided by a real-space zero-baryon power spectrum (matter power spectrum without wiggles). The oscillations are the *Baryon Acoustic Oscillations*. The effect of nonlinear gravitational collapse is demonstrated. It is a function of both redshift and scale factor or wavelength. Taking spherical shells in the sky, at lower redshifts, nonlinearity exists up to larger scales compared to higher redshifts. e.g at $z = 1$, the linear regime exists up to $k < 0.2hMpc^{-1}$ corresponding to 2-3 oscillations and at $z = 3$, its up to $k < 0.5hMpc^{-1}$, about 4 oscillations

it was much smaller than unity, meaning processes operating at these scales in the early universe can be analytically studied, unlike in the present universe. This also implies that the scales at which non-linear gravitational collapse occurs evolves (increases) with time. Nonlinearity has an observable effect on the matter power spectrum (and the baryon acoustic oscillations). It increases the power spectrum on small scales and tends to smear out the amplitude of the acoustic oscillations. This can be clearly observed in figure 2.10, and we can determine scales at which it occurs (if other effects are corrected for) that is at $z = 1$, linear regime exists up to $k < 0.2hMpc^{-1}$ corresponding to 2-3 oscillations and at $z = 3$, it is up to $k < 0.5hMpc^{-1}$, about 4 oscillations.

To study the evolution of physical processes and especially gravitational collapse on scales of nonlinearity, we need numerical simulations. The millennium simulation tracks $N = 2160^3 \simeq 1.0078 \times 10^{10}$ particles from redshift $z = 127$ to the present in a cubic region

$500h^{-1}Mpc$ on the side. Here h as usual is Hubble's constant in units of $100\text{kms}^{-1}\text{Mpc}^{-1}$ and the expansion factor of the universe relative to the present is $1+z$ [56]. It simulates the properties of universe at different redshifts using the dominant mass component, the cold dark matter, which is assumed to be made of elementary particles that interact only gravitationally. The dark matter is thus taken to be a collisionless fluid represented by a set of discrete point particles.

The first step considered (initial condition) is the background cosmological model, which for the millennium simulation was a spatially flat Robertson-Walker universe and lambda cold dark matter model. That is $\Omega_{Total} = 1$, where $\Omega_m = \Omega_{dm} + \Omega_b = 0.25$, $\Omega_b = 0.045$ is the baryon density of the universe at present in units of critical density for closure, $\rho_{crit} = 3H_0^2/(8\pi G)$, Ω_{dm} is dark matter density, and Ω_m is the total matter density. Other cosmological parameters defined include $h = 0.73$, $\Omega_\Lambda = 0.75$ (which is the density of dark energy at present still in units of critical density), $n = 1$, and $\sigma_8 = 0.9$ [56]. The parameters used are obtained from a joint analysis of the 2dFGRS and first year WMAP data [4].

The second initial condition is the specification on the statistical nature of the primordial fluctuations from which structure seeded. The process considered in the millennium simulation to have generated the fluctuations is *inflation* Guth (1981). Inflation predicts Gaussian fluctuations, which are simple to work with because they are specified fully by one function, the power spectrum $P(k)$, and in this model the fluctuations are set right from the beginning (around 10^{-35}s after the Big Bang). Non-gaussian models on the other hand are a bit more complex, they require more information than just the power spectrum and are costly in computation [5].

The positions, and velocities of the dark matter particles are determined from the moment the linear density fluctuation field has been specified, at the initial time, which is $z = 127$ for the millennium simulation. The particles' positions and velocities are displaced from a uniform cubic box of $500h^{-1}Mpc$ using the Zel'dovich (1970) approximation. That is

$$\vec{x} = \vec{q} + D(t)\vec{\psi}(\vec{q}), \quad \vec{v} = a\frac{dD}{dt}\vec{\psi} = aHfD\vec{\psi} \tag{2.35}$$

Where $\vec{q}$ denotes the unperturbed position, $D(t)$ is the growth factor of the linear growing

mode, and $f = d\ln D/d\ln a \approx \Omega^{0.6}$ is the logarithmic growth rate. $\vec{\psi}$ is the displacement field [5]. The particles are evolved under gravity in an expanding background using a leapfrog integration.
There is also need to constrain the matter power spectrum, $P(k)$ in such simulations. $P(k)$ is generally given by

$$P(k, t_i) = Ak^n |T(k, t_i)|^2 \tag{2.36}$$

where $n = 1$ for the millennium simulation as noted before, $T(k, t_i)$ is the transfer function for cold dark matter, and A is the amplitude of the primordial power spectrum, usually obtained through physical normalisation using the CMB data.

2.7 The millennium simulation

2.7.1 Dark matter simulation

The millennium simulation, carried out with the GADGET2 code, uses the "TreePM" method to evaluate the gravitational forces between particles. TreePM is basically a "tree" algorithm or hierarchical multipole expansion combined with a classical, Fourier transformation particle-mesh method. The tree algorithm computes short-range forces by dividing space recursively into a hierarchy of cells, each containing one or more particles. That is if a cell of size s and distance from the point where the gravitational force is to be computed, d, satisfies $s/d < \theta$, the particles in this cell are treated as one pseudoparticle located at the centre of mass of the cell [5]. The PM algorithm is based on representing the gravitational potential on a cartesian grid, and solves the Poisson equation on this grids. It works by first computing mass density, $\rho(\tilde{x}, t)$ on a grid, solves the Poisson equation for the gravity field, and the gravity field is then finally interpolated back to the particles.

The simulation stored the full particle data at 64 output time slices each of size 300 GB, totalling a raw data volume of about 20 TB. The output of the simulation include the

friends-of-friends (FOF) group catalogues. The FOF groups are defined as identity classes in which any pair of particles is identified as members of the same group if their separation is less than 0.2 of the mean particle separation [56]. FOF groups can be initialised with each particle in its own single group, then testing all possible particle pairs. If a pair satisfying the condition is found and at the same time each of the particles lies in different groups already present, then the groups are linked to a common group. The FOF group finder represents groups as link-lists (head, tail, and length). Each output of the simulation is therefore a group catalogue with at least 20 particles in each group (FOF haloes). Since galaxies form in subhaloes within a FOF group, we therefore need to identify the subhaloes to be able to follow the fate of the infalling galaxies. A post processing algorithm, SUBFIND is applied to achieve this; SUBFIND subjects each dark matter halo containing more then 20 particles to a gravitational unbinding procedure, and its basic physical properties like angular momentum, velocity dispersion, maximum of its rotation curve, etc are determined [56][11].

The virial mass for the FOF haloes was computed using the spherical-overdensity approach, the boundary being at the radius which encloses a mean overdensity of 200 times the critical value. The relation between the virial mass, radius and circular velocity of a given halo at a redshift z is defined as;

$$M_{vir} = \frac{100}{G} H^2(z) R_{vir}^3 \quad = \frac{V_{vir}^3}{10GH(z)} \tag{2.37}$$

where $H(z)$ is the Hubble constant at z.

The final output had 17.7×10^6 FOF groups at $z = 0$, the maximum being 19.8×10^6 at $z = 1.4$ when groups were more abundant but of lower mass on average. At $z = 0$ there was a total of 18.2×10^6 haloes, with the largest FOF group containing 2328 of them.

Merger trees were then built to characterise the structural evolution. The merger trees contain details of how haloes grow as the universe evolves.They are defined by identification of the progenitor and a descendant. A unique descendant is defined for each halo and subhalo, and a given halo can have several progenitors. Details can be found in Springel et al (2005).

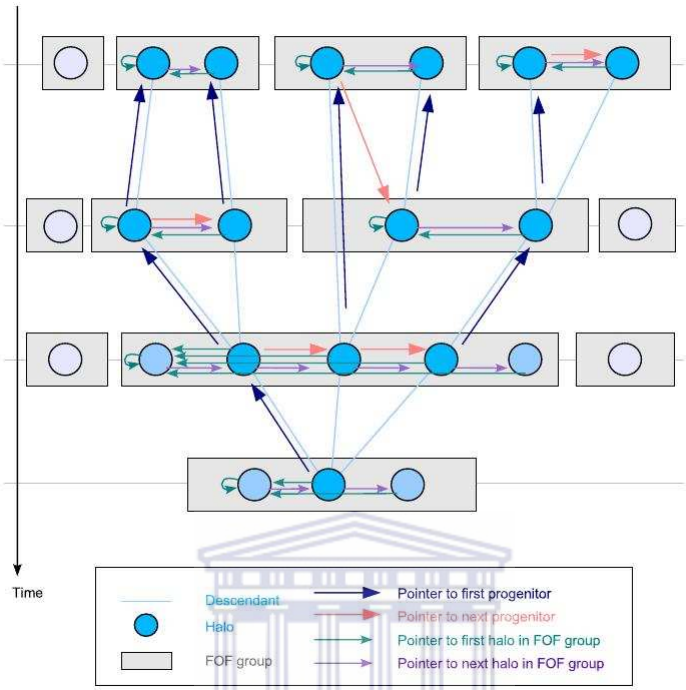

Figure 2.11: § [56] Schematic organisation of the merger tree in the Millennium Run. At each output time, FOF groups are identified which contain one or several (sub)halos. The merger tree connects these halos. The FOF groups play no direct role, except that the largest halo in a given FOF group is the one which may develop a cooling flow according to the physical model for galaxy formation implemented for the trees. To facilitate the latter, a number of pointers for each halo are defined. Each halo knows its descendant, and its most massive progenitor. Possible further progenitors can be retrieved by following the chain of next progenitors. In a similar fashion, all halos in a given FOF group are linked together.

The simulated mass distribution of the universe, just liked the observed universe, has a complex topology usually described as a "cosmic web". Pictures and the video of the output can be accessed from $http://www.mpa-garching.mpg.de/galform/millennium/$. The simulation is able to resolve hundreds of dark matter substructures (subhaloes) independently as gravitationally bound objects orbiting within the cluster halo. The plot of space density of dark matter haloes (FOF groups) produced by the simulation at various redshifts, gives a mass-range of dark matter haloes, from small groups of galaxies to the most massive clusters. This is shown in figure 2.13

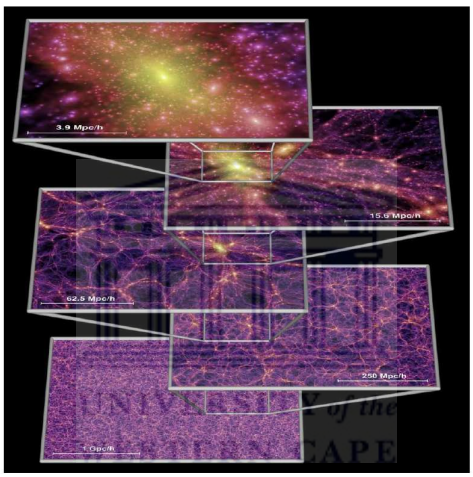

Figure 2.12: § [56] The dark matter density field on various scales. Each individual image shows the projected dark matter density field in a slab of thickness $15h^1$ Mpc (sliced from the periodic simulation volume at an angle chosen to avoid replicating structures in the lower two images), colour-coded by density and local dark matter velocity dispersion. The zoom sequence displays consecutive enlargements by factors of four, centred on one of the many galaxy cluster halos present in the simulation.

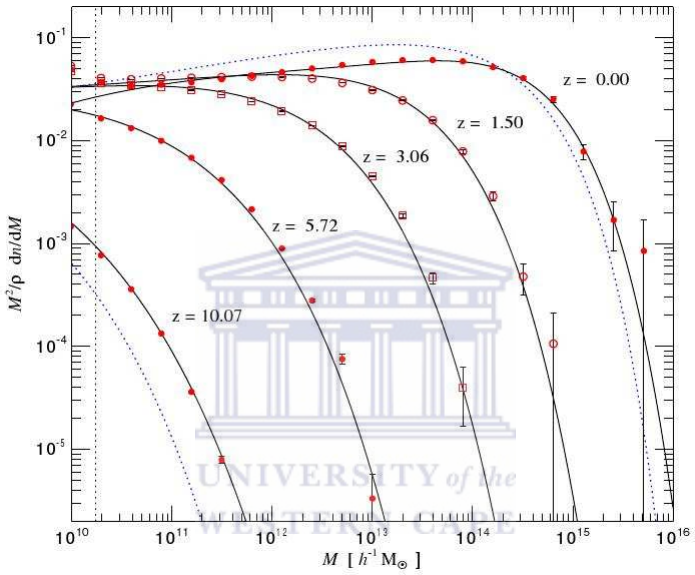

Figure 2.13: § [56] Differential halo number density as a function of mass and epoch. The function $n(M, z)$ gives the comoving number density of halos less massive than M. It is plotted as the halo multiplicity function $M^2\rho^{-1}dn/dM$, where ρ is the mean density of the universe. The fraction of mass bound to halos of more than 20 particles (vertical dotted line) grows from 6.42×10^4 at $z = 10.07$ to 0.496 at $z = 0$. Solid lines are predictions from an analytic fitting function proposed by Jenkins (2001), while the dashed lines give the Press-Schechter model [48] at $z = 10.07$ and $z = 0$.

2.7.2 Semi-Analytic models (SAM)

Semi-analytic models of galaxy formation are then implemented on the merger history trees of dark matter haloes plus their substructures. The semianalytic modelling simply involves grafting on the dark matter haloes the behaviour of baryons (gas); it tracks the physics of cooling, heating, star formation and evolution, galaxy dynamics, growth of black holes. The whole procedure includes carrying out analytical prescriptions with numerous adjustable parameters which are varied to match the observable properties of the universe, like the galaxy luminosity function, spatial distribution of large scale structure, X-ray luminosities of clusters, gas content and central black hole mass. The output of the millennium simulation (before grafting the semi-analytic models) contains a total of about 800 million nodes, each corresponding to a dark matter subhalo on which the associated galaxies are imprinted on. Imprinting the semi-analytic models on high resolution simulations of dark matter opposed to the traditional way of using Monte-Carlo realisation of merger trees is advantageous in that it reduces the uncertainties since the evolution of dark matter substructures are tracked accurately; providing accurate positions and peculiar velocities of all the model galaxies.

In this project, we used galaxy catalogues from the millennium simulation obtained by employing the semi-analytic modelling of the group at MPA (Max-Planck Institute for Astrophysics). The details can be found in Croton D. J. et al (2005). I give a summary of steps involved below.

Gas infall and cooling

The first step is tracking the gas infall and cooling. The mass fraction in baryons associated with every dark matter halo is set to be 17%, consistent with first year WMAP results by Spergel et al (2003). The gas initially has the same spatial distribution as dark matter (DM), fluctuations in DM haloes makes them collapse. Gas gets heated by shocks as it falls into DM gravitational potentials leading to production of hot gas haloes supported by pressure against collapse. In massive haloes, the gas shocks to a virial temperature (which depends upon the mass of the halo) and is added to a quasi-static hot

atmosphere extending approximately to the virial radius of the halo.

$$T_{vir} = \frac{1}{2}\frac{\mu m_H}{k} V_H^2 \tag{2.38}$$

$$V_H = \sqrt{\frac{GM}{r_{vir}}} \tag{2.39}$$

In lower massive haloes and at early times, the infalling process is treated in such a way that the gas still shocks to the virial temperature but a quasi-static atmosphere is not formed, since the postshock cooling time is relatively short. Dark matter haloes are supported against further gravitational collapse by pressure from thermalised velocities of DM particles. Gas then starts to cool through processes such as bound-bound and bound-free emission, inverse Compton Scattering of the CMB photons by the electrons in the hot halo gas (important for very early universe), bremsstrahlung radiation as electrons are accelerated in an ionized plasma, etc. The cooling process is dependent on temperature, which determines ionisation state, chemical composition, and density-rate of collision between electrons and ions.

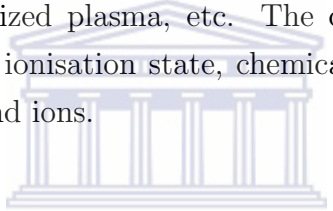

As gas cools, its pressure drops, it sinks to the centre on dynamical time scales in the halo. If the angular momentum is conserved, gas forms a rotationally supported disc. Infall rates of gas gives the cooling radius r_{cool}. The gas within the cooling radius has had sufficient time to cool since the formation of the DM halo. r_{cool} continues to propagate outwards until either all of the hot gas halo has cooled, or a merger with another halo results in the formation of a new halo [3]. The cooling time of the gas is defined as ratio of its specific thermal energy to the cooling rate per unit volume that is

$$t_{cool} = \frac{3}{2}\frac{\bar{\mu} m_p k T}{\rho_g(r)\Lambda(T, Z)} \tag{2.40}$$

where $\bar{\mu} m_p$ is the mean particle mass, k is the Boltzmann constant, $\rho_g(r)$ is the hot gas density, and $\Lambda(R, Z)$ is the cooling function which depends on both metallicity Z and temperature of the gas. The post-shock temperature of the infalling gas is assumed to be the virial temperature of the gas defined as, $T = 35.9(V_{vir}/kms^{-1})^2$K.

By defining the cooling radius, we can estimate the instantaneous cooling rate onto the central object of a halo. Different authors adopt different definitions, but the one used

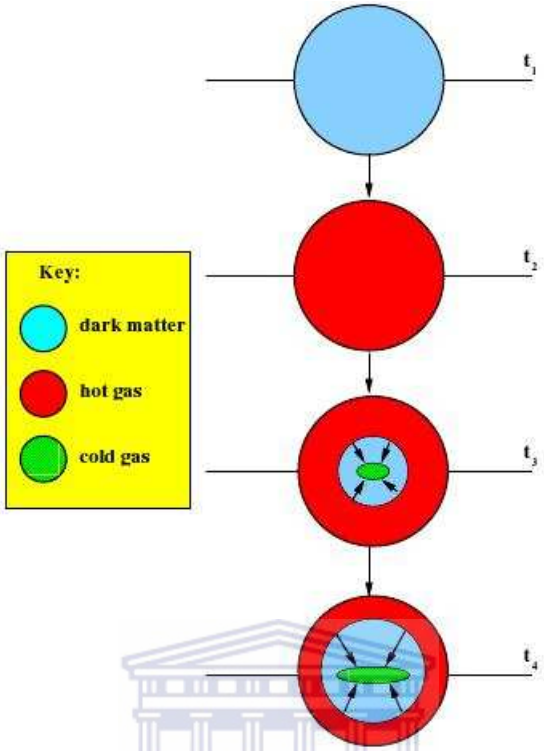

Figure 2.14: §[3] A schematic of the cooling model used in semi-analytical models represents a stage in the cooling process. In the first step (t_1), baryons fall into the gravitational potential well of the dark matter halo. This gas is assumed to be heated by shocks as it falls into the potential well, attaining the virial temperature associated with the halo (t_2). In the third step (t_3), the inner parts of the hot gas halo cool, forming a rotationally supported disc. At a later stage (t_4), the radius within which gas has had time to cool advances outwards towards the virial radius of the halo and the cold gas disc grows in size

here is adopted from Springel et al. (2001a) and De Lucia et al. (2004). They defined it as the point where the local cooling time is equal to the halo dynamical time, $R_{vir}/V_{vir} = 0.1H(z)^{-1}$. The cooling rate can then be computed through,

$$\dot{m}_{cool} = 4\pi\rho_g(r_{cool})r_{cool}^2\dot{r}_{cool} \tag{2.41}$$

where $\rho_g(r)$ is the hot gas density. The equation above is valid when $r_{cool} < R_{vir}$, and in this case the system forms a static hot gas halo (atmosphere) and cooling gas falls into the central object through *cold accretion*. A system is said to form a static halo when the mass of hot halo gas exceeds that of cold disk gas. The alternative is *rapid accretion*, when $r_{cool} > R_{vir}$, that is at early epochs and in lower mass halos where the post-shock

gas cools in less than one sound crossing time and cannot maintain the pressure needed to support an accretion shock at large radius.

Cooling can be reduced especially in massive halos by physical processes such as supernova explosions (heating the gas causing it to be more diffuse), thermal conduction from outer parts of the hot gas halo to the inner parts, and accretion of material onto a central black hole.

Effect of Reionization

The effect of reionization was computed based on a technique by Gnedin (2000) where he showed that the effect of photoionization heating on the gas content of a halo of mass M_{vir} can be modeled by defining a characteristic mass scale, *the filtering mass*, M_F, below which the gas fraction f_b is reduced relative to the universal value expressed as,

$$f_b^{halo}(z, M_{vir}) = \frac{f_b^{cosmic}}{(1 + 0.26 M_F(z)/M_{vir})^3} \tag{2.42}$$

M_F is a function of redshift and is noted to change significantly around the epoch of reionization. Details can be found in Gnedin [26], and the full description as well as the derivation of the analytical model can be found in Kravtsov et al [39].

Black Hole growth and AGN outflows

The third task was implementation of black hole (BH) growth and AGN outflows. The major role of black holes and AGN processes is suppression of cooling flows, hence modifying the luminosities, colours, stellar masses and clustering of the galaxies that populate the bright end of the luminosity function. Two modes of BH growth are considered depending on whether mass accretion is due to a major merger or a result of hot gas accretion.

The quasar mode results from major mergers (a major merger occurs when two galaxies of comparable mass merge, otherwise it is a minor merger), where the gas accreted during a merger is assumed to be proportional to the total cold gas present, but with the efficiency lower for smaller mass systems and for unequal mergers, that is

$$\Delta m_{BH,Q} = \frac{f'_{BH} m_{cold}}{1 + (280 kms^{-1}/V_{vir})^2} \tag{2.43}$$

where

$$f'_{BH} = f_{BH}(m_{sat}/m_{central}) \tag{2.44}$$

$f_{BH} \approx 0.03$ is constant and is chosen to reproduce the observed local $m_{BH} - m_{bulge}$ relation, m_{cold} is the mass of the cold gas, m_{sat} is the mass of the satellite halo and $m_{central}$ is the mass of the central halo. More details can be found in references [11][34].

The radio mode results from hot gas accretion onto a central supermassive black hole. It occurs when a static hot halo has formed around the black hole's host galaxy, and produces lower energy compared to the quasar mode, but sufficient enough to reduce or even stop the cooling flow. The accretion is assumed to be continual and quiescent and defined by the black hole mass accretion rate density as,

$$\dot{m}_{BH,R} = \kappa_{AGN} \left(\frac{m_{BH}}{10^8 M_\odot}\right) \left(\frac{f_{hot}}{0.1}\right) \left(\frac{V_{vir}}{200 kms^{-1}}\right)^3 \tag{2.45}$$

where m_{BH} is the black hole mass, f_{hot} is the fraction of the total halo mass in form of hot gas, $V_{vir} \propto T_{vir}^{1/2}$ is the virial velocity of the halo, and κ_{AGN} is a free parameter in units of $M_\odot yr^{-1}$ with which the efficiency of accretion is controlled, the value used is $\kappa_{AGN} = 6 \times 10^{-6} M_\odot yr^{-1}$.
The effect of quasar mode accretion as noted earlier is dominant over radio mode in suppressing cooling flows, but the radio mode becomes important at later times and for large values of black hole mass.

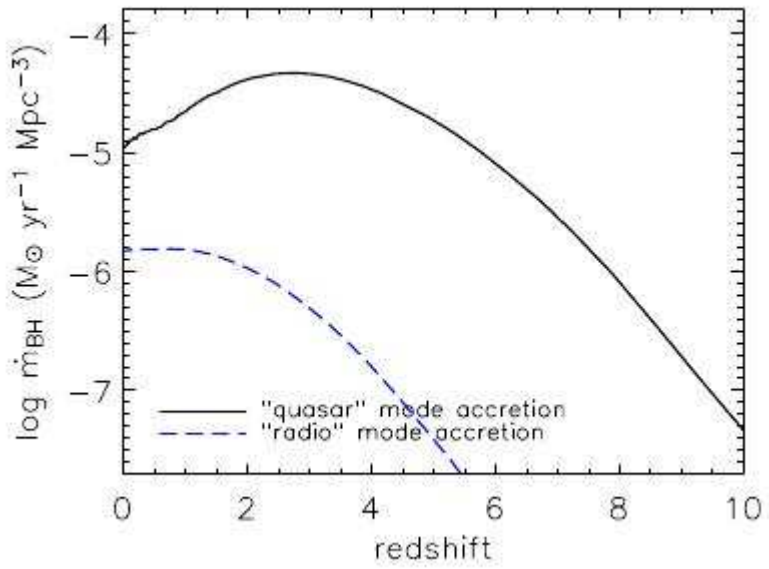

Figure 2.15: § [11]The black hole accretion rate density, $\dot{m}_{BH}$, as a function of redshift for both the 'quasar' and the 'radio' modes discussed above. This figure shows that the growth of black holes is dominated by the 'quasar mode' at high redshift and falls off sharply at $z \lesssim 2$. In contrast, the 'radio mode' becomes important at low redshifts where it suppresses cooling flows, but is not a significant contributor to the overall black hole mass budget

Star formation

The other process taken into account in the simulation is that of star formation. An assumption is made that all star formation occurs in a cold disk gas, either quiescently or in a star burst (star bursts are associated with mergers, which can cause change in the morphology of the two systems merging and 'quasar mode' accretion). Based on observational work of Kennicutt [35], a threshold surface density adopted for the cold gas is that of a kind below which no stars form, but above which gas starts to collapse and form stars. The critical surface density at a distance R from the galaxy centre is approximated by [33],

$$\Sigma_{crit}(R) = 120 \left(\frac{V_{vir}}{200 kms^{-1}} \right) \left(\frac{R}{kpc} \right)^{-1} M_\odot pc^{-2} \tag{2.46}$$

This is converted to critical mass by assuming the cold gas mass to be evenly distributed over the disk, that is

$$m_{crit} = 3.8 \times 10^9 \left(\frac{V_{vir}}{200kms^{-1}}\right)\left(\frac{r_{disk}}{10kpc}\right) M_\odot \tag{2.47}$$

and for the scale length $r_s = \left(\lambda/\sqrt{2}\right) R_{vir}$, the outer disk radius is set $r_{disk} = 3r_s$ based on the properties of the Milky Way. The disk radius is explained in detail by Mo et al [45], where λ is the spin parameter defined in terms of angular momentum of the halo, J as $\lambda = J|E|^{1/2}G^1M^{5/2}$, E being the total energy of the halo [45]. If the mass of the cold gas in a galaxy is greater than the critical value defined above, then the star formation rate is assumed to be

$$\dot{m}_\star = \alpha_{SF}(m_{cold} - m_{crit})/t_{dyn,disk} \tag{2.48}$$

where the efficiency α_{SF} is set so that 5 to 15 percent of the gas is converted to stars in a disk dynamical time $t_{dyn,disk}$, defined as r_{disk}/V_{vir}.

Supernova feedback

Supernova feedback was modeled following the observations by Martin (1999), that is the amount of cold gas reheated by supernova is given by

$$\Delta m_{reheated} = \epsilon_{disk}\Delta m_\star \tag{2.49}$$

where $\Delta m_\star$ is the mass of stars formed over some finite time interval, and ϵ_{disk} is a parameter which was fixed at $\epsilon_{disk} = 3.5$ based on observational data. The amount of energy released in this interval is then approximated by

$$\Delta E_{SN} = 0.5\epsilon_{halo}\Delta m_\star V_{SN}^2 \tag{2.50}$$

where $0.5V_{SN}^2$ is the mean energy in supernova ejected per unit mass of stars formed, and ϵ_{halo} defines the efficiency with which the energy is able to reheat disk gas. $V_{SN} = 630kms^{-1}$ was adopted basing on the standard initial stellar mass function (IMF) and standard supernova theory, and ϵ_{halo} was taken to be $\epsilon_{halo} = 0.35$ to fit the observations

as mentioned earlier.

Assuming that the reheated gas was added to the hot halo without changing its specific energy, then its total thermal energy would change by

$$\Delta E_{hot} = 0.5\Delta m_{reheated} V_{vir}^2 \tag{2.51}$$

such that the excess energy in the hot halo after reheating becomes $\Delta E_{excess} = \Delta E_{SN} - \Delta E_{hot}$. For $\Delta E_{excess} < 0$, the energy transfered with the reheated gas is insufficient to eject any gas out of the halo and the assumption that all the hot gas is not dissociated from the main halo is made. For $\Delta E_{excess} > 0$, there is excess energy to eject the hot gas from the halo to an external 'reservoir', which is estimated as

$$\Delta m_{ejected} = \frac{\Delta E_{excess}}{E_{hot}} m_{hot} = \left(\epsilon_{halo} \frac{V_{SN}^2}{V_{vir}^2} - \epsilon_{disk} \right) \Delta m_\star \tag{2.52}$$

where $E_{hot} = 0.5 m_{hot} V_{vir}^2$ is the total thermal energy of the hot gas, and $\Delta m_{ejected}$ is set at $\Delta m_{ejected} = 0$ when $\Delta E_{excess} < 0$. The process is modeled in such a way that for small V_{vir} the entire hot halo can be ejected, and the ejected gas need not be lost permanently; as the dark halo grows, some of the surrounding ejecta may fall back in and get reincorporated into the cooling cycle. The reincorporation is modeled based on Springel et al [55] and Delucia et al [16] , that is by assuming

$$\dot{m}_{ejected} = -\gamma_{ej} m_{ejected} / t_{dyn} \tag{2.53}$$

where γ_{ej} is set to control the amount of reincorporation per dynamical time, and it typically ranges from 0.3 to 1.0. These values imply that all the ejected gas will return to the hot halo in a few halo dynamical times.

The other processes modeled in the simulation include the galaxy morphology, merging and starbursts; which explains how galaxy mergers influence their morphology and star bursts. It accounts for the difference between major and minor mergers where for a minor merger, the stars of the satellite galaxy are added to the bulge of the central galaxy and the cold gas of the satellite is added to the disk of the central galaxy with any stars that formed during the star burst. For a major merger, the disks of both galaxies are destroyed

to form a spheroid in which all stars are placed. Lastly, the spectroscopic evolution and star dust was modeled following Bruzual & Charlot [7], and metal enrichment was adopted from De Lucia et al [16].

Chapter 3

Methodology

3.1 Introduction

This chapter gives the criteria we used to select galaxy clusters from the millennium simulation database, the calibrations used to convert from star formation rate (a parameter given in the simulation) to the IR luminosity, and the spectral energy distribution models used. I also describe how temperature fluctuations are obtained from the fluxes derived for the IR galaxies in clusters.

3.2 Data

The output of the millennium simulation and superposed semi-analytic models is stored in a relational database, where the individual properties of galaxies and dark matter halos are stored in columns in the database table. The data is accessible online using the standard Structured Query Language (SQL). The web interface allows users to formulate scientific questions as SQL queries operating on the tables, in which rows correspond to individual objects (halos and/or galaxies) always identified with their halo or galaxy IDs and columns contain attributes of these objects (positions, velocity, mass, angular momentum, size, flattening, type, colour, luminosity, indices, star formation rate, etc)

[24]. Our parameters of interest are position (x,y,z coordinates) of the galaxy, its star formation rate and mass as well as the virial mass of the background halo (corresponding to the virial mass of a cluster).

The SZE surveys aim to identify all clusters in a specific angular region of the sky, $\delta\Omega$, then find their redshifts, and masses. For flux limited surveys, the identification will be for clusters above a certain mass limit. In this project, we prioritise estimation of the contribution of faint infrared sources within the cluster to the SZE signal. Variations in the contributions can be considered for a given mass-limit and redshift range.
Now, if N is the number of clusters observed in a given redshift and mass bin, dz and dM respectively, then in a flux limited survey, one can measure the number of clusters for a comoving volume element $dV/dzd\Omega$ for a solid angle $d\Omega$ on sky, given by.

$$\frac{dN}{dzd\Omega} = \frac{dV}{dzd\Omega}(z)\int_{M_{min}} dM\frac{dn}{dM}(M,z) \tag{3.1}$$

where $\frac{dn}{dM}$ is the number density of clusters between M and $M + dM$ at z.

In the simulation, each snapshot (snapnum) corresponds to a redshift, z. This means that we can compute the number density of clusters in a mass bin dM, $\frac{dn}{dM}$, or n, the number density of clusters above a certain mass limit, M_{min}, for different snapshots, where M_{min} is the minimum cluster mass that can be detected in the the SZE survey. We used $M_{min} = 2 \times 10^{14} M_{\odot}$, which is approximately the detection limit for the Atacama Cosmology Telescope (ACT) [37]. We therefore extracted all clusters in the millennium database with virial mass $M_{min} = 2 \times 10^{14} M_{\odot}$.

3.3 Fluxes

Infrared fluxes from starforming galaxies are obtained from the star formation rates using the Kennicutt calibration [35]. Kennicutt gives a relation between the star formation rate (SFR) and the far-infrared luminosity for starburst galaxies. The relation holds for galaxies ranging from low-level starbursts ($L_{FIR} \sim 10^8 - 10^{10} L_{\odot}$) to ultraluminous starburst

($L_{FIR} > 10^{12} L_{\odot}$) galaxies, where L_{FIR} is the far-infrared ($\lambda = 40 - 500\mu m$) luminosity. The relation is given by the formula below.

$$\frac{SFR}{1 M_{\odot} yr^{-1}} = \frac{L_{FIR}}{2.2 \times 10^{43} erg.s^{-1}} = \frac{L_{FIR}}{5.7 \times 10^{9} L_{\odot}} \tag{3.2}$$

From equation 3.2, low-level starbursts will have a star formation rate of about $0.2 M_{\odot} yr^{-1}$. An alternative relation is

$$\frac{SFR}{1 M_{\odot} yr^{-1}} = 1.8 \times 10^{-10} \frac{L_{IR}}{L_{\odot}} \tag{3.3}$$

where L_{IR} is the bolometric infrared luminosity (between $8 - 1000\mu m$). L_{FIR} can be obtained from L_{IR} using relations given by Chary and Elbaz (2001).
After some experimentation, we set the minimum SFR which we consider to be $sfr \geq 0.2 M_{\odot} yr^{-1}$ (below this value there is a negligible contribution to the total flux in a cluster). We then extracted all galaxies within a cluster (above the mass limit described above), which satisfy the star formation rate conditions.

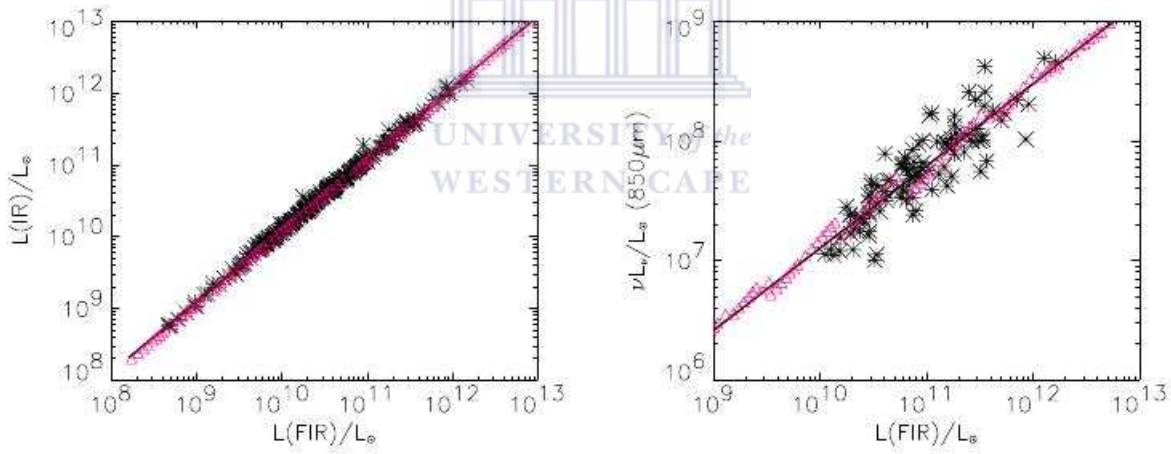

Figure 3.1: § [9] The asterisks show data from IRAS, ISOCAM and SCUBA surveys. The lines are the best fit of a first order polynomial. The red triangles are the corresponding values from template spectral energy distributions of Chary & Elbaz [9].

We use equation 3.3 to obtain the bolometric infrared luminosity, L_{IR}. After which we use the Chary and Elbaz (2001) model to compute the far-infrared luminosity for each selected galaxy as in figure 3.1,

$$1og_{10}(L_{IR}) = 0.9981og_{10}(L_{FIR}) + 0.0847 \tag{3.4}$$

where L_{FIR} here is defined in the wavelength range $(40 - 500\mu m)$ as defined before. Still using the spectral energy distribution from Chary and Elbaz (2001), we then obtained the monochromatic luminosity at 850μm ($350GHz$) using the relation

$$1og_{10}(L_{350GHz}) = 0.6731og_{10}(L_{FIR}) + 0.3738 \tag{3.5}$$

We then calculated the corresponding fluxes at $350GHz$ from the flux luminosity relation

$$S(\nu) = \frac{L(\nu)}{4\pi D_L^2} \tag{3.6}$$

where D_L is the luminosity distance, which is a function of redshift, z, using the cosmology of the millenium simulation. We finally obtain the monochromatic fluxes at the ACT frequencies (145, 217 and 265 GHz) using the scaling $S_\nu \propto \nu^\alpha$. To understand how this scaling comes about, I briefly review information on the spectral energy distribution (SED) of infrared galaxies.

The observed spectral energy distribution of infrared galaxies depends on the properties of the dust models and stellar populations. The dust models vary according to the composition and size distribution of dust particles one adopts. Generally speaking, the SED is modeled as a sum of stellar emission, PAH emission, power-law emission, and thermal grey-body emission [50]. The stellar emission is mainly from the old population, which is accounted for by considering a 10 Gyr-old single stellar population, with a solar metallicity and Salpeter Initial Mass Function (IMF). The model used for PAH is typical of that constructed by Draine et al (2003), where he considers PAH molecules to be silicate minerals, with emission and absorption lines between $1 - 24\mu m$. A detailed explanation of this model can be found in [18]. The PAH emission therefore dominates the mid-infrared wavelength. For continuum dust emission, the two models mainly used are; a power-law of the form, $f_\nu \propto \nu^{-\alpha_d}$ to represent emission from warm, small grains (that is for roughly $\lambda < 60\mu m$), where α_d is the emission index, with typical values ~ 3. In the Sajina, Scott, Dennefeld, Dole and Lacey (2004) model, this part of the spectrum is cut-off as $exp(-0.17 \times 10^{14} Hz/\nu)$ in order not to interfere with the IR/sub-mm wavelength emission, described by a thermal component $f_\nu \propto \nu^{3+\beta}[exp(h\nu/kT) - 1]^{-1}$. The SED would

then be of the form in figure 3.2.

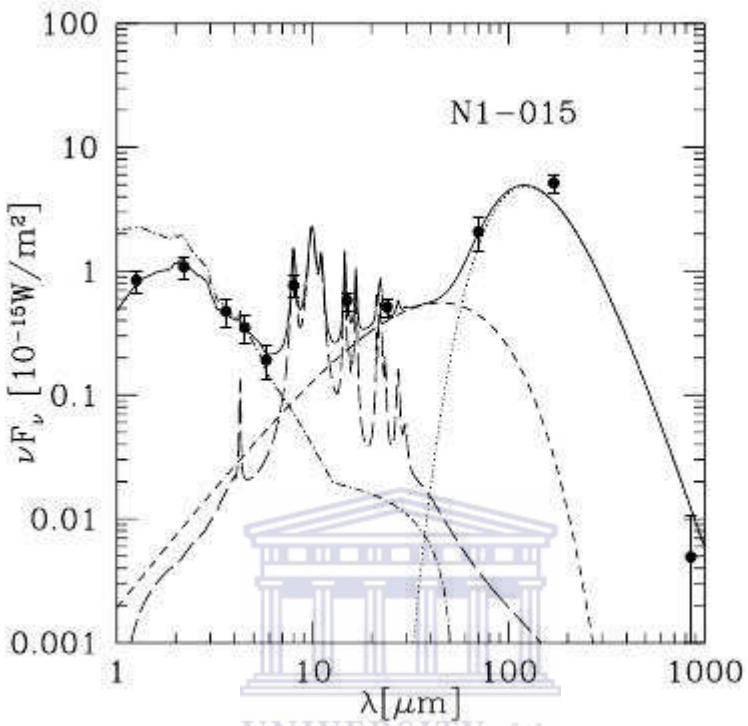

Figure 3.2: § [50] The spectral energy distribution of infrared bright galaxy. It includes a grey-body (dotted line), a warm power-law (short-dash), PAH emission (long-dash), and unextincted stellar emission (dot-dash) with $e^{-\tau\nu}$ extinction applied. The thick solid line is the total

Using the thermal component of the SED (for far-infrared and sub-mm), we can summarise it as $S_\nu \propto \nu^{\beta_{mm}} B_\nu$ (where β_{mm} refers to the emissivity index), or simply a power-law of the form $S_\nu \propto \nu^\alpha$ as explained above, for sub-mm/mm wavelength ($< 350GHz$). For the range 150 - 350 GHz, Knox, Holder & Church (2004) used best-fit spectra for local galaxies, and by placing them at a range of redshifts, they found the best fit to the power-law with the spectral index well fitted by $\alpha = 3.14 - 0.22z$, with a fairly constant scatter at each redshift of $\sigma_\alpha \sim 0.18$. By assuming a uniform distribution in redshift between 0 and 5, they found a mean spectral index of 2.6. More literature on this can be obtained from Dunne et al [19]. In general, the average value of $\alpha \sim 2.5$. We therefore used this model to compute the monochromatic fluxes (at 145, 217 and 265 GHz) from the 350 GHz fluxes derived above.

3.4 Temperature fluctuations

We computed the temperature fluctuations for the kinetic SZE using equation 2.25. The details of this equation can be found in section 2.33

$$\Delta T_{RJ} = -\beta \tau_e T_{rad} \frac{x^2 e^x}{(e^x - 1)^2} \tag{3.7}$$

Chapter 4

Results and Discussion

4.1 Overview

In this chapter I present results and a discussion of the results. I show that our models generate source counts which are consistent with a number of observations. I present 2D projections of galaxy clusters, highlighting the positions of starforming galaxies, and show plots of galaxy number counts as a function of radius. The next section displays tables (chosen at selected redshifts) showing the fluxes and temperature fluctuations, ΔT at 3 observation frequencies of ACT (i.e 145 GHz, 217 GHz, 265 GHz) deduced from infrared bright galaxies within clusters. A summary of the displayed tables plus other results of fluxes and ΔT at different redshifts (tables not displayed) is shown in a plot of ΔT against z. We then provide a fitting functions of ΔT as a function of z, and compute the estimated contamination of SZ signals from clusters.

4.2 Simulation output versus observations

We test the output of our models used in the millennium simulation (as described in section 2.7.2) against observations summarized in Huynh et al (2007).

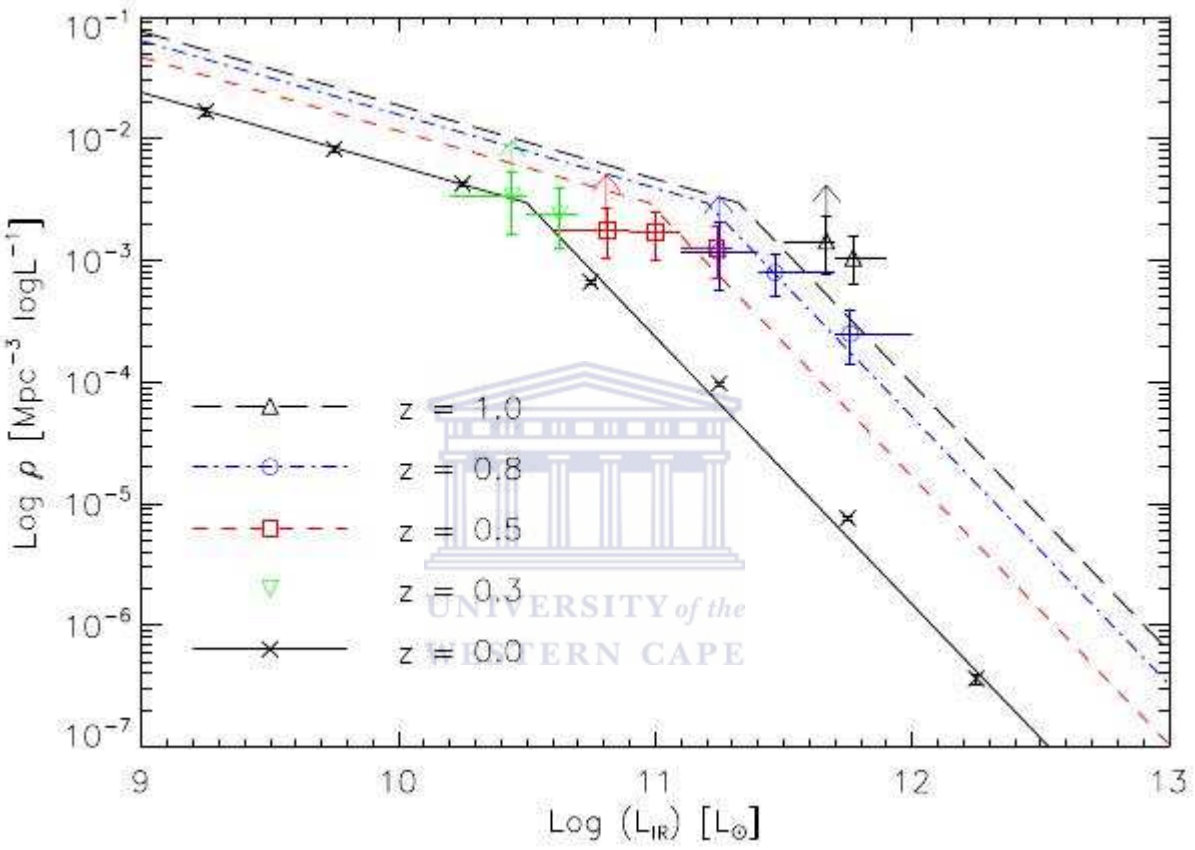

Figure 4.1: IR luminosity function (LF) observations adapted from [29], in which crosses mark the local LF from Sanders et al. (2003) and the corresponding solid line is the double power law fit to the local data. The symbols mark the LF calculated in their work at redshift 0.3 (upside down triangles), 0.5 (squares), 0.8 (circles) and 1.0 (triangles). The lines are the local LF evolved to the corresponding redshift with the best fit pure evolution parameters. The arrows indicate bins which are incomplete because of the survey sensitivity. The horizontal error bars indicate the binsize

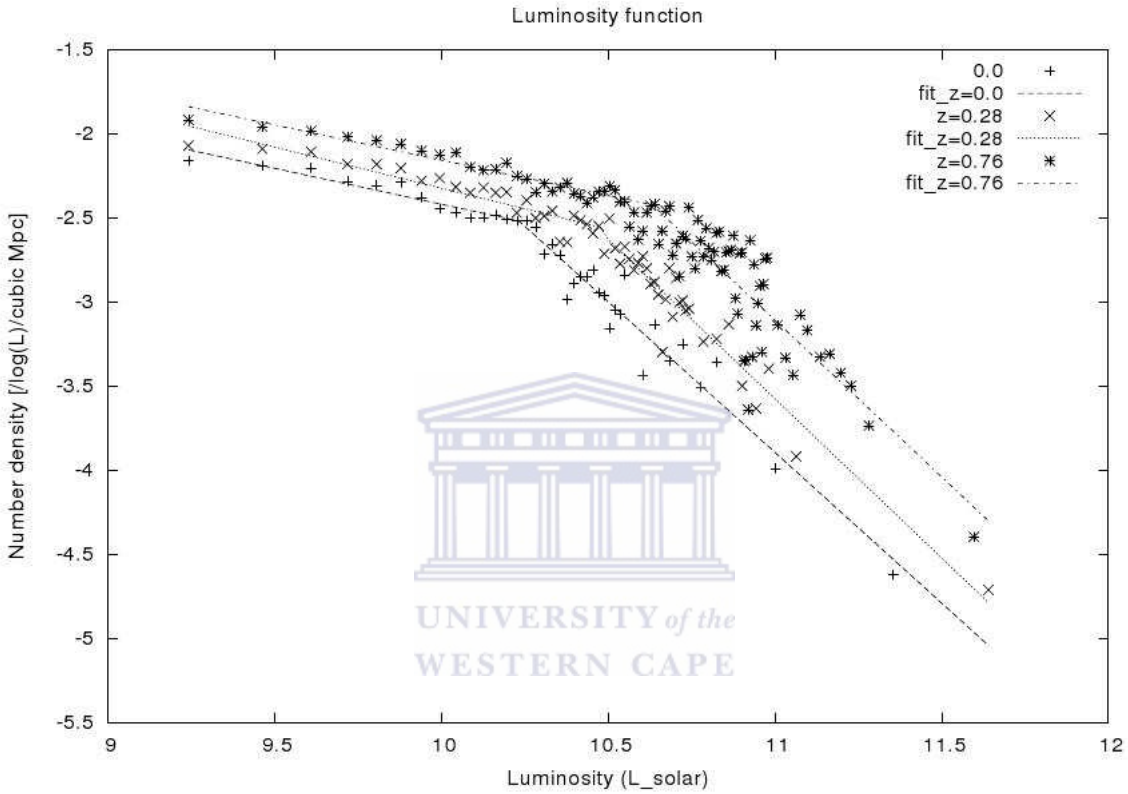

Figure 4.2: The IR luminosity function, obtained using our model in the millennium simulation at different redshifts. The three lines (dash, dotted, and dash-dotted) are corresponding fits for the redshifts $z = 0$, 0.28 and 0.76. The break points indicate a seperation between the two classes of infrared galaxies, the Luminous InfraRed Galaxies (LIRGs) and the Ultra-Luminous InfraRed Galaxies (ULIRGs). The low density of ULIRGs can thus be effectively seen as a sharp slope in the luminosity function. What is also recognisable is the difference in the evolution rate of the number density of the two classes, it is relativey high for ULIRGs, an indication of their abundance at higher redshifts. It is also vital to note that this is a log - log plot

Figure 4.1 shows local observations of the luminosity function (LF) and constraints on the evolution of the LF from other data. The evolution of the luminosity function can be described as $\rho(L, z) = g(z)\rho[L/f(z), 0]$, where $g(z)$ and $f(z)$ represent the evolution of the density and luminosity of the luminosity function, usually represented as $g(z) = (1 + z)^q$ and $f(z) = (1 + z)^p$. In the observational data plot, the data points are observations and the dotted lines are the local LF evolved to the corresponding redshift with the best fit pure evolution parameters [29]. Observations indicate that the evolution is not strong in luminous infrared galaxies (LIRG) for $z < 0.4$ and the evolution is generally strong for ultraluminous infrared galaxies (ULIRGs) and even stronger at higher redshifts.

In Figure 4.2, we plot results from our simulation. The number density of IR sources above a limiting luminosity of $L = 1.78 \times 10^9 \mathrm{L}_\odot$ is given as a function of luminosity for various redshifts. The shape and evolution of the LF is similar to what is observed in the observations. The profile is a double power law with a sharper slope at the luminous end of the luminosity function than at the faint end. The local luminosity function has a break point at $L \approx 2 \times 10^{10} \mathrm{L}_\odot$ for the simulation data and $L \approx 3 \times 10^{10} \mathrm{L}_\odot$ for the observational data. For the millennium simulation data LF, the lines are best fits to the points.

Despite the similar shapes of the LF for both the simulation and the observation; similar in that they both predict a double power-law of log- log plot of LF, we note that the millennium simulation data underpredicts the number density slightly. The possible explanations for this are:

- We used the milli-millennium simulation to construct this LF. The milli-millennium simulation has a volume of 1/512 that of the full simulation. It is possible that the low number density is partly due to the small sample volume. Similarly the simulation LF does not show galaxies with $L > 4.5 \times 10^{11} \mathrm{L}_\odot$ because the number density of ULIRGs is low and the sample volume of the milimillennium simulation is not large enough to pick out galaxies which are that bright.
- The other possibilty could be as explained by E. Daddi et al (2007), who in his study of star formation and galaxy growth suggested that star formation in massive galaxies (ULIRGs) occurs too early in the simulation, or was terminated too early due to the adopted truncation of star formation rate from AGN feedback.

In summary, there exists an approximate match between the output of the simulation and the observation. The model is adequate for achieving our goal of studying the contamination of SZE in clusters by the IR galaxies within the clusters, and other properties of galaxy clusters as detailed in the next sections. It is adequate since the number density we obtain from the simulation is relatively comparable to that from the observations, and the contamination effect of these sources (infra red galaxies) on the SZ surveys can thus be approximated using the simulation output.

4.3 The distribution of simulated star forming galaxies in clusters

4.3.1 2D projections

It is important to know the location within the cluster, of the star-forming galaxies (contributing to sub-mm fluxes) as compared to the SZ signatures: if, for example, star formation was enhanced in the outer parts of clusters, the resulting annulus of excess IR-contributions may cause problems for SZE filtering techniques. Studies have shown that less massive cold clusters are more prolific star forming environments than massive hot clusters, but there is also an observed variation within a cluster irrespective of the mass. This variation is seen to be dependent on cluster environment [41]. The X-ray surface brightness profile drops from the centre toward the outskirts; we therefore expect the SZ signal to be strongest at the cluster core and relatively less at the outskirts. We plot the distribution of galaxies in clusters to identify the location of active star forming galaxies; this can be compared with the expected distribution of SZ flux.

Examples of the distribution of starforming galaxies in clusters at z=0.36 are shown in Figure 4.3. The less massive cluster ($2.2 \times 10^{14} M_{\odot}$) contains few galaxies with star formation rate sfr$> 3 M_{\odot} yr^{-1}$; the intermediate size cluster ($7.5 \times 10^{14} M_{\odot}$) contains more and the most massive cluster contains the most, even though star formation is quenched in many galaxies that fall into clusters. In the next section, we determine what fraction of galaxies in a cluster are star forming as a function of mass.

In figure 4.4, we plot distributions for simulated clusters identified at higher redshifts. We observe that the number of galaxies with high star formation rates increases with redshift. In both figures 4.3 and 4.4 (and in the many other distributions we plotted), we observe that clusters are generally irregular shaped objects often showing signs of infalling galaxies. High star formation rates are sometimes associated with infalling galaxies.

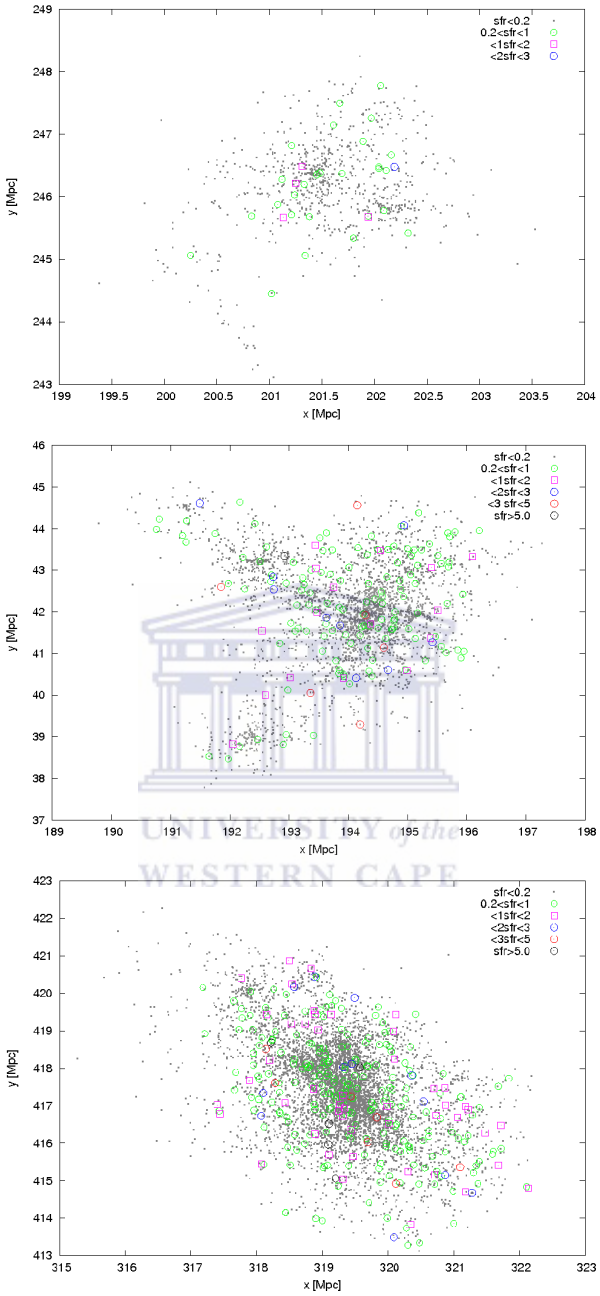

Figure 4.3: Examples of the distribution of galaxies in clusters at redshift, $z = 0.36$. The grey points are galaxies with star formation rate, sfr< 0.2 in $M_{\odot}yr^{-1}$ and the green circles are galaxies with $0.2 <$sfr< 1, and so on as indicated on the figure. The grey points are scaled smaller than the others for visual clarity. The three figures are for a less massive cluster ($2.2 \times 10^{14} M_{\odot}$), an intermediate mass cluster ($7.5 \times 10^{14} M_{\odot}$) and the most massive $2.21 \times 10^{15} M_{\odot}$ cluster projected on the x-y axes.

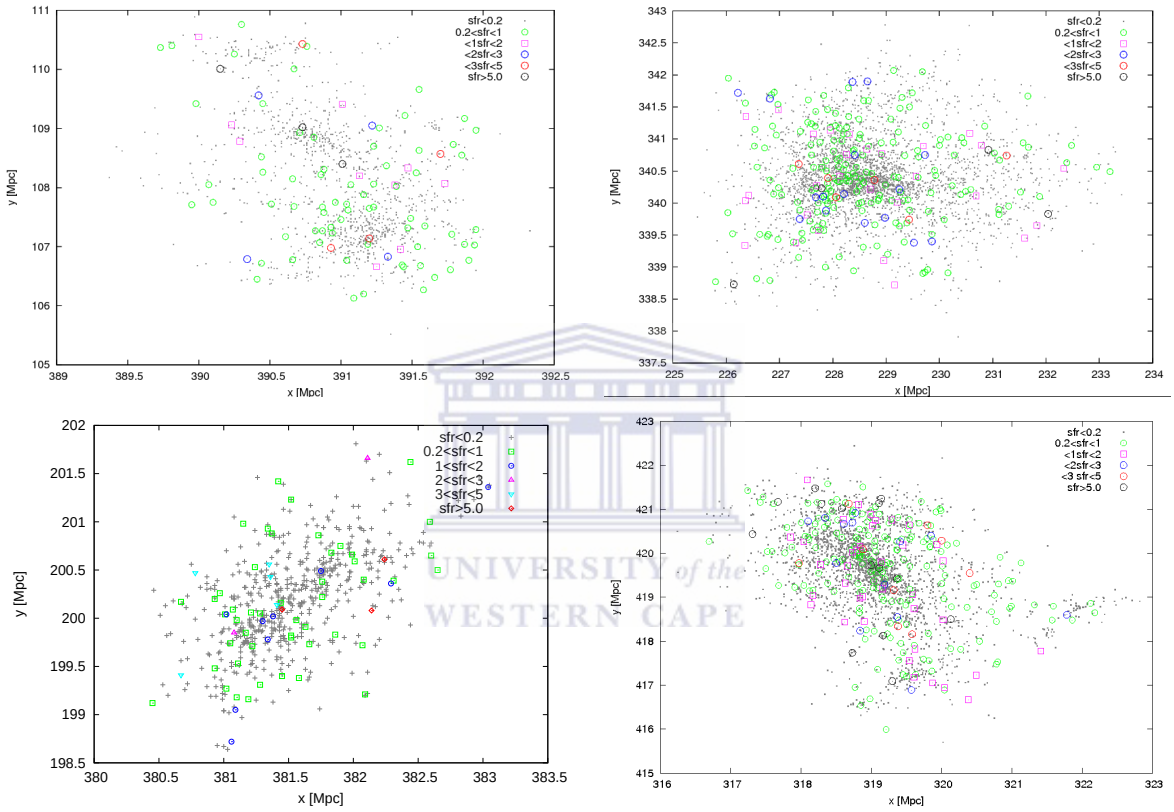

Figure 4.4: The upper row is two clusters at intermediate redshift, $z = 0.69$, a $2.2{\times}10^{14} M_{\odot}$ cluster (left) and a $1.16 \times 10^{15} M_{\odot}$ (right). The bottom row is two clusters at $z = 1.08$, a $2.1 \times 10^{14} M_{\odot}$ cluster (left) and $7.1 \times 10^{14} M_{\odot}$ (right). The projected distribution doesn't seem to vary with redshift significantly, but what is obvious is that the number of star forming galaxies tends to increase with redshift, depending on the richness of the cluster.

4.3.2 The radial distribution of galaxies in clusters and substructure

We observed in our plots that simulated clusters are not only irregular in shape but also as mentioned before, show regions of infalling halos containing many galaxies. Some of the infalling halos have active star forming galaxies when compared to other regions within the cluster. To make sure that this is not just a 2D projection effect, we plotted the radial distribution of the number density of starforming galaxies and all galaxies, n within the cluster both in two and three dimensions (2D and 3D). n is obtained by dividing the number of galaxies within a radius or 3D shells (3 dimensions) by the area and the volume of the shell (for 3D shells), for galaxies in clusters with $M_{clus} > 2.0 \times 10^{14}$ $M_{\odot}$. That is for 2 dimension,

$$n = \frac{N(sfr > 0.2, r_i \leq r \leq r_{i+dr})}{2\pi r_i dr} \tag{4.1}$$

for $i = 0.2, 0.4, 0.6, ...$, where $N(sfr > 0.2, r_i \leq r \leq r_{i+dr})$ is the number of galaxies with star formation rate greater than $0.2 M_{\odot} yr^{-1}$ within the area bounded by the circles of radius r_i and r_{i+dr}. $dr = 0.2$ is the interval of the bins in Mpc, sfr is in $M_{\odot} yr^{-1}$. At $i = 0$, n becomes

$$n = \frac{N(sfr > 0.2, r \leq dr)}{\pi dr^2} \tag{4.2}$$

In 3 dimensions

$$n = \frac{N(sfr > 0.2, r_i \leq r \leq r_{i+dr})}{4\pi r_i^2 dr} \tag{4.3}$$

with $N(sfr > 0.2, r_i \leq r \leq r_{i+dr})$ being the number of galaxies with star formation rate greater than $0.2 M_{\odot} yr^{-1}$ within the volume bounded by the spherical shells of radius r_i and r_{i+dr}. At $i = 0$ n becomes

$$n = \frac{N(sfr > 0.2, r \leq dr)}{\frac{4}{3}\pi dr^3} \tag{4.4}$$

We find in Figures 4.5 and 4.6 that the number density of galaxies with $sfr > 0.2 M_{\odot} yr^{-1}$ generally drops logarithmically but tends to have bumps in the outskirts for a few clusters. This increase is the effect of the halos residing outside the virial radius of the cluster with relatively high star formation rate. We identify these halos as substructures. Another

observation we make from the plots is that the 2 dimensional view of the clusters tends to concentrate the galaxies toward the center of the cluster. This is the effect of viewing both the foreground and background galaxies along the line of sight through the cluster. This observation is particularly worth noting when considering the contamination of the SZ signal since the SZ signal is highest at the cluster core.

Galaxy clusters are often modeled as virialised spherically symmetric systems, but even in the early 80's, studies showed that most galaxy clusters are composed of *substructures* sometimes called *subclusters*. Studies by Geller and Beers in (1982), showed that substructures are relevant to 30 - 60% of all clusters, after they had examined projected distributions of a sample of 65 Galaxy clusters. Kriessler and Beers (1997) examined 56 clusters and obtained a similar result. The sizes of these substructures are 0.4 - 0.6 Mpc [22] [23]. Escalera et al 1994 also studied the richness and masses. They found that the virial masses of substructures closely relate to the number of galaxies belonging to them, and that their typical masses are often 10% of the parent clusters total mass. Conselice and Gallagher (1998) and Kambas et al (2000) claim that they found some substructures as small as 0.2 Mpc. The substructures are attributed to the hierarchical scenario of large scale structure formation, in which smaller subclumps of matter merge to form large virialised systems. West and Bothun (1990) categorized substructures in galaxy clusters into four classes:

1. remnants of galaxy systems which have merged or are in a merging phase to form a rich cluster (usually associated with young clusters)
2. substructures presently residing within an otherwise relaxed cluster, arising from secondary infall of bound groups in the phase of tidal disruption within the cluster.
3. galaxy groups bound to the cluster but still outside the virial region,
4. galaxy groups which are dynamically disjoint from clusters

The millennium simulation uses the LCDM hierarchical model, so we would expect substructures. What is interesting is that by plotting 2D projectecd and 3D shell distributions we can identify clusters with substructures that appear to be detached from the parent

clusters with particularly large numbers of active star forming galaxies. This is evidenced in $5.7 \times 10^{14} M_{\odot}$ at $z = 0.36$ (the second row in Figures 4.5 and 4.6). We can confidently rule out attributing substructures to projection effects as was claimed by some authors, because they are clearly observable even in 3D shell distributions.

We find that most cluster cores are composed of passive star forming galaxies, as would be expected; we deduce this by examining the number density, n distribution of sfr > 0.2 $M_{\odot} yr^{-1}$ for 3D shells. In some cases the number of starforming galaxies is actually greater for 3D shells at the core than for 2D projections, as in the third row shown in figure 4.5. Such rare cases could appear if a cluster has undergone a merger. Lastly to note about Figures 4.5 and 4.6 is that the density profile of clusters tend to be very similar when the small effects of substructures are removed.

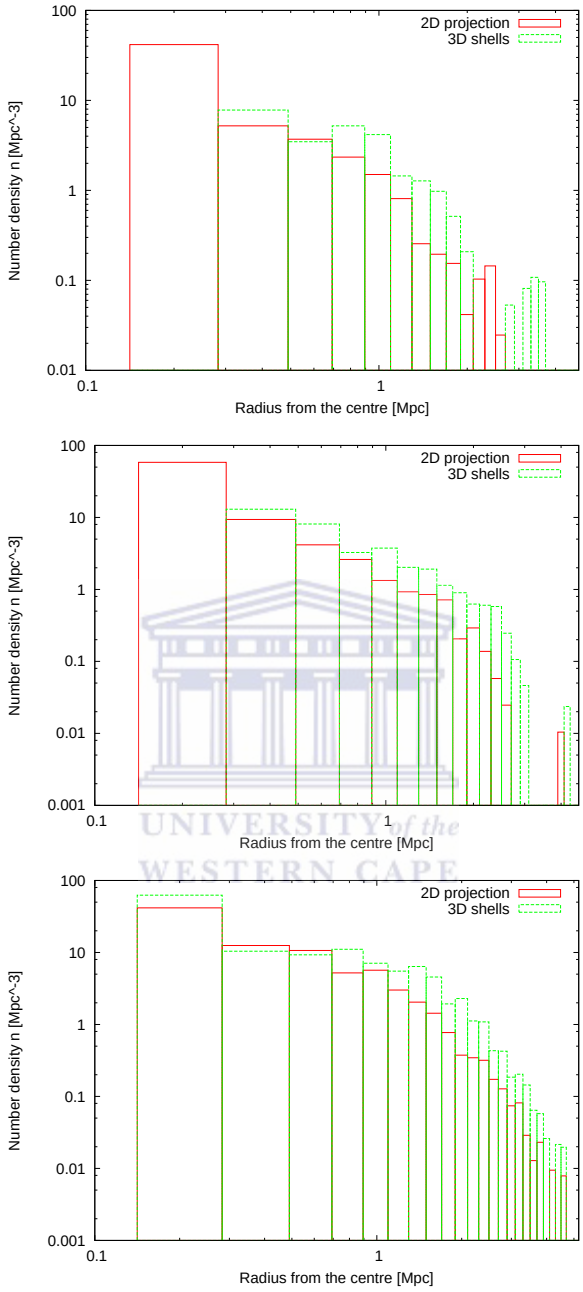

Figure 4.5: The radial distribution of starforming galaxies. Number density in 2D annuli (Mpc^{-2}) are compared with 3D shells (Mpc^{-3}) for galaxies with $sfr > 0.2 M_{\odot} yr^{-1}$. The three rows are clusters with mass $2.045 \times 10^{14} M_{\odot}$ ($R_{vir} = 52.65\ Mpc$) and $5.7 \times 10^{14} M_{\odot}$ ($R_{vir} = 147.63\ Mpc$) at $z = 0.36$, and $1.16 \times 10^{15} M_{\odot}$ ($R_{vir} = 300.44\ Mpc$) at $z = 0.69$. In the last row, we show an example of a cluster that has a significant number of starforming galaxies at its centre.

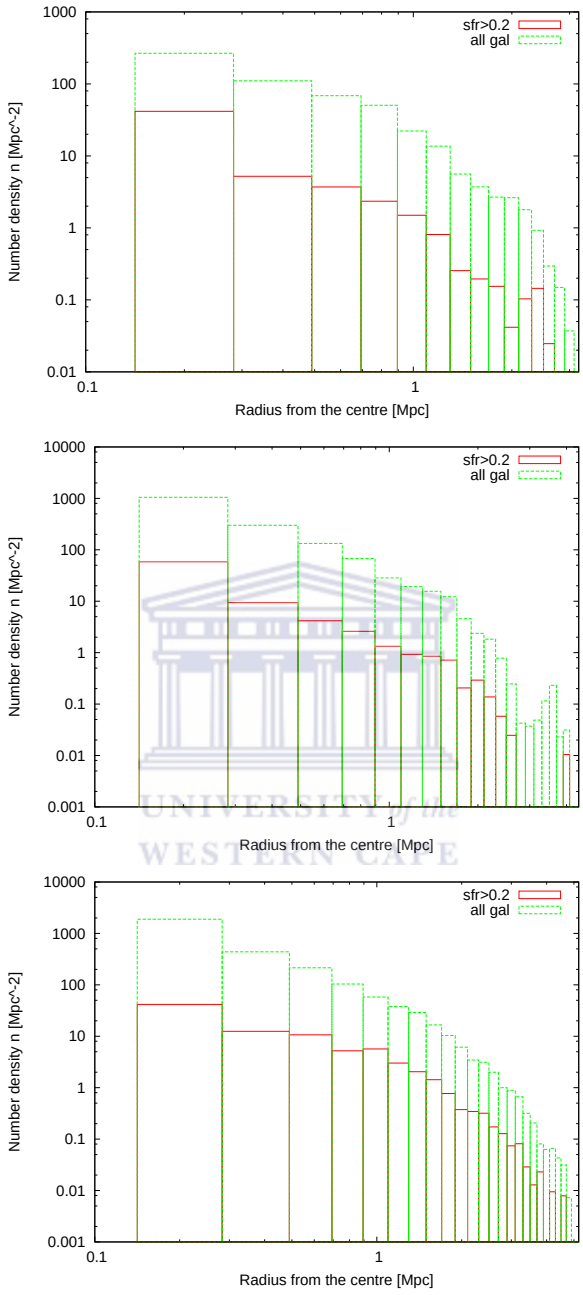

Figure 4.6: Number density of galaxies in 2D (Mpc^{-2}) as a function of radius: comparison of all galaxies in the cluster with those that have $sfr > 0.2 \mathrm{M}_{\odot} yr^{-1}$. The three rows are clusters $2.045 \times 10^{14} M_{\odot}$ and $5.7 \times 10^{14} M_{\odot}$ at $z = 0.36$, and $1.16 \times 10^{15} M_{\odot}$ at $z = 0.69$. In the first cluster, a higher fraction of star forming galaxies can be seen in an infalling halo at the outskirts of cluster

4.3.3 The fraction of star forming galaxies in clusters as a function of cluster size and redshift

Galaxy mergers are more probable in groups than in clusters because the typical speeds of galaxies in groups are lower. One might thus expect low-mass clusters to have a higher fraction of star forming galaxies. To test this idea, we measure n_{rel} where, in 2D,

$$n_{rel} = \frac{N(sfr > 0.2)}{\pi R_{vir}^2 N_{tot}} \tag{4.5}$$

and in 3-D,

$$n_{rel} = \frac{N(sfr > 0.2)}{\frac{4}{3}\pi R_{vir}^3 N_{tot}} \tag{4.6}$$

and N_{tot} is the total number of galaxies in the cluster.

That is, n_{rel} is the number density of galaxies with $sfr > 0.2\mathrm{M}_{\odot}\mathrm{yr}^{-1}$ per Mpc^2 for 2D projections (per Mpc^3 for 3D spherical shells), normalized by the total number of galaxies in the cluster.

We randomly sampled galaxies in clusters with similar virial radius, R_{vir} (which is a function of the virial mass, M_{vir}) and averaged them for three redshifts, at $z = 0.36$, $z = 0.69$ and $z = 1.08$. Given M_{vir} of a virialized cosmological perturbation, its R_{vir} scales as;

$$R_{vir} = 259 \left(\frac{M_{vir}}{10^{12} M_{\odot}} \right)^{\frac{1}{3}} kpc \tag{4.7}$$

In figure 4.7 we observe that n_{rel} is greater for less massive (small R_{vir}) clusters than for more massive clusters. Comparing $n_{rel}(r)$ (profiles for n_{rel}) for 2D to that of 3D we find that, for 2D there is a sharp increase from the centre of the cluster to a maximum followed by an exponential drop. The drop-off is less pronounced in 3D.

In figure 4.8, we find that the profile of $n_{rel}(r)$, where r is the radial distance from the center of the cluster, scales with z. For clusters of the same R_{vir}, $n_{rel}(r)$ is generally greater for higher redshifts. This means that the star formation rate in clusters scales

with redshift, which is consistent with observations. This can be explained by the observational result that the star formation rate globally increases with redshift and peaks at $z \sim 2$ then starts to fall off, summary of global star formation history can be found in Hopkins et al [28]. We therefore expect the star formation rate in clusters to increase with redshift (as one doesn't expect to find clusters at $z > 2$ in a LCDM universe).

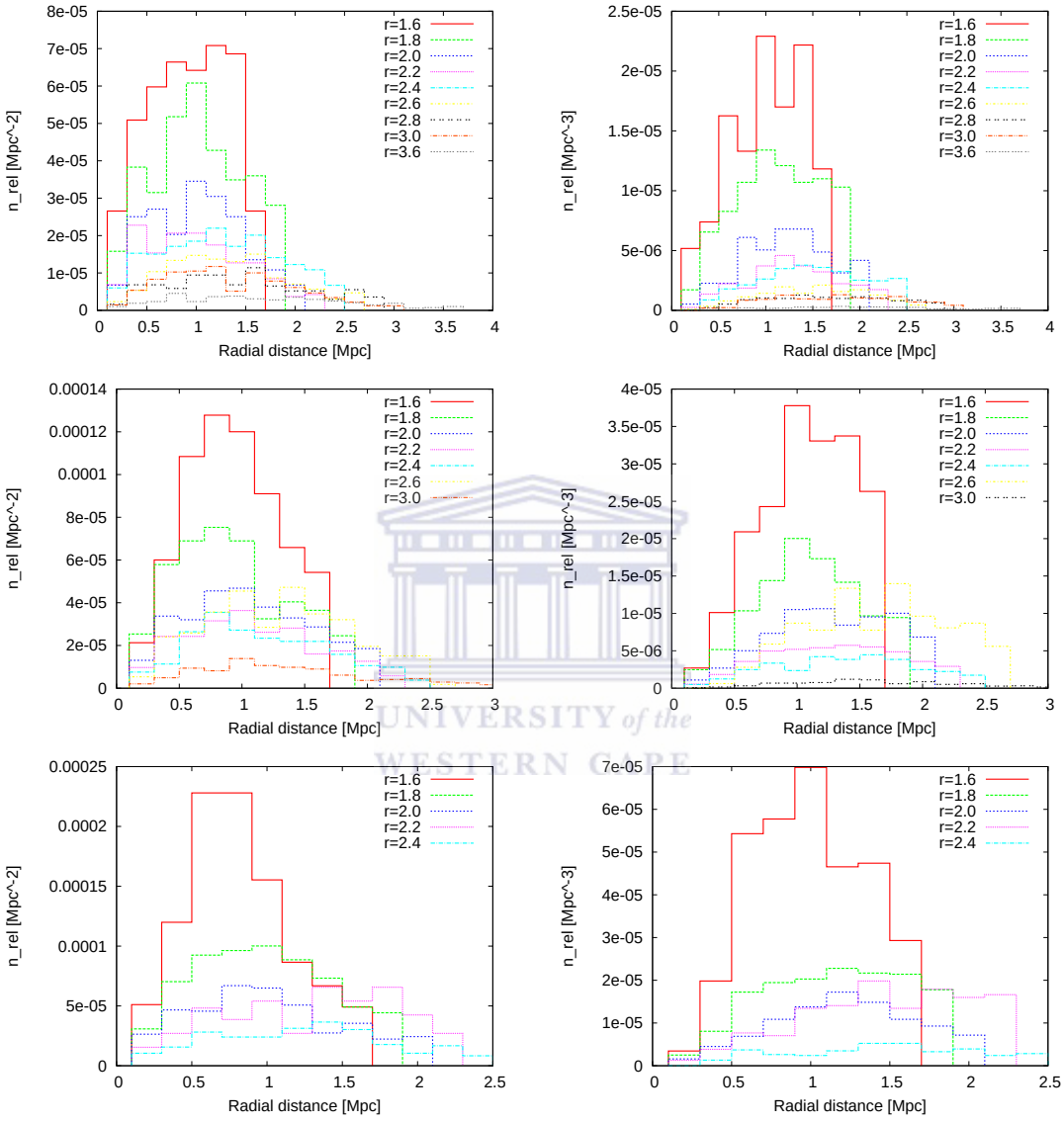

Figure 4.7: The left column is the two dimensional radial distribution and the right column is the three dimensional radial distribution of galaxies with sfr$> 0.2 M_{\odot} yr^{-1}$. The units of n_{rel} in 2D are Mpc^{-2} and in 3D are Mpc^{-3}. In each panel, the average distributions for galaxies with different virial radii, R_{vir} are plotted. The three rows are for redshifts $z = 0.38, 0.69, 1.08$ respectively. Note that n_{rel} decreases with increasing R_{vir}

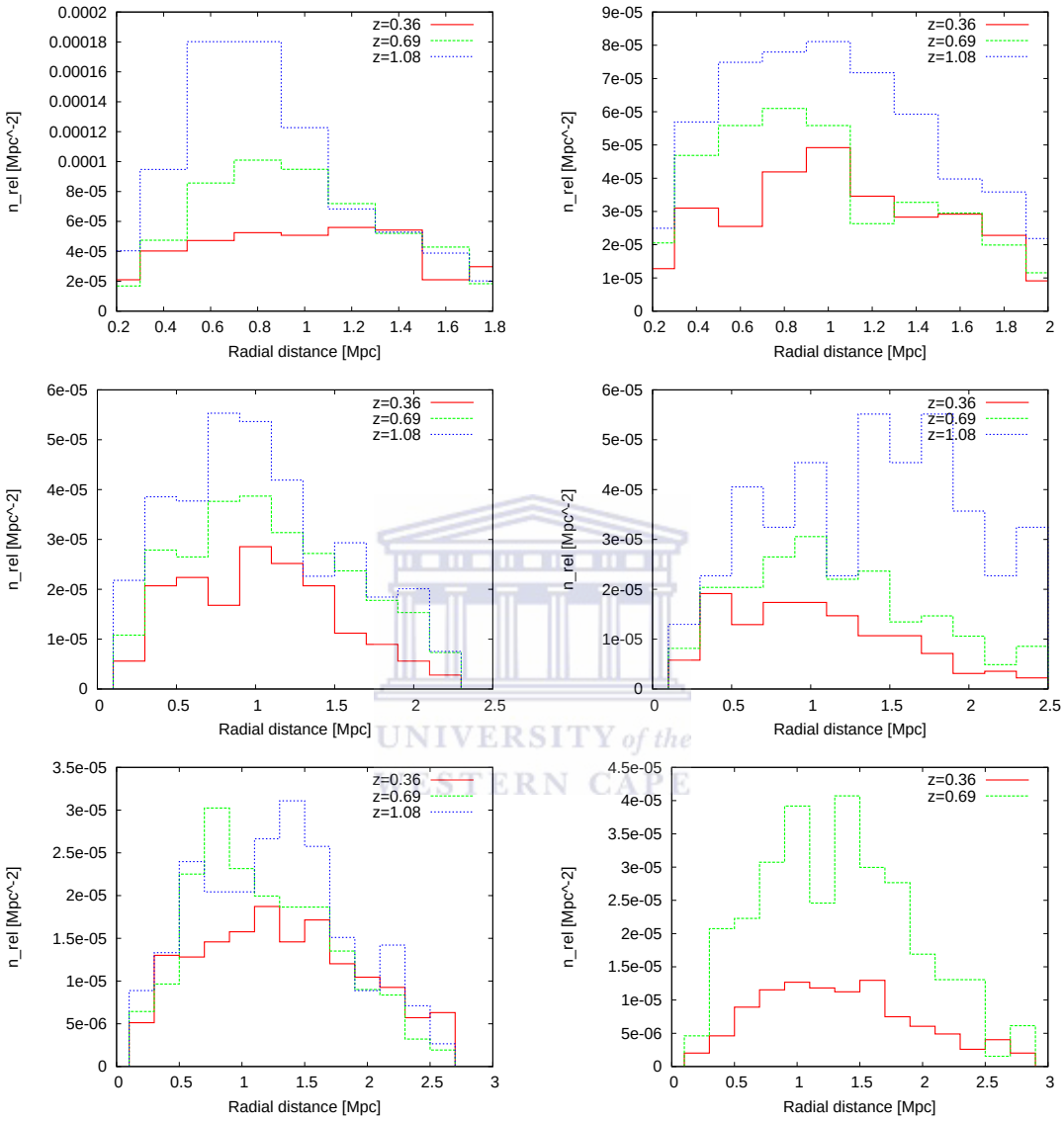

Figure 4.8: Two dimensional radial distribution of galaxies with sfr$> 0.2 M_{\odot} yr^{-1}$. Different plots are for clusters scaled to virial radii of $R_{vir} = 1.8, 2.0, 2.2, 2.4, 2.6, 2.8 Mpc$, from the top left (left to right) to the bottom right respectively. On the vertical axes is the galaxy number count per square Mpc, n_{rel}, normalized to the total number of galaxies in the cluster. This is plotted for three redshifts $z = 0.36, 0.69, 1.08$. Clearly from the figures, n_{rel} scales with z.

4.4 Implied temperature fluctuations from infrared-bright galaxies in clusters

We estimate the contribution to millimeter fluxes in clusters with $M_{vir} \geq 2 \times 10^{14} M_{\odot}$ by totaling up the contribution from the component galaxies with $sfr \geq 0.2 M_{\odot} yr^{-1}$. We used equation 2.33 (section 2.3.4) to estimate the corresponding temperature fluctuations in micro-Kelvin.

We extracted all clusters that satisfy the selection criteria for redshifts snapshots of the millennium simulation from $z = 0.36$ to $z = 1.39$. Flux estimates were obtained at the three frequencies at which the Atacama Cosmology Telescope observes: 265 GHz, 217 GHz, and 145 GHz. The temperature fluctuations were in turn deduced from the fluxes. The tables below show the fluxes and temperature fluctuations at the three frequencies, at $z = 0.36, 0.51, 0.83, 1.08, 1.39$. In the tables, c_{mass} refers to the virial mass of the cluster, $flux$@265, $flux$@217 and $flux$@145 are the fluxes in milliJansky (mJy) at $265GHz$, $217GHz$ and $145GHz$ respectively. $tempflcn$@265, $tempflcn$@217 and $tempflcn$@145 are the corresponding temperature fluctuations in microkelvin, μK. The cluster mass is given in units of $10^{14}\mathrm{M}_{\odot}$.

There is a noticeable dependence of the fluctuations on the virial mass of the cluster and the redshift, this is summarised in figure 4.9, for all the output redshifts between 0.36 to 1.39. From the tables and in figure 4.9 we note a drop in amplitude of temperature fluctuations with redshift, z. The drop occurs despite the increase in total star formation rate in clusters with redshift. This is purely the luminosity distance (d_L) effect, which overwhelms that of the evolution of sfr with z.

The amplitude of temperature fluctuations also scales with cluster mass. Though n_{rel} is greater for less massive clusters than for massive clusters, we note here that the contribution of $sfr > 0.2 M_{\odot} yr^{-1}$ galaxies in the cluster to the SZE is greater for more massive clusters than in less massive ones. The size of the mass bins used is carefully chosen to account for the fact that the cluster mass function changes with z.

We show the dependence of the temperature fluctuation (ΔT) on the three frequencies at which ACT observes. For rows of the plots in figure 4.9, at 265 GHz, the average $\Delta T \simeq 44\mu K$ for the most massive clusters; it drops to $\Delta T \simeq 24.5\mu K$ at 217 GHz, and to $\Delta T \simeq 11\mu K$ at 145 GHz. This effect comes from the SED adopted in section 3.3.

The error bars shown are average absolute deviations, which includes 58% of the sample for a normal distribution. It has to be noted that beyond $z = 1.08$ the error bars cannot be interpreted interms of a normal distribution because there are fewer sources (less than 10 galaxies) in each mass bin

The amplitude of temperature fluctuation can be modeled with redshift as,

$$\log \Delta T = m \log z + C$$

which can be expressed as a power-law,

$$\Delta T = C z^m$$

The typical values of m and C are given in table 4.8. To the first decimal place, $m = -1.8 \pm 0.07$
The values for C vary widely with cluster mass and frequency at which the observations are carried out.

Table 4.1: Fluxes (in mJy) and temperature fluctuations (in K) at z = 0.36 shown for frequencies 145 GHz, 217 GHz and 265 GHz (continues to table 4.3). Cluster mass is in $10^{14} M_{\odot}$. Some rows (chosen randomly) have been omitted since the table contained about 400 rows (too long to be wholly displayed)

cluster mass	Flux@265	tempfln@265	flux@217	tempflcn@217	flux@145	tempflcn@145
2.001	0.99	26.1	0.6	14.67	0.22	6.72
2.089	0.99	26.17	0.6	14.71	0.22	6.74
2.099	0.33	8.78	0.2	4.93	0.07	2.26
2.106	1.6	42.3	0.97	23.77	0.35	10.9
2.140	1.15	30.34	0.7	17.05	0.25	7.82
2.193	1.07	28.19	0.65	15.84	0.24	7.26
2.194	0.66	17.31	0.4	9.73	0.15	4.46
2.203	1.75	46.13	1.06	25.93	0.39	11.88
2.262	0.84	22.25	0.51	12.51	0.19	5.73
2.286	0.72	19.09	0.44	10.73	0.16	4.92
2.291	0.98	25.81	0.59	14.51	0.22	6.65
2.309	0.92	24.35	0.56	13.68	0.2	6.27
2.317	0.8	21	0.48	11.8	0.18	5.41
2.370	1.13	29.9	0.69	16.81	0.25	7.7
2.388	1.46	38.5	0.88	21.64	0.32	9.92
2.390	1.63	43.04	0.99	24.19	0.36	11.09
2.403	0.96	25.36	0.58	14.25	0.21	6.53
2.452	0.75	19.69	0.45	11.07	0.17	5.07
2.454	0.49	12.94	0.3	7.27	0.11	3.33
2.484	0.93	24.58	0.57	13.82	0.21	6.33
2.491	1.34	35.33	0.81	19.85	0.3	9.1
2.491	1.23	32.42	0.75	18.22	0.27	8.35
2.508	1.08	28.57	0.66	16.06	0.24	7.36
2.561	1.34	35.35	0.81	19.87	0.3	9.11
2.586	1.27	33.5	0.77	18.82	0.28	8.63
2.605	0.99	26.1	0.6	14.67	0.22	6.72
2.656	1.03	27.26	0.63	15.32	0.23	7.02
2.663	0.94	24.86	0.57	13.97	0.21	6.4
2.674	1.75	46.14	1.06	25.93	0.39	11.89
2.700	1.44	37.92	0.87	21.31	0.32	9.77
2.741	1.13	29.93	0.69	16.82	0.25	7.71
2.744	1.6	42.27	0.97	23.76	0.35	10.89
2.756	1.57	41.49	0.95	23.32	0.35	10.69
2.779	1.12	29.62	0.68	16.65	0.25	7.63
2.809	0.91	23.92	0.55	13.44	0.2	6.16
2.829	1	26.28	0.6	14.77	0.22	6.77
2.897	1.45	38.35	0.88	21.55	0.32	9.88
2.960	1.53	40.29	0.93	22.64	0.34	10.38

Table 4.2: Fluxes (in mJy) and temperature fluctuations (in K) at z = 0.36 shown for frequencies 145 GHz, 217 GHz and 265 GHz. Cluster mass is in $10^{14} M_{\odot}$.

cluster mass	Flux(265)/mJy	tempfln265/	flux@217GHz	tempflcn@217	flux@145	tempflcn@145
2.971	1.89	49.88	1.15	28.03	0.42	12.85
3.061	1.09	28.84	0.66	16.21	0.24	7.43
3.132	1.19	31.49	0.72	17.7	0.26	8.11
3.235	1.4	37.02	0.85	20.81	0.31	9.54
3.349	1.09	28.81	0.66	16.19	0.24	7.42
3.427	1.12	29.53	0.68	16.59	0.25	7.61
3.506	1.8	47.56	1.09	26.73	0.4	12.25
3.691	1.23	32.53	0.75	18.28	0.27	8.38
3.707	1.32	34.79	0.8	19.55	0.29	8.96
3.778	1.52	40.1	0.92	22.53	0.34	10.33
3.808	1.33	35.04	0.81	19.69	0.29	9.03
3.99	2.1	55.32	1.27	31.09	0.46	14.25
4.027	1.6	42.28	0.97	23.76	0.35	10.89
4.193	1.71	45.18	1.04	25.39	0.38	11.64
4.35	2.22	58.59	1.35	32.93	0.49	15.09
4.482	1.41	37.23	0.86	20.92	0.31	9.59
4.502	2.08	55.03	1.26	30.92	0.46	14.18
4.6	1.27	33.56	0.77	18.86	0.28	8.65
4.802	1.77	46.76	1.07	26.28	0.39	12.05
4.962	1.68	44.24	1.02	24.86	0.37	11.4
5.012	1.43	37.66	0.87	21.16	0.32	9.7
5.171	2.05	54.23	1.25	30.48	0.45	13.97
5.412	1.42	37.42	0.86	21.03	0.31	9.64
5.552	1.74	46.05	1.06	25.88	0.39	11.86
5.635	1.56	41.07	0.94	23.08	0.34	10.58
5.762	1.46	38.65	0.89	21.72	0.32	9.96
5.902	1.81	47.85	1.1	26.89	0.4	12.33
6.187	2.63	69.37	1.59	38.98	0.58	17.87
6.398	2.08	54.95	1.26	30.88	0.46	14.16
6.79	2.37	62.53	1.44	35.14	0.52	16.11
6.941	2.41	63.54	1.46	35.71	0.53	16.37
7.33	1.78	46.92	1.08	26.37	0.39	12.09
7.541	2.58	68.05	1.56	38.24	0.57	17.53
8.346	2.14	56.59	1.3	31.8	0.47	14.58
9.775	2.13	56.18	1.29	31.57	0.47	14.47
10.789	2.78	73.31	1.68	41.2	0.61	18.89
11.243	2.48	65.51	1.51	36.81	0.55	16.88
12.511	2.88	76.12	1.75	42.78	0.64	19.61
22.159	4.02	106.15	2.44	59.66	0.89	27.35

Table 4.3: Fluxes (in mJy) and temperature fluctuations (in K) at z = 0.51 shown for frequencies 145 GHz, 217 GHz and 265 GHz. Cluster mass is in $10^{14} M_{\odot}$. It continues to table 4.5

cluster mass	Flux@265	tempflcn@265	flux@217	tempflcn@217	flux@145	tempflcn@145
2.007	0.53	13.99	0.32	7.87	0.12	3.61
2.054	0.52	13.82	0.32	7.77	0.12	3.56
2.088	0.37	9.64	0.22	5.42	0.08	2.48
2.095	0.69	18.25	0.42	10.26	0.15	4.7
2.11	0.54	14.3	0.33	8.03	0.12	3.68
2.155	0.39	10.34	0.24	5.81	0.09	2.66
2.198	0.48	12.58	0.29	7.07	0.11	3.24
2.22	0.28	7.46	0.17	4.19	0.06	1.92
2.262	0.57	15.1	0.35	8.49	0.13	3.89
2.299	0.62	16.5	0.38	9.27	0.14	4.25
2.317	0.49	13.02	0.3	7.32	0.11	3.36
2.36	0.44	11.66	0.27	6.55	0.1	3
2.382	0.52	13.7	0.31	7.7	0.11	3.53
2.397	0.54	14.15	0.33	7.95	0.12	3.64
2.418	0.44	11.5	0.26	6.46	0.1	2.96
2.424	0.55	14.6	0.34	8.21	0.12	3.76
2.463	0.6	15.95	0.37	8.97	0.13	4.11
2.486	0.43	11.46	0.26	6.44	0.1	2.95
2.51	0.58	15.27	0.35	8.58	0.13	3.93
2.569	0.65	17.28	0.4	9.71	0.14	4.45
2.595	0.95	24.96	0.57	14.03	0.21	6.43
2.645	0.5	13.09	0.3	7.36	0.11	3.37
2.652	0.35	9.23	0.21	5.19	0.08	2.38
2.694	0.57	15.11	0.35	8.49	0.13	3.89
2.737	0.74	19.44	0.45	10.92	0.16	5.01
2.771	0.63	16.53	0.38	9.29	0.14	4.26
2.813	0.71	18.66	0.43	10.49	0.16	4.81
2.86	0.67	17.58	0.4	9.88	0.15	4.53

Table 4.4: Fluxes (in mJy) and temperature fluctuations (in K) at z = 0.51 shown for frequencies 145 GHz, 217 GHz and 265 GHz. Cluster mass is in $10^{14} M_{\odot}$.

cluster mass	Flux@265/mJy	tempfln@265	flux@217GHz	tempflcn@217	flux@145	tempflcn@145
2.902	0.51	13.36	0.31	7.51	0.11	3.44
2.957	0.45	11.84	0.27	6.65	0.1	3.05
2.991	0.58	15.19	0.35	8.54	0.13	3.91
3.023	0.71	18.87	0.43	10.61	0.16	4.86
3.155	0.81	21.48	0.49	12.07	0.18	5.53
3.193	1.03	27.23	0.63	15.31	0.23	7.02
3.3	0.54	14.13	0.32	7.94	0.12	3.64
3.316	0.54	14.3	0.33	8.04	0.12	3.68
3.353	0.84	22.28	0.51	12.52	0.19	5.74
3.401	0.46	12.02	0.28	6.75	0.1	3.1
3.523	0.63	16.58	0.38	9.32	0.14	4.27
3.647	0.93	24.6	0.57	13.83	0.21	6.34
3.683	0.7	18.56	0.43	10.43	0.16	4.78
3.71	0.77	20.22	0.46	11.37	0.17	5.21
3.874	0.71	18.81	0.43	10.57	0.16	4.85
3.951	0.58	15.34	0.35	8.62	0.13	3.95
3.987	0.46	12.21	0.28	6.86	0.1	3.15
4.014	0.74	19.41	0.45	10.91	0.16	5
4.166	0.87	22.9	0.53	12.87	0.19	5.9
4.225	0.61	16.05	0.37	9.02	0.13	4.14
4.301	0.98	25.94	0.6	14.58	0.22	6.68
4.355	0.93	24.44	0.56	13.74	0.21	6.3
4.578	0.92	24.18	0.56	13.59	0.2	6.23
4.863	0.62	16.43	0.38	9.24	0.14	4.23
4.96	0.98	25.74	0.59	14.47	0.22	6.63
5.013	1.44	37.96	0.87	21.34	0.32	9.78
5.117	0.92	24.25	0.56	13.63	0.2	6.25
5.378	0.9	23.87	0.55	13.42	0.2	6.15
5.838	1.21	31.87	0.73	17.91	0.27	8.21
5.997	1.2	31.61	0.73	17.77	0.27	8.14
6.04	0.91	24.01	0.55	13.49	0.2	6.19
6.147	1.09	28.84	0.66	16.21	0.24	7.43
6.299	0.75	19.76	0.45	11.11	0.17	5.09
6.81	1.01	26.77	0.62	15.05	0.22	6.9
10.724	3.2	84.48	1.94	47.48	0.71	21.76
10.878	1.33	35.04	0.81	19.69	0.29	9.03
11.636	1.35	35.63	0.82	20.02	0.3	9.18
12.138	1.88	49.72	1.14	27.94	0.42	12.81

Table 4.5: Fluxes (in mJy) and temperature fluctuations (in K) at z = 0.83 shown for frequencies 145 GHz, 217 GHz and 265 GHz. Cluster mass is in $10^{14} M_{\odot}$.

cluster mass	Flux@265	tempfln@265	flux@217	tempflcn@217	flux@145	tempflcn@145
2.003	0.2	5.24	0.12	2.94	0.04	1.35
2.078	0.17	4.59	0.11	2.58	0.04	1.18
2.091	0.13	3.55	0.08	1.99	0.03	0.91
2.117	0.2	5.27	0.12	2.96	0.04	1.36
2.184	0.22	5.81	0.13	3.27	0.05	1.5
2.225	0.21	5.58	0.13	3.14	0.05	1.44
2.294	0.19	5.01	0.12	2.82	0.04	1.29
2.316	0.15	3.85	0.09	2.16	0.03	0.99
2.366	0.19	5.11	0.12	2.87	0.04	1.32
2.388	0.1	2.65	0.06	1.49	0.02	0.68
2.405	0.15	4.07	0.09	2.29	0.03	1.05
2.434	0.34	9	0.21	5.06	0.08	2.32
2.497	0.25	6.5	0.15	3.65	0.05	1.67
2.552	0.29	7.61	0.17	4.27	0.06	1.96
2.588	0.19	5.12	0.12	2.88	0.04	1.32
2.621	0.25	6.66	0.15	3.74	0.06	1.71
2.671	0.23	6.14	0.14	3.45	0.05	1.58
2.77	0.35	9.16	0.21	5.15	0.08	2.36
2.798	0.27	7.25	0.17	4.07	0.06	1.87
2.841	0.23	6.17	0.14	3.47	0.05	1.59
2.974	0.23	6.11	0.14	3.44	0.05	1.58
3.235	0.2	5.39	0.12	3.03	0.05	1.39
3.46	0.3	7.86	0.18	4.42	0.07	2.02
3.514	0.28	7.41	0.17	4.16	0.06	1.91
3.692	0.22	5.91	0.14	3.32	0.05	1.52
3.821	0.29	7.69	0.18	4.32	0.06	1.98
4.051	0.27	7.12	0.16	4	0.06	1.83
4.453	0.26	6.99	0.16	3.93	0.06	1.8
4.9	0.26	6.94	0.16	3.9	0.06	1.79
5.328	0.28	7.5	0.17	4.22	0.06	1.93
5.544	0.31	8.28	0.19	4.65	0.07	2.13
5.752	0.35	9.31	0.21	5.23	0.08	2.4
5.83	0.35	9.13	0.21	5.13	0.08	2.35
6.025	0.49	13	0.3	7.31	0.11	3.35
6.527	0.41	10.92	0.25	6.14	0.09	2.81
8.84	0.61	16.21	0.37	9.11	0.14	4.18

Table 4.6: Fluxes (in mJy) and temperature fluctuations (in K) at z = 1.08 shown for frequencies 145 GHz, 217 GHz and 265 GHz. Cluster mass is in $10^{14} M_{\odot}$.

cluster mass	Flux@265	Tempfln@265	flux@217	tempflcn@217	flux@145	tempflcn@145
2.014	0.12	3.08	0.07	1.73	0.03	0.79
2.059	0.13	3.47	0.08	1.95	0.03	0.89
2.084	0.12	3.29	0.08	1.85	0.03	0.85
2.138	0.12	3.07	0.07	1.73	0.03	0.79
2.193	0.12	3.05	0.07	1.72	0.03	0.79
2.223	0.13	3.37	0.08	1.89	0.03	0.87
2.266	0.14	3.6	0.08	2.02	0.03	0.93
2.297	0.11	2.95	0.07	1.66	0.02	0.76
2.315	0.1	2.59	0.06	1.46	0.02	0.67
2.351	0.2	5.22	0.12	2.93	0.04	1.34
2.43	0.1	2.63	0.06	1.48	0.02	0.68
2.515	0.16	4.16	0.1	2.34	0.03	1.07
2.548	0.14	3.78	0.09	2.12	0.03	0.97
2.625	0.13	3.47	0.08	1.95	0.03	0.89
2.657	0.19	5.12	0.12	2.88	0.04	1.32
2.664	0.1	2.75	0.06	1.55	0.02	0.71
2.678	0.17	4.49	0.1	2.52	0.04	1.16
2.864	0.17	4.39	0.1	2.47	0.04	1.13
2.971	0.17	4.5	0.1	2.53	0.04	1.16
3.021	0.11	2.8	0.06	1.58	0.02	0.72
3.049	0.18	4.85	0.11	2.73	0.04	1.25
3.085	0.2	5.19	0.12	2.92	0.04	1.34
3.18	0.17	4.52	0.1	2.54	0.04	1.17
3.241	0.17	4.47	0.1	2.51	0.04	1.15
3.418	0.13	3.46	0.08	1.95	0.03	0.89
3.464	0.17	4.5	0.1	2.53	0.04	1.16
3.918	0.19	4.89	0.11	2.75	0.04	1.26
3.938	0.12	3.27	0.08	1.84	0.03	0.84
4.122	0.22	5.8	0.13	3.26	0.05	1.49
4.501	0.19	5.04	0.12	2.83	0.04	1.3
4.741	0.31	8.13	0.19	4.57	0.07	2.09
7.173	0.31	8.16	0.19	4.59	0.07	2.1

Table 4.7: Fluxes (in mJy) and temperature fluctuations (in K) at z = 1.39 shown for frequencies 145 GHz, 217 GHz and 265 GHz. Cluster mass is in $10^{14} M_{\odot}$.

cluster mass	Flux@265	tempflcn@265	flux@217	tempflcn@217	flux@145	tempflcn@145
1.987	0.08	2.05	0.05	1.15	0.02	0.53
2.037	0.11	2.99	0.07	1.68	0.03	0.77
2.112	0.11	2.98	0.07	1.67	0.02	0.77
2.119	0.08	2.17	0.05	1.22	0.02	0.56
2.155	0.08	1.99	0.05	1.12	0.02	0.51
2.187	0.08	2.02	0.05	1.14	0.02	0.52
2.275	0.14	3.75	0.09	2.11	0.03	0.97
2.303	0.08	2.1	0.05	1.18	0.02	0.54
2.507	0.09	2.33	0.05	1.31	0.02	0.6
2.539	0.09	2.4	0.06	1.35	0.02	0.62
2.979	0.1	2.54	0.06	1.43	0.02	0.65
3.054	0.12	3.04	0.07	1.71	0.03	0.78
3.257	0.12	3.21	0.07	1.8	0.03	0.83
6.125	0.14	3.76	0.09	2.11	0.03	0.97

Table 4.8: Typical values of m and C

$2 \leq$ M < 2.4 ($\times 10^{14}$M$_{\odot}$)			
frequency	$145GHz$	$217GHz$	$265GHz$
m	-1.84531	-1.84119	-1.84119
c	0.00831556	0.347524	0.597524
$2.4 \leq$ M < 3.5($\times 10^{14}$M$_{\odot}$)			
frequency	$145GHz$	$217GHz$	$265GHz$
m	-1.81563	-1.82764	-1.82764
c	0.0828811	0.418636	0.668636
$\geq 3.5 \times 10^{14}$M$_{\odot}$			
frequency	$145GHz$	$217GHz$	$265GHz$
m	-1.78627	-1.7868	-1.7809
c	0.229403	0.566667	0.818775

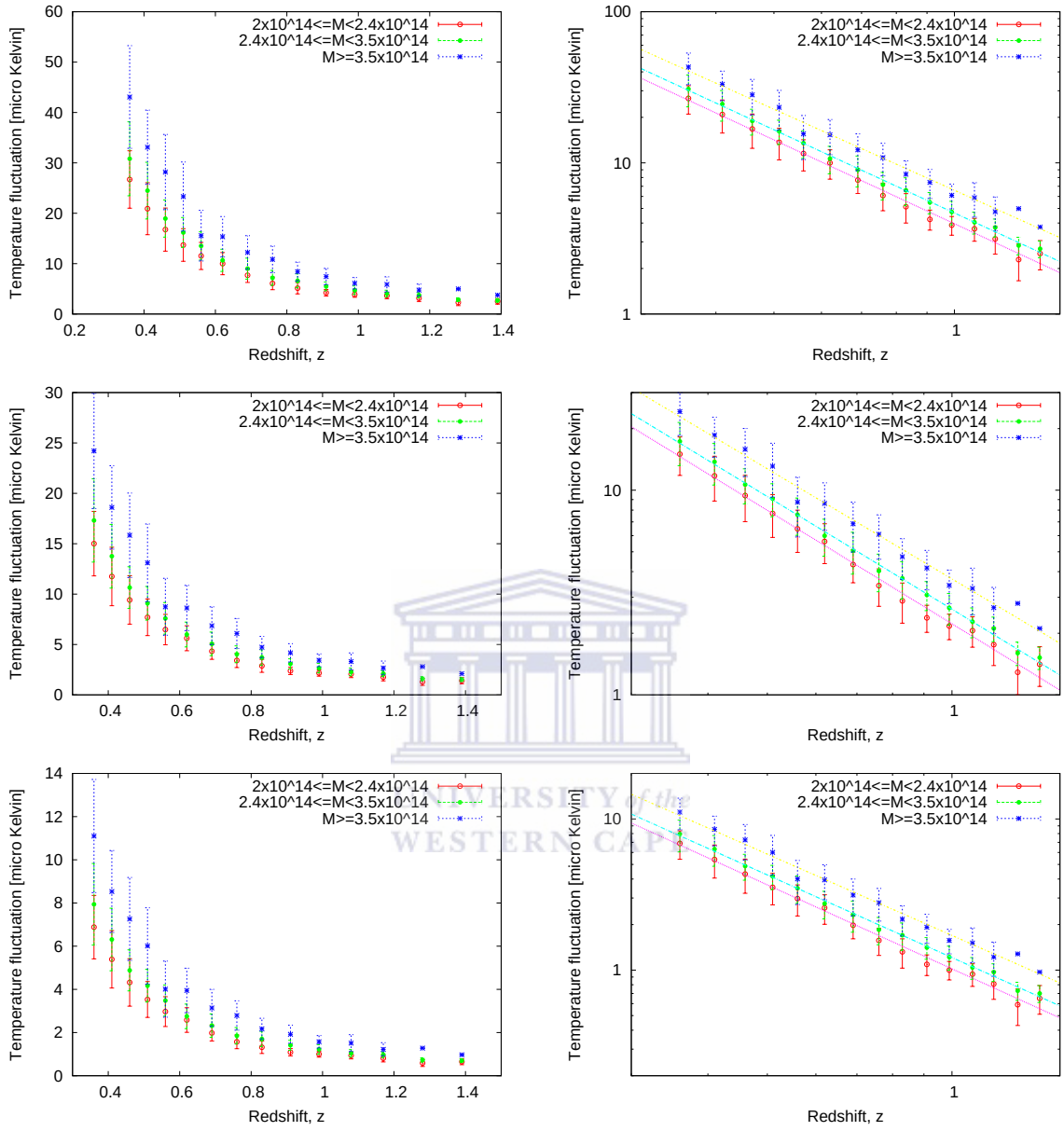

Figure 4.9: Variation of the temperature fluctuation with redshift. The right column is the log-log plot of the first column. The rows are plots for 265 GHz, 217 GHz and 145 GHz respectively. This is plotted for three mass bins, $2.0 \times 10^{14} \leqq M < 2.4 \times 10^{14}$, $2.4 \times 10^{14} \leqq M < 3.5 \times 10^{14}$, and $M \geqq 3.5 \times 10^{14}$. These mass bins were chosen this way to account for the fact that cluster mass function drops off with redshift. On the vertical axis is the average temperature fluctuation for each of the mass bins, and the errorbars are deviations from the average value (average deviation; a reason why the error bars are so small at high z; few cluster), which for a normal distribution includes 58% of the sample. There is a drop in magnitude of the fluctuations with z, and an increase of the magnitude with cluster mass. The lines are first order polynomial fits

4.4.1 Magnitude of point-source contributions compared to SZ signatures

Galaxy clusters have typical temperatures of orders of $k_B T_e = 1 - 10keV$, with some claims of temperatures as high as $17keV$ for very massive clusters. We can carry out some analytical estimates to determine the kind of temperatures expected from the thermal and kinetic SZE.

For a gas within a cluster's gravitational potential well, its electron temperature can be approximated by

$$k_B T_e \approx \frac{G M m_p}{2 R_{eff}} \tag{4.8}$$

$$\approx 7 \left(\frac{M}{3 \times 10^{14} M_\odot} \right) \left(\frac{R_{eff}}{Mpc} \right)^{-1} keV \tag{4.9}$$

where M is the cluster mass and R_{eff} is the cluster's effective radius (the radius at which mass is half the total mass). For example the most massive cluster at $z = 0.36$, $M = 2.21 \times 10^{15} \mathrm{M}_\odot$, can have a temperature of $\gtrsim 11keV$.

For low-energy scattering, the cross-section is Thomson scattering, σ_T (ref. section 2.3.1), the optical depth is therefore given by $\tau_e \approx n_e \sigma_T R_{eff}$. τ_e has typical values of $\sim 10^{-2}$. The typical values of mean change of photon energy produced by the scattering is approximately

$$\Theta = \frac{\Delta \nu}{\nu} \approx \frac{k_B T_e}{m_e c^2} \tag{4.10}$$

which gives an estimate of about $\sim 10^{-2}$. For the very massive cluster, like the one at $z = 0.36$ above, with $k_B T_e \gtrsim 11keV$, we obtain $\Theta \gtrsim 2 \times 10^{-2}$
The magnitude of thermal SZE is of order $\frac{\Delta T_{th}}{T_{rad}} \approx \tau_e \Theta \approx 10^{-4}$ (for an average mass cluster). We therefore expect to observe thermal SZ signals of about 270 μK

From section 2.3.2, the magnitude of kinetic SZE can be estimated by $\frac{\Delta T_{RJ}}{T_{rad}} = \tau_e \beta$, where $\beta = v_z/c$. On average $v_z \approx 300 kms^{-1}$, giving the magnitude of the kinetic SZ signal to be about 30 μK.
The level of contamination caused by the submillimeter sources in clusters can clearly not be neglected.

4.4.2 Removing bright point sources and residual temperature fluctuations

The magnitude of ΔT displayed in the tables and in figure 4.9, as mentioned before, is obtained by totaling up the contribution from all the component galaxies with $sfr > 0.2 M_{\odot} yr^{-1}$. Depending on the resolution of the survey and the availability of follow up observations, some of the contaminating sources can be identified as infrared/submilimeter point sources. To get an idea of the resolutions we are talking about, we note ACT has a resolution of about $1.3'$ and a 3 Mpc diameter cluster at $z = 0.36$ has an angular scale of about $5'$, so most of the relatively massive clusters can be resolved at such redshift.

The surveys that can be used to carry out follow-up observations to pick out some of the point sources would include Spitzer space telescope and Submillimetre Common-User Bolometer Array (SCUBA). SCUBA is mounted on the James Clerk Maxwell Telescope (JCMT) and has a limiting flux density of about $2mJy$, it can only pick out brighter sources, which are rare in clusters with the mass limit we considered. The flux density limit for a reasonable Spitzer survey at $24\mu m$ is about $110\mu Jy$. At $z = 0.36$ this would correspond to a luminosity of,

$$L_{24\mu m} = 4\pi d_L^2 f_{24\mu m} \tag{4.11}$$

where d_L is the Luminosity distance. Thus

$$L_{24\mu m} = 5.72 \times 10^{42} ergs^{-1} = 1.49 \times 10^9 L_{\odot}$$

Sajina et al (2006) fitted a relation between mid-infrared ($L_{24\mu m}$) and the total infrared luminosity L_{IR} in the galaxy, they obtained a $\log - \log$ linear relation given below,

$$\log L_{24\mu m} = (1.13 \pm 0.05) \times \log L_{IR} - (2.5 \pm 0.5) \tag{4.12}$$

Using equation 4.12, we can deduce the sub-mm flux corresponding to the 24 μm flux limit of 110 μJy at $z = 0.36$: 110 μJy at 24 μm gives $L_{IR} \approx 2.14 \times 10^{10} L_{\odot}$, which results in flux density limits at 145 GHz, 217 GHz and 265 GHz shown in table 4.9.

This means we can treat sources with flux greater than the limits listed in table 4.9 as

Table 4.9: flux limits

Frequency (GHz)	145	217	265
flux limit (mJy)	0.05	0.14	0.23

point sources and pick them out. By doing this, we shall be able to reduce the contamination of the infrared bright galaxies within the cluster to the SZ signal.

Considering again the most massive cluster in the simulation at $z = 0.36$, $2.21 \times 10^{15} M_{\odot}$, if we remove contribution from all the sources with $flux \gtrsim 0.05, 0.14, 0.23 mJy$ as in the table 4.9 above, the magnitude of ΔT reduces by a considerably large amount, table 4.10. ΔT_{orig} is the total temperature from all the infrared sources within the cluster, and ΔT_{rest} is the temperature fluctuation that results after subtracting above the respective flux limit sources.

Table 4.10: magnitude of ΔT

Frequency (GHz)	145	217	265
$\Delta T_{orig}(\mu K)$	27.35	59.66	106.15
$\Delta T_{rest}(\mu K)$	13.65	29.66	52.75

Chapter 5

Conclusion

In this project we modelled IR-bright galaxies in the millenium simulation using the relationship between IR-luminosity and star formation rate. We showed that this model satisfies observational constraints from Spitzer surveys fairly well.

We used our modelling to study the distribution of galaxies in simulated galaxy clusters, looking at properties such as the radial number density of star forming galaxies (n_{sf}). n_{sf} generally falls off with the radius, r. We observe bumps outside the virial radius for some clusters that signify substructures. Some of the substructures are at the periphery of the clusters, and have higher star formation rates relative to other regions at the same radius.

We also found that in some clusters, there are numerous galaxies with sfr $\geq 0.2\mathrm{M}_{\odot}\mathrm{yr}^{-1}$ within $r \leq 0.2$Mpc spherical volume which we attribute to cluster merging. This is more pronounced in less massive clusters.

In n_{rel} plots we noted the difference in profiles for 2D projections and 3D shell volumes. 2D projected view tends to concentrate galaxies at the centre of the cluster. We observe a drop in n_{rel} (sfr $> 0.2\mathrm{M}_{\odot}\mathrm{yr}^{-1}$) with R_{vir}. Despite more massive galaxies containing more galaxies with sfr $> 0.2\mathrm{M}_{\odot}\mathrm{yr}^{-1}$, the relative number count of these galaxies is less in more massive clusters than in less massive clusters.

We estimated the total fluxes and the corresponding temperature fluctuations arising from faint infrared galaxies within galaxy clusters. We then computed the effect of these galaxies in contaminating the SZ signal from clusters. We classified the contamination into cluster mass bins at different redshifts, and did this for three ACT observing frequencies (145 GHz, 217 GHz, 265 GHz). We obtained a power-law relation between the magnitude of ΔT and z for all the 3 mass bins we considered, and at all frequencies. The fitting formula is of the form $\Delta T = Cz^m$, where C is a constant determined by obtaining the ΔT intercept of the relation. To the first decimal place, we found $m = 1.8 \pm 0.07$, and C takes a range of values for all the 3 mass bins and frequencies.

We conclude that infrared (IR) galaxies within clusters contribute a non-negligible contamination of the SZ signal from clusters. The contamination can be reduced if follow-up observations and/or higher resolution data allow the brighter sources to be extracted . Surveys such as that by Spitzer space telescope can be used to carry out modelling of these sources and thereafter reduce the contamination by up to more than 55%.

Future work

In this project we carried out the modelling of infrared SZE contaminants within clusters purely from simulation data. There is a need to supplement our findings with the observational data. Giard et al 2008 studied the infrared luminosity of galaxy clusters and modeled it with redshift. Future studies would include using such data to model the SZE contamination by infrared galaxies in cluster and compare with the models we obtained from simulations.

New data on IR/sub-mm sources from Spitzer, Balloon-borne Large Aperture Submillimeter telescope (BLAST), AZTEC (a 144 element bolometer array in the Large Millimeter Telescope (LMT)), etc can be used to further refine models of IR-bright sources.

Our work provides improved modelling of the positions of IR-bright galaxies in clusters.

This approach can be used to generate simulated CMB maps which give a better description of the SZ-contamination.

Chapter 6

Appendix

6.1 Radiation energy density in Compton scattering

This section shows the derivation for the transformation of the radiation energy density U'_{rad} in the electron's rest frame, P' to the radiation energy density U_{rad} in the lab frame, P in Compton scattering. Let an electron be moving in a positive x-direction with speed $v = v_x$ in the lab frame, such that it is hit successively by two low-energy photons in a parallel beam approaching from an angle θ in the lab frame as illustrated in the geometry below.

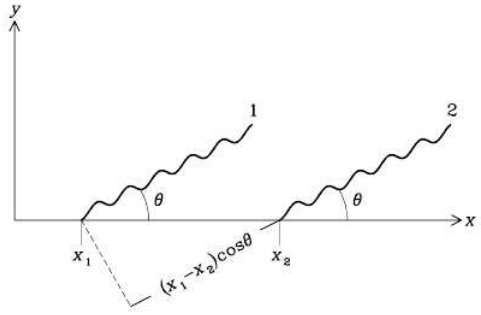

Figure 6.1: Two low energy photons in a parallel beam stricking the moving electron at an angle θ from the x axis, as seen in the lab frame.

The coordinates of the two successive photons in the lab frame is therefore $(x_1, 0, 0, t_1)$ and $(x_2, 0, 0, t_2)$, with the corresponding Lorentz transformation $(\gamma v_{t_1'}, 0, 0, \gamma t_1')$ and $(\gamma v_{t_2'}, 0, 0, \gamma t_2')$ respectively.
In the lab frame, the time t elapsed between the arrival of these two photons at the plane normal to the direction of propagation will be

$$\begin{aligned} \Delta t &= t_2 + \frac{(x2 - x1)}{c} cos\theta - t_1 && (6.1) \\ &= \gamma t_2 + \frac{(\gamma v t_2' - \gamma v t_1')}{c} cos\theta - \gamma t_1 && (6.2) \\ &= (t_2' - t_1')[\gamma(1 + \beta cos\theta)] && (6.3) \end{aligned}$$

were $t_2' - t_1' = \Delta t'$ is time elapse between the two photons in the electron's (P') frame.

$$\Delta t = \Delta t'[\gamma(1 + \beta cos\theta)] \tag{6.4}$$

This implies that the time rate of arrival of photons is shorter by a factor $\gamma(1 + \beta cos\theta)$ in P' frame. Similarly, if N is the photon number density in the lab frame, then $N' = N[\gamma(1 + \beta cos\theta)]$
Since in the lab frame $U_{rad} = N\hbar\omega$, we can then have,

$$U_{rad}' = U_{rad}[\gamma(1 + \beta cos\theta)]^2 \tag{6.5}$$

This is the energy density associated with the photons incident at angle θ in the P frame and arriving from a solid angle $2\pi sin\theta d\theta$. If the radiation field in lab (P) frame is assumed to be isotropic, then the total energy density in the electron (P') frame is obtained by integrating over all directions (the solid angle), that is.

$$U_{rad}' = \frac{U_{rad}}{4\pi} \int_{\phi=0}^{2\pi} \int_{\theta=0}^{\pi} [\gamma(1 + \beta cos\theta)]^2 sin\theta d\theta d\phi \tag{6.6}$$

ϕ being the azimuthal angle around the x axis. The result of the integration is,

$$U_{rad}' = \frac{4}{3} U_{rad}(\gamma^2 - \frac{1}{4}) \tag{6.7}$$

which gives energy radiation rate of,

$$\left(\frac{dE}{dt}\right) = \frac{4}{3}\sigma_T c U_{rad}(\gamma^2 - \frac{1}{4}) \tag{6.8}$$

as the total energy in the radiation field after inverse-Compton upscattering of low-energy photons.

6.2 Derivation of thermal SZE for relativistic limit

If we take the geometry as that in fig 2.1, where the electron velocity $v_e = \beta c$, $\mu = \cos\theta$ in P frame, and $\mu' = \cos\theta'$ in P' frame. Chandrasekhar (1979) showed that the probability of scattering a photon originally moving in a direction $\mu = \cos\theta$ with respect to the electron, into a direction $\mu' = \cos\theta'$ can be expressed as follows.

$$f(\mu', \mu) = \frac{3}{8}\left(1 + \mu^2\mu'^2 + \frac{1}{2}\left(1 - \mu^2\right)\left(1 - \mu' 2\right)\right) \tag{6.9}$$

such that the change in photon direction causes the scattered photon to appear at frequency

$$\nu'' = \nu\left(1 + \beta\nu'\right)\left(1 - \beta\nu\right)^{-1} \tag{6.10}$$

Writing the resultant scatter in terms of the logarithmic frequency shift caused by a scattering, s as $s = \log\left(\nu''/\nu\right) = \ln\left(\frac{1+\beta\mu'}{1-\beta\mu}\right)$, one can then express the probability for the scattering of a single photon as

$$P(s, \beta)ds = \int p(\mu) f(\mu', \mu)\left(\frac{d\mu'}{ds}\right) ds \tag{6.11}$$

where

$$p(\theta)d\theta = p(\mu)d\mu = \left(2\gamma^4(1 - \beta\mu)^3\right)^{-1} d\mu'$$

is the probability of a photon scattering with angle θ, and γ is the Lorentz factor.
For a population of electrons, the distribution of photon frequency shifts caused by population scattering can be obtained from $P(s, \beta)$ by averaging over the electron β distribution [6]. If β_{lim} is the minimum value of β capable of causing a frequency shift s, then for

photons that have been scattered once, the probability of s, $P_1(s)$ is

$$P_1(s) = \int_{\beta_{lim}}^{1} p_e(\beta) d\beta P(s,\beta) \tag{6.12}$$

and $p_e(\beta)d\beta$ is electron velocity distribution, which in this case is taken to be a relativistic Maxwellian distribution.
If all the incident photons within the spectrum $I_0(\nu)$ are scattered once where

$$I_0(\nu) = \frac{2h\nu^3}{c^2}\left(e^{\frac{h\nu}{k_B T_{rad}}} - 1\right)^{-1}, \tag{6.13}$$

then the resulting spectrum of the CMB after scatter will be of the form,

$$\frac{I(\nu)}{\nu} = \int_0^{\infty} P_1(\nu,\nu_0)\frac{I_0(\nu_0)}{\nu_0} \tag{6.14}$$

where $P_1(\nu,\nu_0)$ is the probability that a scattering occurs from frequency ν_0 to ν, and $\frac{I(\nu)}{\nu}$ is the spectrum in photon number terms [4]. $P_1(\nu,\nu_0) = \frac{P_1(s)}{\nu}$, where $P_1(s)$ is the frequency shift function in 6.12. 6.14 can be thus be written in terms of s as,

$$I(\nu) = \int_{-\infty}^{\infty} P_1(s) I_0(\nu_0) ds \tag{6.15}$$

The change in the radiation spectrum at frequency ν is

$$\Delta I(\nu) = I(\nu) - I_0(\nu) = \frac{2h}{c^2}\int_{-\infty}^{\infty} P_1(s) ds \left(\frac{\nu_0^3}{e^{\frac{h\nu_0}{k_B T_{rad}}} - 1} - \frac{\nu^3}{e^{\frac{h\nu}{k_B T_{rad}}} - 1}\right) \tag{6.16}$$

The above equation is for a single photon scatter, which collectively can still lead to a significant shift in the spectrum as in section 2.3. Now let us consider general situations (even in tenuous plasma like that in the intracluster medium) where photons are scattered 0, 1, 2, or more times. If τ_e is the optical depth to scattering through the electron cloud, we can express the probability of a photon emerging out of the cloud unscattered as $e^{-\tau_e}$ and the probability that it is once scattered is $\tau_e e^{-\tau_e}$ and for N scattering the probability becomes

$$p_N = \frac{\tau_e^N e^{-\tau_e}}{N!} \tag{6.17}$$

The full frequency distribution function from the scattering is the weighted sum over the probabilities

$$P(s) = e^{-\tau_e}\left(\delta(s) + \tau_e P_1(s) + \frac{1}{2!}\tau_e^2 P_1(s) \otimes P_1(s) + ...\right) \tag{6.18}$$

where $\otimes$ is the convolution and δ is a delta function.
As noted earlier, the electron scattering medium in the clusters is optically thin, with $\tau_e \ll 1$, of orders not more than 0.01. such that equation 6.18 can be approximated by

$$P(s) = (1 - \tau_e)\delta(s) + \tau_e P_1(s) \tag{6.19}$$

The resulting intensity change is as that of a single photon scatter but has an amplitude reduced by a factor τ_e, Such that the resulting intensity change is reduced by a factor τ_e from that of a single photon scatter, 6.16.

$$\Delta I(\nu) = I(\nu) - I_0(\nu) = \frac{2h}{c^2}\tau_e \int_{-\infty}^{\infty} P_1(s)ds \left(\frac{\nu_0^3}{e^{\frac{h\nu_0}{k_B T_{rad}}} - 1} - \frac{\nu^3}{e^{\frac{h\nu}{k_B T_{rad}}} - 1}\right) \tag{6.20}$$

6.3 The kinetic SZE

If the occupation number of the photons is of Planck form

$$n_\alpha = \left(e^{h\nu/k_B T_{rad}} - 1\right)^{-1} \tag{6.21}$$

for $\alpha = 1$, 2 and T_{rad} being the radiation temperature of the CMB as noted before, then the occupation number in a frame moving at speed v_z along the z-axis away from the observer will be

$$n_\alpha = (exp(x_1\gamma_z(1 - \beta_z\mu_1)) - 1)^{-1} \tag{6.22}$$

where $x_1 = h\nu/k_B T_1$ is the dimensionless frequency of photons in the frame of scattering medium. The radiation temperature of the CMB as seen by an observer at rest in the Hubble flow near the scattering gas is $T_1 = T_{rad}(1 + z_H)$, z_H is the Hubble flow redshift, and $\beta_z = v_z/c$ is the peculiar velocity. γ_z is the corresponding Lorentz factor. $\mu_1 = cos\theta_1$ is the directional cosine of photons arriving at a scattering electron relative to the z-axis

and measured at the frame of the moving scattering medium [6]. The geometry is illustrated in figure 6.2.

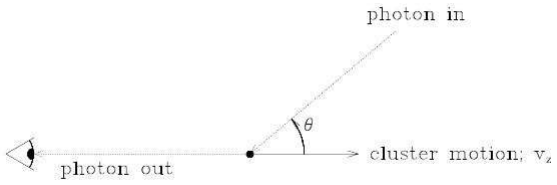

Figure 6.2: § [6] Geometry of the kSZE as seen in the frame of an observer at rest in the Hubble flow

If ν is the frequency in the rest frame relative to the CMB, then the relativistic relation between ν and ν_1 (frequency as seen by an observer at rest in the Hubble flow) is given by

$$\nu_1 = \gamma_z(1+\beta_z)\nu \tag{6.23}$$

where in the z-axis $\mu = cos\theta = 1$.
Using the radiative transfer equation, Birkinshaw (1998) expressed an equation for the specific intensity due to scattering as

$$\frac{dI_\nu(\mu)}{d\tau_e} = \int_{-1}^{+1} d\mu_1 f(\mu,\mu_1)\left(I_{\nu_1}(\mu_1) - I_{\nu_1}(\mu)\right) \tag{6.24}$$

where $\tau_e = \int \alpha_{\nu,sca} dz$ is the optical depth, $f(\mu,\mu_1)$ is the scattering redistribution function. If photons are scattered only once (cases of small optical depth), the above equation can be simplified to

$$\frac{I_{\nu_1}(\tau_e,\mu) - I_{\nu_1}(0,\mu)}{\tau_e} = \int_{-1}^{+1} d\mu_1 f(\mu,\mu_1)\left(I_{\nu_1}(0,\mu_1) - I_{\nu_1}(0,\mu)\right) \tag{6.25}$$

For $\mu = 1$, f takes a simple form, such that the fractional change in specific intensity becomes

$$\frac{\Delta I_\nu}{I_\nu} = \tau_e \int_{-1}^{+1} d\mu_1 \frac{3}{8}(1+\mu_1^2)\left(\frac{I_{\nu_1}(0,\mu_1)}{I_{\nu_1}(0,1)} - 1\right) \tag{6.26}$$

Due to invariance of the left hand side of the above equation, the same fractional intensity change would be seen by an observer in the rest frame of the CMB at frequency ν. Working in terms of the frequency seen at redshift zero (that is ν), and using 6.22 for n_α, the fractional intensity change becomes

$$\frac{\Delta I_\nu}{I_\nu} = \tau_e \int_{-1}^{+1} d\mu_1 \frac{3}{8}(1+\mu_1^2)\left(\frac{e^x-1}{e^{x_2}-1}-1\right) \tag{6.27}$$

where $x_2 = x\gamma_z^2(1+\beta_z)(1-\beta_z\mu_1)$ and $x = \frac{h\nu}{k_B T_{rad}}$. For small β_z, by expanding the integral in powers of β_z, and neglecting odd terms of the integrand, we end up with

$$\frac{\Delta I_\nu}{I_\nu} = -\tau_e \beta_z \frac{xe^x}{e^x-1} \tag{6.28}$$

Bibliography

[1] Bahcall A. Neta, Fan Xiaohui, and Cen Renyue, 1997. "Constraining Ω Cluster Evolution". astro-ph/9706018v1.

[2] Bahcall A. Neta, 1997. "Tracing the Universe with Clusters of Galaxies". astro-ph/9711062v2.

[3] Baugh C. M. 2006 "A primer on hierarchical galaxy formation: the semi-analytical approach". astro-ph/0610031v2

[4] Bennett C. L. et al, 2003. "First Year *Wilkinson Microwave Anisotropy Probe (WMAP)* Observations: Preliminary Maps and Basic Results". astro-ph/0302207v3

[5] Bertschinger Edmund, 1998 "Simulations of structure formation in the universe". Annu. Rev. Astron. Astrophys. 1998. 36:599654.

[6] Birkinshaw Mark 1998. "The Sunyaev-Zel'dovich Effect", astro-ph/9808050v1.

[7] Bruzual G. and Charlot S. 2003. "Stellar population synthesis at the resolution of 2003". Mon. Not. R. Astron. Soc. 000, 135

[8] Carlstrom J. E., Gilbert P. H., Eric D. R. 2002, "Cosmology with the Sunyaev-Zel'dovich Effect". astro-ph/0208192v1

[9] Chary R., Elbaz D. 2001, "Interpreting the Cosmic Infrared Background: Constraint on the Evolution of the Dust Enshrouded Star Formation Rate", astro-ph/0103067v2.

[10] Conselice J. Christopher and Gallagher S. John III 1998. "Tides, Interactions, and Fine-Scale Substructures in Galaxy Clusters", astro-ph/9809390

[11] Croton D. J. et al., 2005. "The many lives of AGN: cooling flows, black holes and the luminosities and colours of galaxies".astro-ph/0508046v4

[12] Daddi E., Dickinson M., Morrison G., Charry R., Cimatti A., Elbaz D., Frayer D., Renzini A., Pope A., Alexander D. M., Bauer F. E., Giavalisco M., Huynh M., Kurk J., Mignoli M. 2007 "Multiwavelength study of massive galaxies at $z \sim 2$: Star formation and galaxy growth". astro-ph/0705.2831v2

[13] Dicke, R. H. 1946. "The Measurement of Thermal Radiation at Microwave Frequencies". Review of Scientific Instruments 17: 268275.

[14] Diego J. M., Hansen S. H. and Silk J., "The impact of relativistic corrections and component separation in the measurement of the Sunyaev-Zel'dovich effect and on the small angular scale non-Gaussianity of the cosmic microwave background". MNRAS, 338 (2003) 796

[15] Dipak Munshi, Cristiano Porciani, and Yun Wang 2004. "Galaxy clustering and dark energy". Rev. Astron. Soc. 349, 281290

[16] De Lucia G., Kauffmann G., Springel V., White D. M., Lanzoni B., Stoehr F., Tormen G., Yoshida N. 2004. "Substructures in Cold Dark Matter Haloes". astro-ph/0306205v2

[17] De Lucia Gabriella, Springel Volker, White D. M. Simon, Croton Darren and Kauffmann Guinevere 2006 "The formation history of elliptical galaxies". Mon. Not. R. Astron. Soc. 366, 499509

[18] Draine B. T. 2003, "Astrophysics of Dust in Cold Clouds". astro-ph/0304488

[19] Dunne L., Eales S., Edmunds M., Ivison R., Alexander P., & Clements D. L. 2000, MNRAS, 315, 115

[20] Eisenstein D.J., 2003. "Large-scale structure and future surveys in Next Generation Wide Field Multi-Object Spectroscopy". ASP Conference Series vol. 280, ed. M.Brown & A.Dey. astro-ph/0301623

[21] Eisenstein D. J. et al, 2005. "Detection of the baryon acoustic peak in the large-scale correlation function of sdss luminous red galaxies". astro-ph/0501171v1

[22] Escalera E., Biviano A., Girardi M., Giuricin G., F. Mardirossian Mazure A., and Mezzett M. 1993. "Structures in Galaxy Clusters". astro-ph/9309057v1.

[23] Geller, M.J. and Beers, T.C, 1982. "Substructure within Clusters of Galaxies". Publ. Astron. Soc. Pac. 94:421

[24] Gerard Lemson 2006. "Halo and Galaxy Formation Histories from the Millennium Simulation: Public release of a VO-oriented and SQL-queryable database for studying the evolution of galaxies in the λCDM cosmogony". http://www.mpa-garching.mpg.de/millennium.

[25] Giard M. ,Montier L., Pointecouteau E., and Simmat E. 2008. "The Infrared Luminosity of Galaxy Clusters". astro-ph/0808.2404v2

[26] Gnedin Y. Nickolay, 2000, "Effect of Reionization on Structure Formation in the Universe". astro-ph/0002151v2

[27] Guth H. Alan, 1981. "Inflationary universe: A possible solution to the horizon and flatness problems". Phys. Rev. D 23:34756

[28] Hopkins M. Andrew 2006. "The Star Formation History of the Universe". astro-ph/0611283v1

[29] Huynh T. Minh , Frayer T. David, Mobasher Bahram, Dickinson Mark, Chary Ranga-Ram, Morrison Glenn 2007 "The far-infrared luminosity function from GOODS-N: constraining the evolution of infrared galaxies for $z \leq 1$ astro-ph/0707.4505v1

[30] Jenkins, A. et al. 2001. "The mass function of dark matter haloes". Mon. Not. R. Astron. Soc. 321, 372384 (2001)

[31] Kambas A., Davies J. I. , Smith R. M., Bianchi S. and Haynes J. A. 2000. "The Low Surface Brightness Extent of the Fornax Cluster". astro-ph/0005099

[32] Karl Glazebrook, Chris Blake, 2003, "Probing dark energy using baryonic oscillations in the galaxy power spectrum as a cosmological ruler". A.J 594:665-673

[33] Kauffmann G., 1996. "Disc galaxies at z=0 and at high redshift: an explanation of the observed evolution of damped Lyalpha absorption systems". MNRAS, 281, 475

[34] Kauffmann Guinevere , Haehnelt Martin, 1999. "A Unified Model for the Evolution of Galaxies and Quasars". astro-ph/9906493v1.

[35] Kennicutt C. Robert, 1998 "The Global Schmidt Law in Star Forming Galaxies". ApJ, 498, 541

[36] Knox L., Gilbert P. Holder, Sarah E. Church 2004. "Effects of submilimeter and radio point sources on the recovery of Sunyaev-Zeldovich galaxy cluster parameters". The Astrophysical Journal, 612:96107

[37] Kosowsky A. "The Atacama Cosmology Telescope", New Astron. Rev. 47, 939 (2003)

[38] Kragh, Helge 1999. Cosmology and Controversy: The Historical Development of Two Theories of the Universe. Princeton University Press

[39] Kravtsov V. Andrey., 2004. "The tumultuous lives of galactic dwarfs and the missing satellites problem". astro-ph/0401088v2

[40] Kriessler R. Jeffrey, Beers C. Timothy (1997). "Substructure in Galaxy Clusters:A Two Dimensional Approach". Astronomical Journal v.113, p. 80-100

[41] Lagan T. F., Lima Neto G. B., Andrade-Santos F., and Cypriano E. S. 2008. "Star formation efficiency in galaxy clusters". astro-ph/0804.1102v2.

[42] Luigina Feretti, Isabella M. Gioia, Gabriele Giovannini, 2001. "Merging processes in galaxy clusters". Kluwer Academic Publishers, page 40 - 67

[43] Malcolm S. Longair 2004. "High Energy Astrophysics", Vol 1 Particles,photons and their detection, second Edition. Cambridge University press

[44] Matthew R. Francis, Rachel Bean, and Arthur Kosowsky, 2005. "Impact of Systematic Errors in Sunyaev-Zel'dovich Surveys of Galaxy Clusters". astro-ph/0511161v2

[45] Mo H. J., Mao Shude, and White D. M. Simon 1998, "The Formation of Galactic Disks". astro-ph/9707093v1.

[46] Peacock J. A., 1999, "Cosmological physics". Cambridge University Press

[47] Peebles P. J. E., 1980, "The large-scale structure of the universe". Princeton University Press

[48] Press, W. H. & Schechter, P. "Formation of Galaxies and Clusters of Galaxies by Self-Similar Gravitational Condensation". Astrophys. J. 187, 425438 (1974)

[49] Rephaeli Y., 2001. "The sunyaev-zeldovich effect and its cosmological significance". arXiv:astro-ph/0110510.

[50] Sajina A., Scott D., Dennefeld M., Dole H., Lacy M., Lagache G. 2006. "The 1 - 1000 μm SED of far-infrared galaxies". astro-ph/0603614v1.

[51] Sazonov S.Y., Sunyaev R.A. 1998. "Cosmic Microwave Background Radiation in the Direction of a Moving Cluster of Galaxies with Hot Gas: Relativistic Corrections". astro-ph/9804125v2

[52] Sehgal N., Bode P., Das S., Hernandez-Monteagudo C., Huffenberger K., Yen-Ting Lin, Ostriker J. P., Trac H. 2009. "Simulations of the microwave sky", astro-ph/0908.0540v3.

[53] Seo Hee-Jong and Eisenstein J. Daniel 2005. "Probing Dark Energy with Baryonic Acoustic Oscillations". ASP Conference Series, Vol. 339, 2005

[54] Spergel D. et al., 2003. "First Year Wilkinson Microwave Anisotropy Probe (WMAP) Observations: Determination of Cosmological Parameters". astro-ph/0302209

[55] Springel V., White S. D. M., Tormen G., Kauffmann G., 2001b, MNRAS, 328, 726

[56] Springel V. et al., 2005. "Simulating the joint evolution of quasars, galaxies and their large-scale distribution". Nature, 435, 629

[57] Sunyaev R. A., Zel'dovich Ya. B. (1980). "Microwave background radiation as a probe of the contemporary structure and history of the universe". Annual review of astronomy and astrophysics 18: 537 560. doi:10.1146/annurev.aa.18.090180.002541

[58] West, M.J. and Bothun, G.D. 1990, "A reanalysis of substructure in clusters of galaxies and their surroundings". Astrophys. J. 350, 36.